Optical memory in an erbium doped crystal : efficiency, bandwidth and noise studies for quantum memory applications

Julian Dajczgewand

NNT : 2015SACLS198

THESE DE DOCTORAT
DE
L'UNIVERSITE PARIS-SACLAY
PREPAREE AU
"LABORATOIRE AIME COTTON"

ECOLE DOCTORALE N° 572
Ondes et matière

Spécialité: physique quantique

Par

M. Julian Eduardo Dajczgewand

Optical memory in an erbium doped crystal:
Efficiency, bandwidth and noise studies for quantum memory applications.

Thèse présentée et soutenue à Orsay, le 10/12/2015:

Composition du Jury :

M. Arne Keller	Professeur (ISMO)	Président
M. Nicolas Sangouard	Professeur (Université de Bâle)	Rapporteur
M. Patrice Bertet	Ingénieur CEA (CEA Saclay)	Rapporteur
M. Aziz Bouchene	Professeur (IRSAM)	Examinateur
M. Thierry Chanelière	Chargé de recherche (LAC)	Directeur de thèse

Acknowledgements

Une image vaut mille mots...

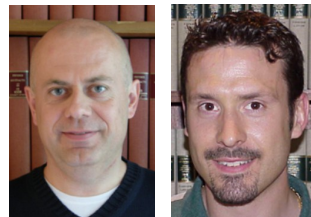Les mecs de l'atelier: Les sommeliers du LAC.

Le bureau de Herve (le chef du labo):

Le bureau des etudes: les flatteurs (ça pourrait être pire....)

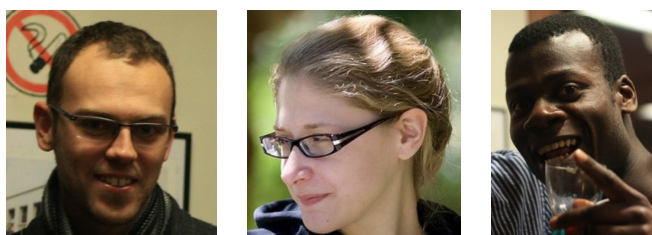Le bureau des informaticiens (les hdmi):
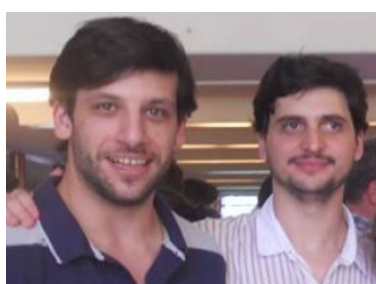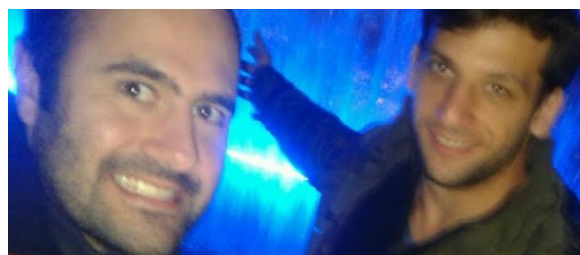
Le bureau des electroniciens:

La reine, Chloe et Hans:
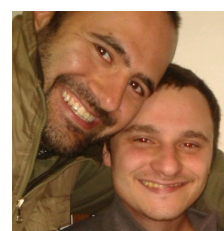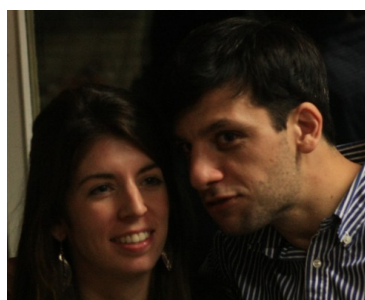
Les CIPRIS:

Les docteurs:

Le chef:

Les autres chefs:

Los amigos: (y los que no pudieron venir a la defensa)

L'amour:

La familia:

Contents

Abstract

This thesis presents the performance of a storage protocol, adapted as quantum memory, called Revival of Silenced echo (ROSE) in Er^{3+}:Y_2SiO_5. This work was done in the framework of a European ITN project called Coherent Information Processing in Rare-Earth Ion Doped Solids (CIPRIS). This network aims at developing new technologies based on coherent interaction with rare earth materials or lanthanides.

Rare earth materials have taken a major role in the development of several quantum applications. In this work we are interested in their application as an optical quantum memory. The improvement made in generating and controlling quantum light states in the last two decades have showed the need of an optical quantum memory. In this context, rare earth materials have been in the spotlight because of their unique characteristics. Thanks to their particular electronic distribution the rare earth ions are protected from the environment, leading to a series of features, such as long coherence times, making them good candidates for optical processing of classical and quantum information. Among all lanthanides, erbium stands out from the rest because its transition is located in the C-band of the telecom spectrum, where the losses in optical fibers are minimized.

Several protocols have been proposed to store information encoded in a light state at telecom wavelength. Among those, there are only two protocols that have already been tested with a few photons: the atomic frequency comb (AFC) and controlled reversible inhomogeneous broadening (CRIB). In this work, I will present the performance and latest improvements while using ROSE protocol in Er^{3+}:Y_2SiO_5 to store information. ROSE protocol was proposed in 2011 by our group. This protocol, based on the photon echo technique, has been tested in Tm^{3+}:YAG and in Er^{3+}:Y_2SiO_5 since 2011. However, a complete analysis of ROSE performance was still missing. Particularly, its performance at telecom wavelength while storing classical pulses as well as a few photons.

ROSE sequence, as opposed to other protocols already tested at telecom wavelength, does not need any preparation step and it can access to the whole inhomogeneous linewidth to store information. Therefore, short pulses or high repetition rates can be achieved. However, as the sequence is based on strong rephasing pulses, noise coming from spontaneous emission due to the inversion of the media needs to

be studied to be able to work with a few photons.

This work is organized as presented in the diagram below. The first chapter of this thesis presents an overview of the applications based on quantum memories, the parameters to estimate their performance and the protocols that succeeded in storing quantum information at telecom wavelengths. Chapter 2 is devoted to the material used to store information in this work, their properties and their most important features. In chapter 3, I present the basis of the interaction between light and matter in a two-level system while, in chapter 4, I discuss the propagation of a weak pulse, the evolution of the coherences and the radiative response of the media. These two former chapters are the basis to explain how ROSE protocol works. ROSE protocol is laid out in chapter 5. Moving forward to the experimental part, in chapter 6 the experimental set-up is presented. Afterwards ROSE protocol performances are shown in chapters 7, 8 and 9, where the efficiency for a fixed bandwidth, the efficiency as a function of the bandwidth and the performance with a few photons are presented respectively. Finally, in chapter 10, I will present a series of new materials doped or codoped with erbium to analyze their capability for optical processing.
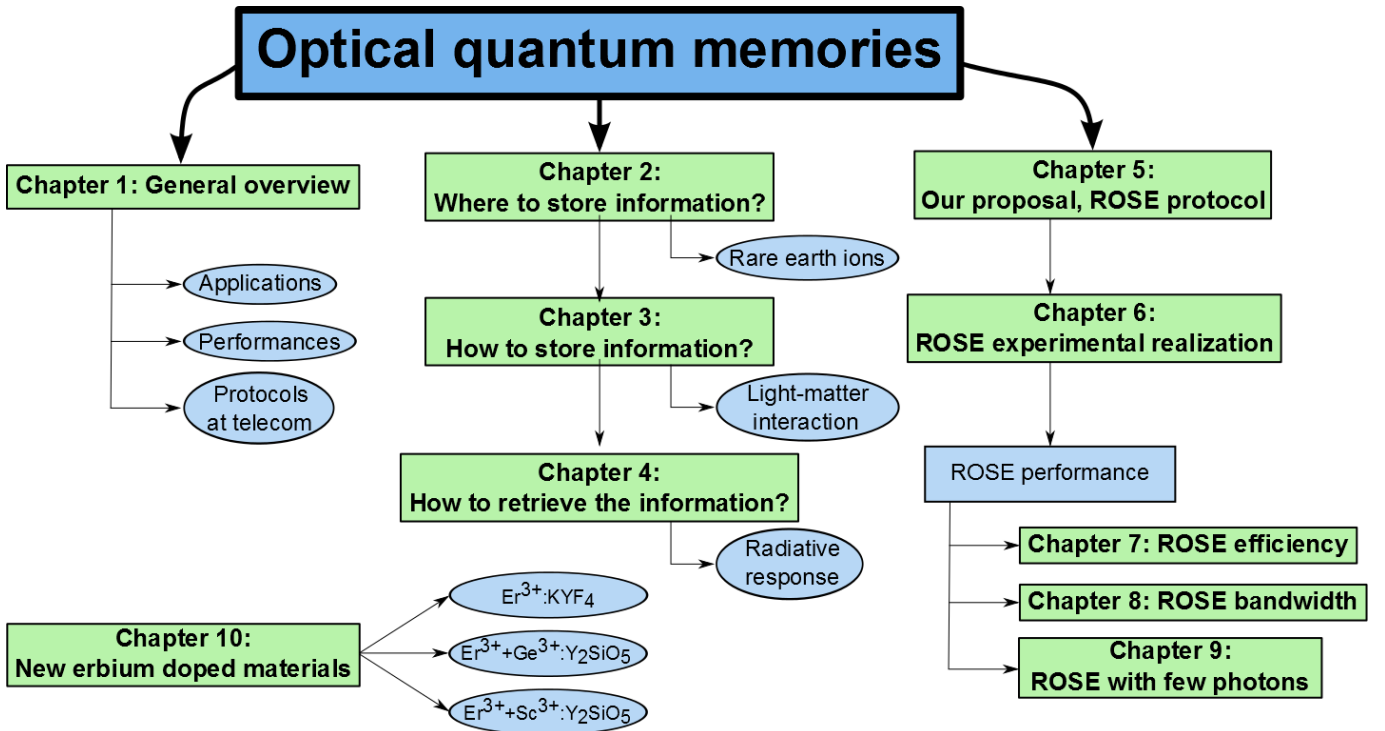
Quantum memories in solids
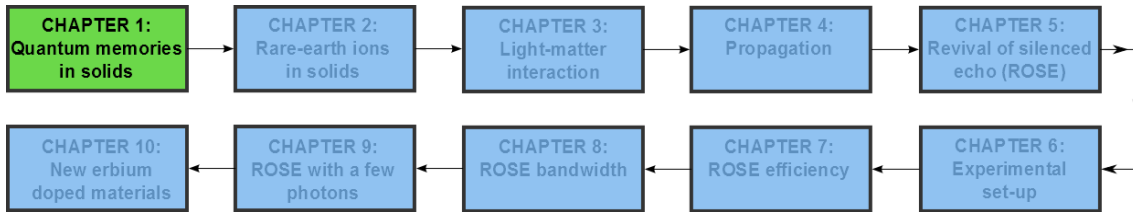
Quantum mechanics appeared in the 20th century with the quite known ultraviolet catastrophe. This catastrophe came from the fact that classical statistical mechanics predicted that a black body in thermal equilibrium should radiate with infinite power. Max Planck, by adding ad hoc hypothesis, explained that the electromagnetic radiation is emitted or absorbed in discrete packages. The measurements made by Planck and the theory to explain them opened the door to a crisis of the actual paradigm. However, It was not until the early 20's where the quantum theory was fully developed and accepted by the scientific community.

Since the acceptance of the quantum mechanics theory to describe the microscopic world, many applications were developed with great success. In the early 80's, Feynman proposed to build up a computer that uses quantum mechanics to its advantage [1]. Although computers processors were rapidly increasing their speed, Gordon Moore made an observation, in 1965, about how the number of transistors of a processor will increase in time [2]. As the size of the processors is reduced and the number of transistors is increased to improve processors speed, quantum effects, such as tunneling effect, will put up a barrier to its development. In this context, quantum computing emerged as a possible new paradigm to overcome classical computer limitations.

However, it was not until the early 90's when the first algorithms that showed how powerful a quantum computer would be appeared [3]. These algorithms showed to be much faster than the classical algorithms, even to break security codes such as RSA encryption based on classical computers. Since people clearly envisaged the potential of quantum computation, much effort have been devoted to the development of this new computing paradigm, where the information is processed and analyzed using the quantum theory.

Quantum information processing showed many promises but it is technically

challenging to implement. Since 2000, after the demonstration of the equivalence between quantum gates and linear optics [4], optical quantum information processing appeared as on opportunity to implement quantum computation.

In this context, where quantum computation came out as a way to overcome the limitations of classical electronics, several components appeared necessary to generate, process and send quantum information. Optical quantum memories has been considered one of the most important components. Although one would think that its goal it is only related to store information as a regular hard drive does, several applications in different fields, such as long distance quantum communication, quantum processing, metrology, among others, are based on a quantum memory.

This chapter starts with two applications for which optical quantum memories play an important role. Afterwards, I will briefly discuss a few relevant parameters to evaluate the performance of a memory. Then I will present two storage protocols used as optical quantum memories that succeeded in storing information at telecom wavelengths. I will finish this chapter introducing our proposal to store quantum information.

1.1   Quantum memories applications

An optical quantum memory is a device that allows to store a quantum state during a certain time. The development of optical quantum information processing applications has shown that a quantum memory is a key element as an important technical step toward several applications [5].

Here I will focus my attention on two applications where quantum memories would have a strong effect on their performances. First, I will discuss long distance quantum communications and, then, I will present the advantage of using an optical quantum memory for quantum processing.

1.1.1   Quantum repeaters

Sending quantum information at long distances has appeared as a major challenge. Due to the losses of the quantum channels (i.e. optical fibers), the range to transmit quantum information faithfully is limited to hundreds of kilometers. To overcome the photon losses, Briegel and coworkers proposed, in 1998, a scheme which establishes entanglement between two spatially separated states [6]. This scheme, known as BDCZ, might allow quantum communication at long distances. The strategy of BDCZ is based on dividing a long quantum channel into shorter segments and distribute entanglement between these segments. However, as the entanglement

distribution is a probabilist effect, a quantum memory is needed in order to wait until the entanglement is achieved in the neighboring segments. Quantum repeaters is one of the most promising applications of quantum memories explaining why it has received much attention in the last decade. However, due to the limited coherence time of the memories, the implementation of a quantum repeater was limited to short segments. To overcome this difficulty, Collins and coworkers developed, in 2007, a different approach to set up a quantum repeater based on multiplexed quantum nodes [7, 8]. The main idea is to use a system of parallel nodes to increase the rate of success of achieving entanglement. Additionally, they proposed to connect dynamically different nodes depending on the entanglement success. Although this proposition partially relaxes the condition about the coherence time or storage time of the memory, it requires a multimode memory for parallel processing.

1.1.2   Quantum processing

As time goes on, more qubits are needed to perform more complex calculations. The creation of photon pairs is a probabilistic event, thus generating a large number of qubits still remains as a challenge. In 2011, Yao and coworkers presented a multipartite entangled system composed of eight photons [9]. The data acquisition lasts 40 hours. A different approach to generate multipartite system was laid out in 2013 to overcome the long waiting times and the unwanted pairs generated by sources of entangled photons. Nunn and coworkers showed that quantum memories might be used to generate multiphoton systems [10], enhancing the multiphoton rate.

Starting from a series of photon pair sources, every heralded photon generated by these sources is stored in a memory. The memory here acts as a buffer. When all the sources heralded photons, the memory is triggered and the photons released. As in the case of quantum repeaters, a high multimode capacity of the memory is desired. However, as the photons are stored in the medium until all the photons are heralded, the storage time is also a crucial element. A parameter that combines both multimode capacity and storage time is given by the time-bandwidth product.

1.2   Properties of memories

An optical quantum memory is a system that converts a light state into a matter state. After a certain time, it is released as an optical state. As a classical memory, a quantum memory has certain features to evaluate its performances [11]. Here, I consider the efficiency, the storage time, the bandwidth, the multimode capacity and

the fidelity. In this section I will define them and briefly discuss these parameters.

1.2.1 Efficiency

The efficiency of a memory (η) is defined as the ratio between the energy of the retrieved signal (ϵ_r) and the energy of the stored signal (ϵ_s):

$$\eta = \frac{\epsilon_r}{\epsilon_s} \tag{1.1}$$

In the case of single photon storage it can be thought as the probability of recovering one photon. This parameter is, in general, quite easy to measure. However, the efficiency of a quantum memory does not take into account any contamination of the retrieved state. Therefore, it does not give any information about how well a quantum state is preserved.

1.2.2 Storage time

The storage time of the quantum memories is an important feature driven by the applications. However, the minimum storage value required for different applications changes. In long distance quantum communication, one would expect to have a storage time as long as the time to create the entanglement between nodes. However, it has been shown that a way to overcome the storage time limitation of some memories, one could rely on the multiplexing capacity of a memory to increase the success probability. For quantum repeaters, a minimum storage time in the range of milliseconds to one second is required.

1.2.3 Bandwidth

A large bandwidth memory would allow to store extremely short pulses. Additionally, a large bandwidth will permit to use a high repetition rate. For storage protocols such as ROSE or AFC, that will be presented later, the bandwidth of a memory is limited by the absorption profile of the material used to store the information.

1.2.4 Multimode capacity

The multimode or multiplexing capacity of a memory determines the number of modes or qubits that can be stored in parallel. This parameter has been shown to be of high importance in all applications based on quantum memories. Due to

the probabilistic nature of the quantum theory, memory multiplexing increases the chance of success by accomplishing the tasks in parallel.

Multiplexing is mainly performed in two domains: spatial and spectral. The spatial multiplexing is performed by dividing an atomic medium into spatially subensembles where the information is stored independently [12]. The spectral domain is used to perform what is called temporal multiplexing [13, 14, 15]. Materials with large inhomogeneous linewidth are of much interest as they might allow to store a large amount of information. The multiplexing capacity of a memory can be evaluated by taking the storage time-to-bandwidth product.

1.2.5   Fidelity

Although the efficiency is a parameter quite easy to measure, it does not take into account any contamination of the input state. A common criteria used to evaluate the general performance of the memory is given by the fidelity. The fidelity is related to the overlap between the input state and the output state, and it gives information about the conservation of the quantum nature of the input state. In terms of the applications, the memory does not need to perfectly store the information. Although there is a threshold for the fidelity, if the quantum memory works above this limit, fault tolerant quantum error correction can be used to overcome the imperfections of the memory.

1.3   Protocols to store quantum information

Quantum memories have been implemented in several ways. In this work, I will focus on quantum memories in solids, particularly in atomic ensembles in rare earth ion doped crystals. As it will be presented in chapter 2, these atomic systems show interesting features that make them good candidates for quantum memories. A variety of protocols to store information were proposed using several approaches. A good review can be found in [16]. In the following sections, I will focus my attention on two protocols that succeeded in storing information at telecom wavelengths. First, I will discuss the atomic frequency comb (AFC) and then the controlled reversible inhomogeneous broadening (CRIB). Finally, I will introduce our proposal to store quantum information: revival of silenced echo (ROSE).

1.3.1   Atomic frequency comb (AFC)

In 2009, Afzelius and coworkers proposed a protocol to store information based on the spectral shaping of an inhomogeneous transition into a series of peaks [17]. In

figure 1.1 the scheme of the protocol is depicted. The top part of the figure shows the different energy levels involved in the protocol, while the bottom part represents the temporal sequence.
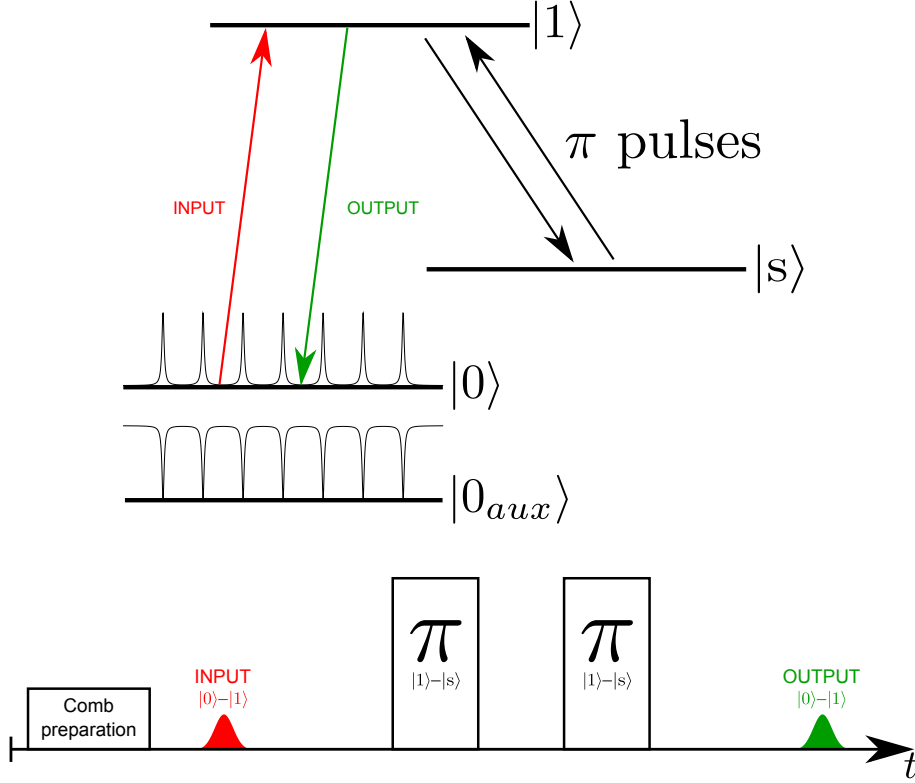
Figure 1.1: Atomic frequency comb (AFC) protocol to store quantum information.

The transition $|0\rangle$-$|1\rangle$ is spectrally shaped by optically pumping the level $|0\rangle$ to an auxiliary state $|0_{aux}\rangle$. This is done to obtain periodic narrow structures called the atomic frequency comb. Initially, a weak input pulse is sent to the crystal, coherently exciting a coherent matter state. Initially the coherence associated to each peak are in phase. As time evolves, the coherences will acquire an inhomogeneous phase which depends on the detuning of the excited atom with respect to the laser frequency. As the frequency comb is periodic, after a certain time the coherences will be in phase again. An echo is formed and the input information recalled. This, in principle, can be thought as an optical delay as there is no control of the readout time. However, taking advantage of the large coherence time of the spin levels, the state can be transfered from the state $|1\rangle$ to a spin level ground state $|s\rangle$. Using a pair π-pulses, it is possible to control the storage time, performing what is known as spin echo.

Regarding its performance, AFC was tested in different materials for different wavelengths. In the C-band of the telecom region (around 1.5 μm), in 2011, Lauritzen and coworkers reported an efficiency of 0.7% at single photon level for a storage time of 360 ns [18]. Recently, a 1% efficiency for a storage time of 5 ns was

reported in an erbium-doped optical fiber [19].

1.3.2   Controlled reversible inhomogeneous broadening (CRIB)

In 2006, Kraus and Alexander proposed a quantum memory protocol based on controlling artificially the inhomogeneous broadening [20, 21]. This scheme, known as controlled reversible inhomogeneous broadening (CRIB), uses external fields to induce a controllable broadening and to revert its effect. In figure 1.2, a scheme of the protocol is presented, where the levels scheme is presented on top and, in the bottom part, the temporal sequence.
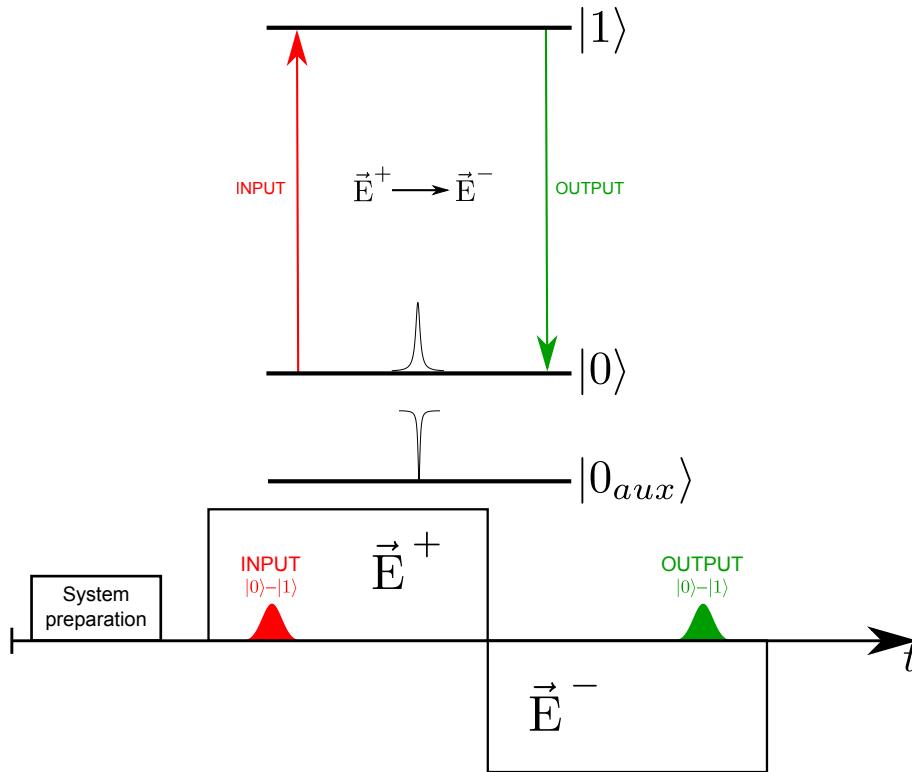
Figure 1.2: Controlled reversible inhomogeneous broadening (CRIB) protocol using an electric field [22].

When the input pulse carrying the information is absorbed by the medium, which is artificially broadened because of the DC electric field applied, the coherences start to dephase because of the inhomogeneous broadening. Then, by reversing the electric field, the artificial detuning is also inverted. The inhomogeneous phase accumulated before inversion is now subtracted leading to the emission of an echo at the instant of rephasing. The information is retrieved as a light state. Regarding its efficiency in the single photon regime, in 2011 an efficiency of 0.25% for a storage time of 300 ns at telecom wavelength was reported [23].

1.3.3 Revival of silenced echo (ROSE): a different approach

In 2011, our group proposed a new protocol to store information called revival of silenced echo (ROSE) [24]. This protocol goes back to the two-pulse photon echo basis, making it suitable to store quantum information. In figure 1.3, a scheme of ROSE is presented, on the top part of the figure the levels scheme are presented while on the bottom part the temporal sequence is shown. ROSE protocol uses the "natural" inhomogeneous broadening of the medium so there is no initial preparation required (optical pumping).
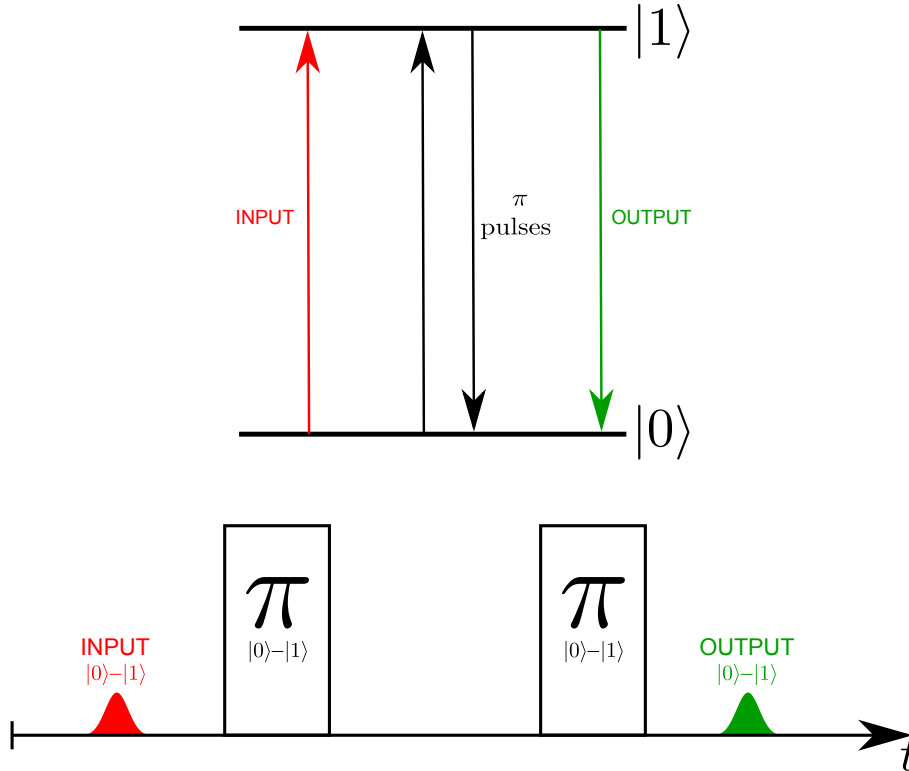
Figure 1.3: Revival of silenced echo (ROSE) protocol [24].

Initially, a weak pulse is sent to the crystal, which will be absorbed by the material. Due to the inhomogeneous broadening of the material, the atoms with different frequencies start to dephase. To control the coherence rephasing a pair of π-pulses are used on the same transition as the input pulse. This sequence can be seen as a succession of two "two-pulse photon echo" sequence. In order to make the protocol suitable to be used as a quantum memory the first echo should not be emitted, or in other words, should be silenced justifying the name ROSE. The first π-pulse is sent in a way that, although the rephasing of the coherences is achieved, the phase matching condition is not satisfied and the first echo is not emitted. On contrary, the second π-pulse beam direction is adjusted to satisfy the phase matching condition for the second echo at the very end of the sequence. Because a

pair of π-pulses is used, the atoms are brought to the ground state. Additionally, the information can be transfered to the spin level to extend the storage time of the memory. However, depending on the material it might be quite hard to achieve a good transfer efficiency from the optical transition to the spin level.

Regarding its performance, ROSE protocol has been tested in the classical regime as well as with few photons. In 2011, an efficiency of 10% for a storage time of 26 μs was reported in Tm^{3+}:YAG (793 nm), while 12% at telecom wavelength for a storage time of 82 μs [24]. Recently, a 12% efficiency at single photon level for a storage time of 40 μs was reported in Tm^{3+}:YAG [25].

In section 5, I will explain in more detail how ROSE protocol is set up. In this thesis I will present the first results of the efficient implementation of ROSE at telecom wavelengths. I will present its performance for different bandwidths and, also, the first results while storing a few photons.

Rare-earth ions in solids
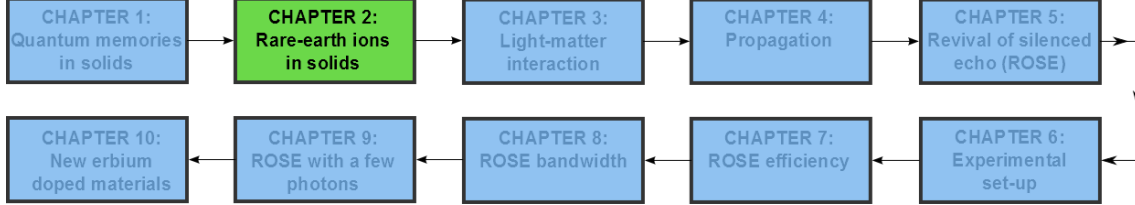
Rare earth ions in host solids have attracted the attention for optical storage and optical processing due to the long coherence times and long spectral hole lifetimes because of the weak interaction of the rare earth ions with their environment [26]. In this chapter, the main characteristics of rare earth ions are reviewed. The analysis will focus on the material studied in this thesis: Er^{3+} in a Y_2SiO_5 crystalline matrix. First, a general review of rare earth ions will be presented. This is followed by an analysis of the fine structure and spin Hamiltonian of Er^{3+} in Y_2SiO_5 . Then, the homogeneous and inhomogeneous broadening in this material will be described. This chapter finishes with a short review of instantaneous spectral diffusion.

2.1 Rare earth ions

Rare earth ions, or lanthanides, in solid hosts have been envisaged for new technological applications due to their unique characteristics: sharp absorption linewidths, long coherence times and long lifetimes. Rare earth ions have partially filled 4f orbitals while their $5s^2$ and $5p^6$ orbitals are fully filled. As the shells 5s and 5p are located further away from the nucleus than the 4f shell, they shield the 4f orbital from the environment. The shielding is so strong that, even when rare earth ions are placed into a host matrix, it is possible to approximate their behavior as free ions with a perturbation due to the crystal field. In 1962 using the Hartree-Fock approximation the first studies of rare earth ions were performed and the wavefunctions were computed as it is shown in figure 2.1 [27]. The shielding of the 4f is evidenced because the 5s and 5p shells extend further from the nucleus than the 4f shell.

There are 13 lanthanides that have partially filled 4f orbitals and, because of their similar electronic structure, they all have similar electronic structure when placed into a host matrix.
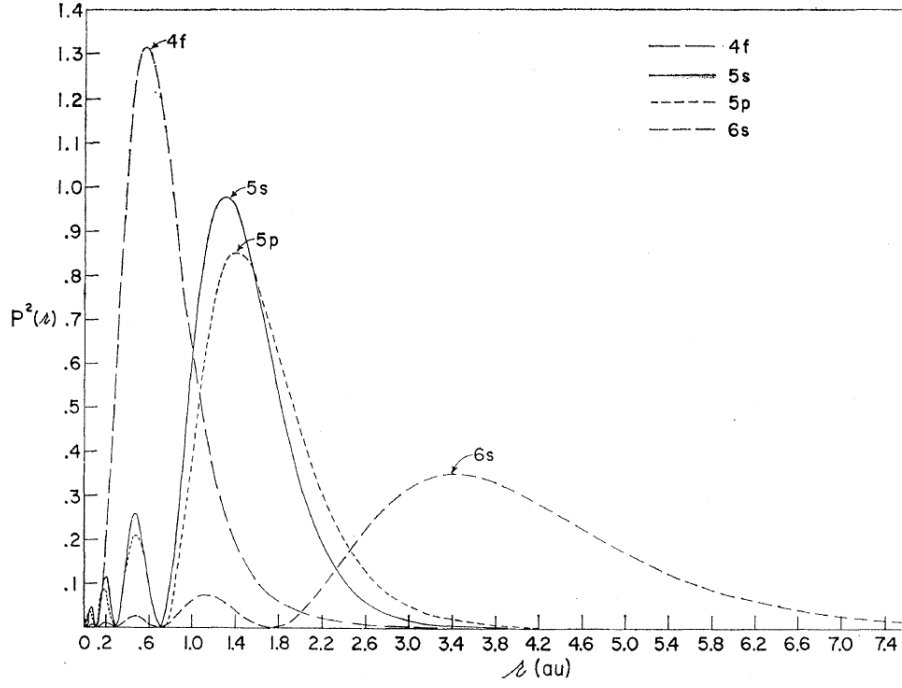
Figure 2.1: Radial probability for the 4s, 5s, 5p and 6s shells of Gd^+ from [27].

From the 60's, with the discovery of the maser (ultimately called laser), the interest in studying the transition energies and strengths of rare earth ions increased as they had shown sharp absorption lines. In 1963, Dieke and Crosswhite presented part of their research of the rare earth spectrum for the 13 lanthanides (see figure 2.2) [28].

In this work, we are interested in erbium doped crystals. Crystals doped with erbium have been extensively studied since the 90's because its transition level is located at telecom wavelength (1.5 μm) [29]. Development of optical fiber networks has exponentially growth since its discovery and, as optical fiber losses are minimized in the telecom region of the spectrum (particularly the C-band), much effort has been devoted to applications based on erbium [30].

The material studied in this thesis is Er^{3+}, which shows an optical transition at 1.5 μm. Many choices are available for the host material [31] but Y_2SiO_5 stands out among others as long coherences times have been reported using this material [32]. Y_2SiO_5 belongs to the space group C_{2h}^6 with eight formula units per monoclinic cell. Additionally, Er^{3+}:Y_2SiO_5 is a birefringent crystal [33] with 3 mutually perpendicular optical extinction axes named D_1, D_2 and b, where b is parallel to the <010> direction (C_2). A diagram of the unit cell and the extinction axes is shown in figure 2.3. The Y^{3+} ions occupy two distinct crystallographic sites with C_1 symmetry. Er^{3+} ions substitute Y^{3+} without charge compensation and, as there are two different sites, erbium ions can be found in both crystallographic sites.
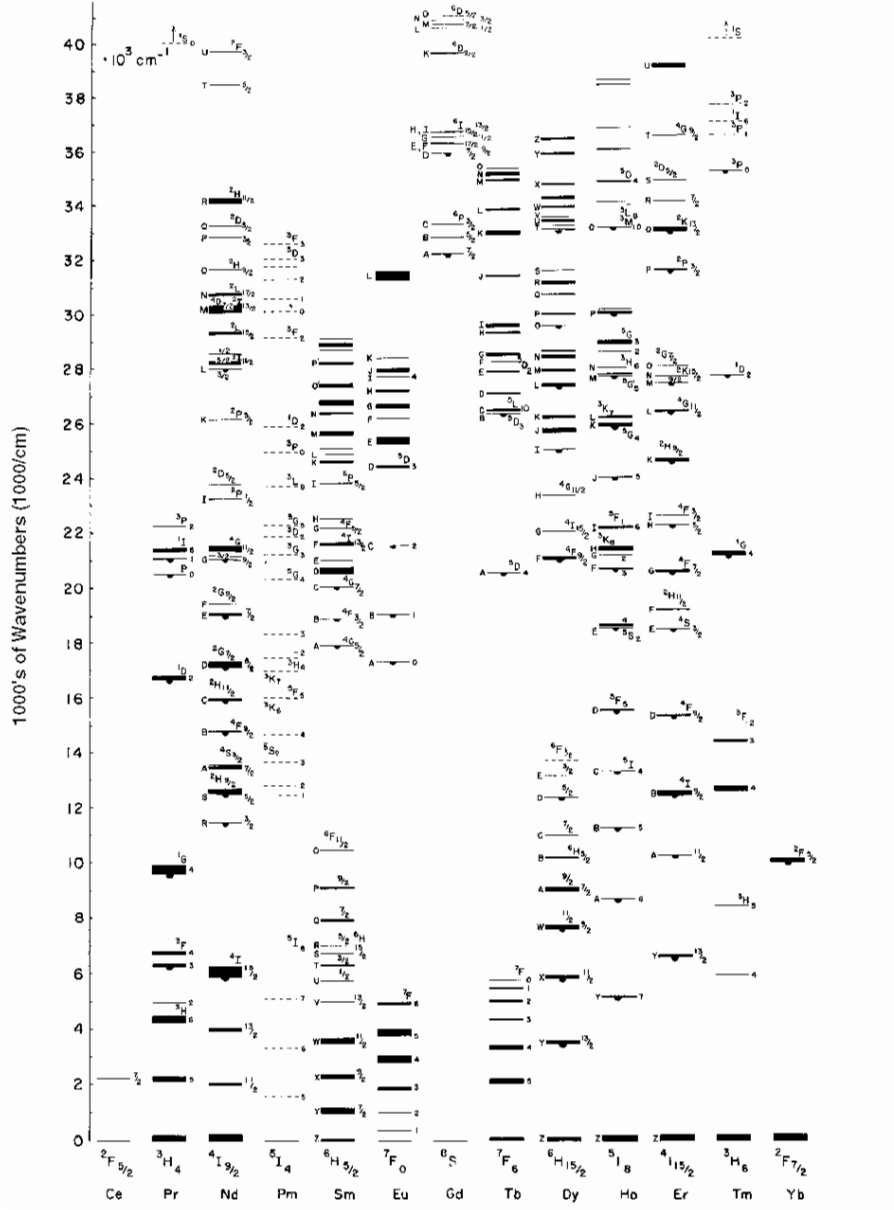
Figure 2.2: Dieke diagram for all trivalent rare earth ions in a LaCl$_3$ crystal [28].

Furthermore, each site has four subclasses of sites with different orientations [34] in the unit cell. These four sites are related by the C$_2$ and inversion symmetry. This means that there are two symmetries that characterize each site: inversion and 180^0 rotation along the b-axis. If a magnetic field is applied in an arbitrary direction, magnetic equivalence among sites is not, in general, achieved. However, depending on the symmetry that relates the sites, a different effect is expected when applying a magnetic field. For the sites related by an inversion, magnetic equivalency is expected. On the other hand, if the sites are related by a 180^0 rotation, they become, in general, magnetically inequivalent. Nonetheless there are two directions for the magnetic field in which the sites are magnetically equivalent for both symmetry
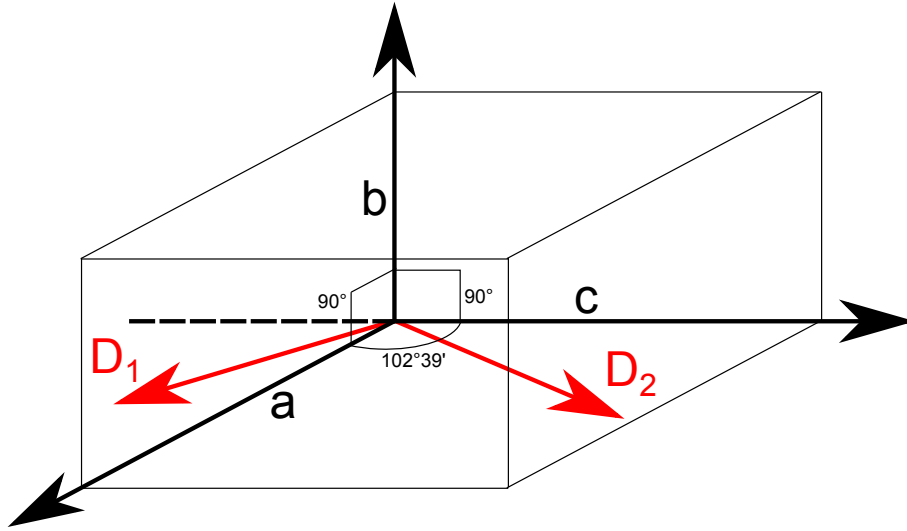
Figure 2.3: Unit cell in Er^{3+}:Y_2SiO_5 and optical extinction axes. The direction b corresponds to the C_2 axis of the unit cell.

operations as shown in figure 2.4. If the magnetic field is applied perpendicularly to the axis b (D_1-D_2 plane) or along the b axis, all subclasses become magnetically equivalent.
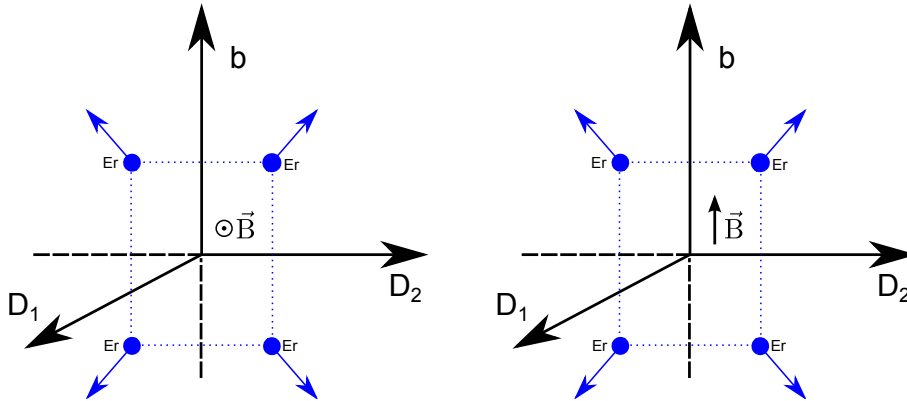
Figure 2.4: Orientation of sites in Er^{3+}:Y_2SiO_5 and the directions of the magnetic field that makes them magnetically equivalent.

2.2 Energy levels in rare earth ions

The Hamiltonian of a rare earth ion in a crystal can be thought as the free ion Hamiltonian with a perturbation due to the crystal field. This approximation greatly simplifies the calculation of eigenstates of the Hamiltonian of the system. A good review of the energy level structure is given by Liu [35]. In the absence of external fields, the primary terms of the Hamiltonian for a system of N electrons are given

by:

$$\mathcal{H}_0 = \sum_{i=1}^{N} \left(\frac{p_i^2}{2m} - \frac{Ze^2}{r_i} \right) + \sum_{i>j=1}^{N} \frac{e^2}{r_{ij}} , \tag{2.1}$$

where r_i is the distance of the electron i from then nucleus and r_{ij} is the distance of electron i from the electron j. In equation (2.1), the first term corresponds to the kinetic energy of the electron, the second term is the interaction between the nucleus and the electrons and the third term is the Coulomb interaction between the electrons. For N>1, this problem cannot be analytically solved because of the second summation of equation (2.1). However, an approximation can be done to be able to solve the Schrödinger equation with that Hamiltonian. The central field approximation supposes that the potential that an electron feels can be reproduced by a spherically symmetric function:

$$\mathcal{H}_0 = \sum_{i=1}^{N} \left(\frac{p_i^2}{2m} + U(r_i) \right) \tag{2.2}$$

Because of the symmetry of this Hamiltonian, and the fact that $\mathcal{H}_0$ is the sum of monoelectronic Hamiltonians, it is possible to compute the wavefunction for a system with N electrons using the Hartree-Fock method. However, this Hamiltonian is quite limited to describe the fine structure of rare earth ions as all the $n = 4$ levels are degenerate.

In order to lift this degeneracy it is necessary to add non-central interactions (not spherically symmetric). To do this, we need to add the next strongest interaction to the Hamiltonian, which is given by the non central part of the interaction between the electrons. This not spherically symmetric interaction will break the degeneracy of the 4f levels, which in the case of rare earth ions means that the 4f level is lifted into 4s, 4p, 4d and 4f.

The next most important interaction is given by the spin-orbit interaction:

$$\mathcal{H}_{SO} = \sum_i \xi(r_i) s_i l_i , \tag{2.3}$$

where s is the spin of electron i, l its angular momentum and ξ a constant that depends on the position of the electron. This interaction lifts the degeneracy of the 4f level. But as neither the spin (S) nor the angular momentum (L) commutes with the spin-orbit Hamiltonian, they cannot be consider as good quantum numbers for the wave functions of the electrons. However, J=L+S is a good quantum number. In that base, the problem can be broken into 2J+1 degenerate states.

The transition studied in this thesis is the one called $^4I_{13/2} \rightarrow ^4I_{15/2}$, where the Russell-Saunders notation $^{2S+1}L_J$ has been used to name the transitions. Transitions

between those levels are in the spectral region of interest, the telecom spectrum.
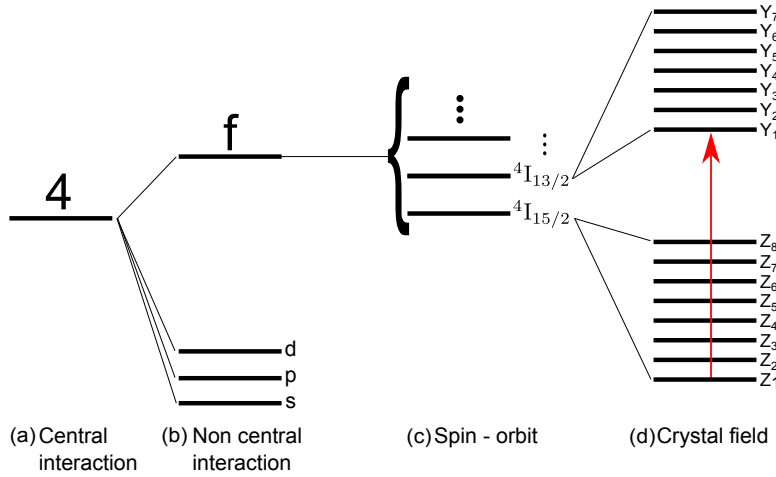
Figure 2.5: Fine structure of the 4f levels in $Er^{3+}:Y_2SiO_5$. In (a) the spherically symmetric part of the Coulomb interaction is considered. In (b) the degeneracy of the level is lifted because of the non central part of the Coulomb interaction. Adding the spin-orbit interaction lifts the degeneracy of each l, as shown in (c). In (d) the crystal field lifts the 2J+1 of each level.

So far the rare earth ions has been considered to be isolated from any other system that could interact with them. When the ions are placed into a crystal, their interaction with the field generated by the crystal fully lifts the 2J+1 degeneracy. In the figure 2.5 the fine structure for $Er^{3+}:Y_2SiO_5$ is presented, where the labels Z_1 to Z_8 has been used for the crystal field ground state $^4I_{15/2}$ and Y_1 to Y_7 for the excited state $^4I_{13/2}$. The transition of interest is the $Z_1 \rightarrow Y_1$ of the $^4I_{13/2} \rightarrow ^4I_{15/2}$ crystal field. This transition shows the highest absorption among all the possibilities for the chosen crystal fields [36].

Additionally, Kramers theorem states that, due to time reversal symmetry of the Hamiltonian, systems with an odd number of electrons (Kramers ions) remains at least doubly degenerate if only electrical field are applied to the system [37, 38]. Therefore, $^4I_{15/2}$ is split into 8 doublets while $^4I_{13/2}$ in 7 doublets. This last degeneracy, due to the Kramers ions, can be lifted applying a magnetic field. This analysis was confirmed in 1992 when Li and coworkers studied the spectroscopic properties of $Er^{3+}:Y_2SiO_5$ at different temperatures [39]. They measured the absorption and emission spectra at 10 K (see figure 2.6) for the three extinction axis of the crystal. They found out 16 lines for the emission spectra and 14 lines for the absorption spectra.

Finally, as stated in section 2, erbium ions can be found in two crystallographic sites. Using Böttger and coworkers notation for the sites [36], site 1 is located at 1536.478 nm and site 2 is located at 1538.903 nm. Site 1 has been chosen for this

thesis as it has the longest population lifetime. The importance of having a long population lifetime will be explained in section 2.4
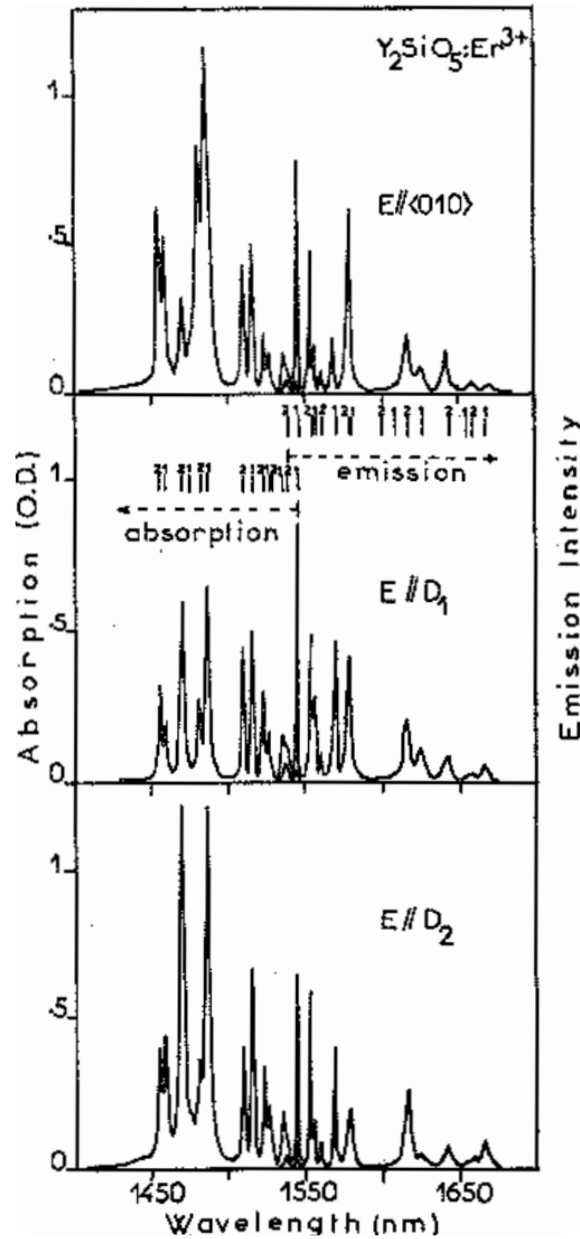
Figure 2.6: Absorption and emission spectra of Er^{3+}:Y_2SiO_5 at 10 K from [39].

2.3   Spin Hamiltonian

Up to now, only the largest contributions to the Hamiltonian have been analyzed. Once the crystal field is split, other contributions to the Hamiltonian have to be considered. For rare earth ions in a crystal the full Hamiltonian can be written as

follows [40]:

$$\mathcal{H} = \mathcal{H}_0 + [\mathcal{H}_{HF} + \mathcal{H}_Q + \mathcal{H}_z + \mathcal{H}_Z]\,, \tag{2.4}$$

where $\mathcal{H}_0$ is the Hamiltionian of the free ion and the crystal field (equation (2.1)), $\mathcal{H}_{HF}$ is the hyperfine coupling between the 4f electrons and the rare earth nucleus, $\mathcal{H}_Q$ is the nuclear quadrupole interaction, $\mathcal{H}_Z$ is the electronic Zeeman interaction and $\mathcal{H}_z$ the nuclear Zeeman interaction.

The first two terms of equation (2.4) were explained in the last section and they have the largest contribution to the Hamiltonian. The other terms are part of the spin Hamiltonian of rare earth ions. The first term that appears in between the brackets in the equation (2.4) is $\mathcal{H}_{HF}$. This term is proportional to nuclear spin and, in the case of erbium, has a small contribution to the hyperfine structure. Er^{3+} is naturally composed of many isotopes and, among them, there is only one which has a nuclear spin. This isotope, the ^{167}Er, has an abundance of only 23%, what explains why it is possible to neglect the contribution of the term $\mathcal{H}_{HF}$. Same argument can be used to neglect $\mathcal{H}_Q$ and $\mathcal{H}_z$.

In Er^{3+}:Y_2SiO_5 the most important contribution to the hyperfine structure is given by the electronic Zeeman Hamiltonian $\mathcal{H}_Z$. This Hamiltonian comes from the interaction between the electrons (Er ions in our case) and a magnetic field, and it is often written as [41]:

$$\mathcal{H}_Z = \mu_B \, \boldsymbol{B} \, \bar{\bar{g}} \, \boldsymbol{J}\,, \tag{2.5}$$

where $\boldsymbol{J}$=$\boldsymbol{L}$+2$\boldsymbol{S}$, $\boldsymbol{B}$ is the magnetic field, μ_B is the Bohr magneton and $\bar{\bar{g}}$ is the g tensor. The electronic degeneracy due to Kramers theorem and the large magnetic moments leads to large first order Zeeman splitting and, thus, at first order the angular momentum $\boldsymbol{L}$ is zero [40]:

$$\mathcal{H}_Z = \mu_B \, \boldsymbol{B} \, \bar{\bar{g}} \, \boldsymbol{S} \tag{2.6}$$

Er^{3+}:Y_2SiO_5 is characterized for its quite high anisotropy regarding the g tensors because of the low symmetry of each Er^{3+} site. However, an effective g-factor can be computed by calculating the eigenstates of the Hamiltonian. These g-factors will describe the splitting of each level. Particularly, this interaction will lift the double degeneracy of the levels Z_1 from the crystal field ground state $^4I_{15/2}$ and Y_1 from the crystal field excited state $^4I_{13/2}$ as shown in figure 2.7. The splitting of the levels depends on the value of the g-factor and can be written as:

$$\Delta E_g = g_g \mu_B B \tag{2.7}$$
$$\Delta E_e = g_e \mu_B B\,, \tag{2.8}$$

where g_g and g_e are the effective g-factors for the ground and excited state respectively. In general, these g-factors have different values, that is why a different splitting is expected for the ground and excited state.
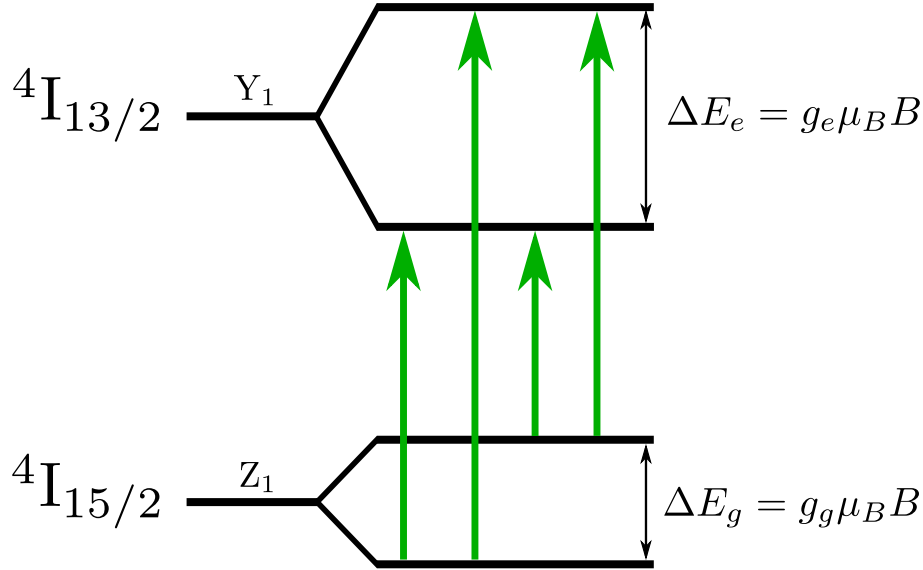
Figure 2.7: Hyperfine structure in Er^{3+}:Y_2SiO_5 for the ground state Z_1 from $^4I_{15/2}$ and the excited state Y_1 from $^4I_{13/2}$.

The g tensors for both ground and excited state were calculated by Sun and coworkers in the D_1-D_2-b coordinate system [34]:

$$\overline{\overline{g}}_g = \begin{pmatrix} 3.070 & -3.124 & 3.396 \\ -3.124 & 8.156 & -5.756 \\ 3.396 & -5.756 & 5.787 \end{pmatrix}, \overline{\overline{g}}_e = \begin{pmatrix} 1.950 & -2.212 & 3.584 \\ -2.212 & 4.232 & -4.986 \\ 3.584 & -4.986 & 7.888 \end{pmatrix}, \quad (2.9)$$

where $\overline{\overline{g}}_g$ and $\overline{\overline{g}}_e$ are the g tensors of the ground and excited state respectively. Using the g tensors calculation of the effective g-factors may be performed. In figure 2.8 the g-factors for the ground and excited state are shown as a function of the angle between the magnetic field and the optical extinction axes D_1 and D_2.

What is the relevance of the g-factors? As it was shown, the splitting of the levels depends on their values and on the external magnetic field. Having a high value of g ensures a higher splitting for a fixed magnetic field. Ultimately, the splitting of the levels competes against the thermal energy. In thermal equilibrium it can be shown that the ratio between two levels is given by:

$$\frac{N_2}{N_1} = e^{-\frac{\Delta E}{kT}}, \qquad (2.10)$$

where N_2 and N_1 are the amount of ions in the upper and the bottom level respec-

tively, ΔE is the splitting of the levels, k is the Boltzmann constant and T is the temperature.
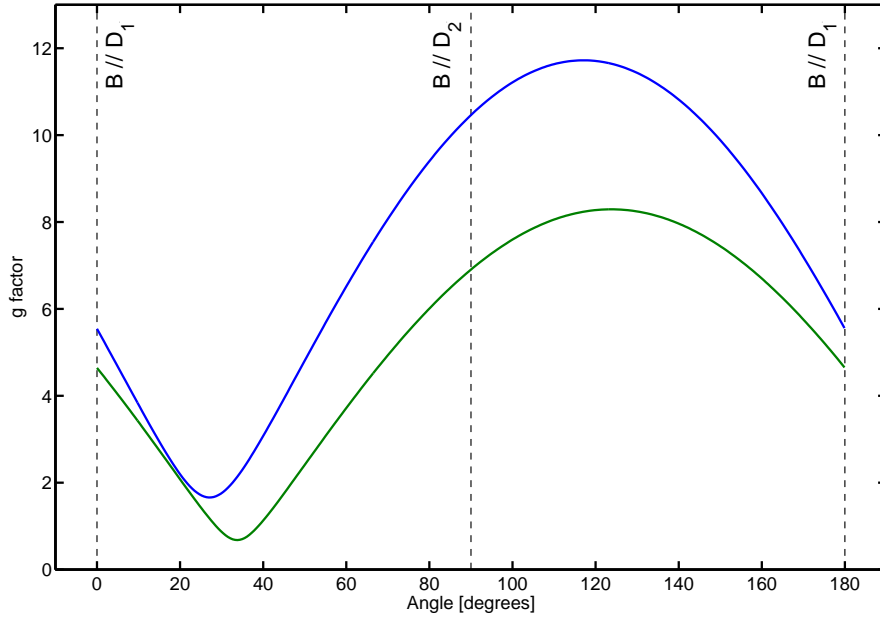
Figure 2.8: Effective g-factors as a function of the angle between the magnetic field and D_1-D_2. In green the g-factor for the excited state and, in blue, the g-factor for the ground state.

Hence, increasing the splitting is a strategy to reduce (or freeze) the population of the level N_2. In order to increase the splitting, in this thesis the magnetic field is applied in the plane D_1-D_2 (perpendicular to b) as it has been proved that this direction has the largest g-factor for both ground and excited state [34]. With that strategy it is possible to reduce optical decoherence due to electron flip fluctuations. As it will be explained in section 2.4, optical decoherence reduces the coherence time and, thus, the storage time. Additionally to the large splitting, the direction chosen for the magnetic field assures the magnetic equivalency between erbium sites.

2.4 Homogeneous broadening

The degeneracy of rare earth ions is lifted because of the crystal field and the external magnetic field. Now a set of optical transitions, characterized by their angular momentum J, describes the system. If these ions were isolated, each optical transition will have a determined linewidth given by the lifetime of the states that participate in that transition. This linewidth is known as homogeneous broadening.

Rare earth ions in crystals are characterized by having narrow homogeneous linewidths at low temperatures. This means that rare earth ions present long co-

herence times as the homogeneous linewidth is related to the coherence time:

$$\Gamma_h = \frac{1}{T_2} \, , \qquad (2.11)$$

where T_2 is the coherence time or dephasing time. Clearly, having control over the homogeneous broadening is an important issue as it may limit the storage time of a memory. Rare earth ions are characterized for having long lifetimes of the excited state, hence this phenomena does not greatly influence on the width of the line. On the other hand, as the ions are not isolated, many interactions come into account to analyze the broadening of the homogeneous linewidth. During an experiment, dynamical processes can contribute to line broadening. For example, changes in the environment or energy exchange between ions may affect a determined transition. There are two contributions to the homogeneous broadening [35]. One comes from the population lifetime of the excited state (T_1) while the other comes from other time-dependent perturbations:

$$\Gamma_h = \frac{1}{T_2} = \frac{1}{2T_1} + \Gamma_D \, , \qquad (2.12)$$

where Γ_D is the contribution to the linewidth due to pure dephasing processes.

The two sites in Er^{3+}:Y_2SiO_5 have been studied from a spectroscopic point of view showing a population lifetime of 11.4 ms for site 1 and 9.2 ms for site 2 [36]. Therefore, site 1 should have, in principle, a higher coherence time. This explains why site 1 has been chosen among the 2 sites.

In Er^{3+}:Y_2SiO_5 extremely narrow linewidth has been reported $\Gamma_h = 2\pi \times$ 73 Hz [42]. Also, Macfarlane and coworkers measured a coherence time $\Gamma_h = 2\pi \times$ 550 Hz ($T_2 = 580 \ \mu s$) [43] for an erbium concentration of 32 ppm using two-pulse photon echo. For that crystal the contribution from the population decay was only of 12 Hz, showing the weight of other processes in optical dephasing.

For rare earth ions, several processes affect the dephasing process and cause what is known as spectral diffusion: phonon processes, spin flips, ion-ion interactions. The mechanisms that increase spectral diffusion and optical decoherence in Er^{3+}:Y_2SiO_5 has been extensively studied by Böttger and coworkers [44, 45], and it can be summarized as follows:

$$\Gamma_D = \Gamma_{ion-phonon} + \Gamma_{ion-lattice} + \Gamma_{ion-ion} \, , \qquad (2.13)$$

where there are three contributions to the homogeneous linewidth: $\Gamma_{ion-phonon}$ from the interaction between the ions and phonons, $\Gamma_{ion-lattice}$ from the interaction between the ions and the host lattice and $\Gamma_{ion-ion}$ from the interaction between the

ions. For Er^{3+}:Y_2SiO_5 it is possible to summarize each contribution as follows:

- $\Gamma_{ion-phonon}$: in Er^{3+}:Y_2SiO_5 the most important contribution comes from the phonon-induced electronic spin flip due to one phonon processes. Absorption or spontaneous emission of phonons promote a spin from one Zeeman level to the other Zeeman level which causes spin-flip of Er^{3+}, changing the ion environment.

- $\Gamma_{ion-lattice}$: nuclear and electronic spins fluctuations from Y_2SiO_5 may contribute to the optical dephasing of the Er^{3+} ions. However, Y_2SiO_5 has small magnetic moments or a small abundance of magnetic isotopes, reducing decoherence due to the coupling of the erbium electronic states and the host matrix. Thus, its contribution to the linewidth is negligible [46], what explains why long coherence times have been observed in Er^{3+}:Y_2SiO_5 [45].

- $\Gamma_{ion-ion}$: here it is possible to distinguish two processes. The first one is due to mutual Er^{3+}-Er^{3+} spin flip-flops. Neighboring Er^{3+} ions, which initially are in the upper Zeeman level of the ground state, can undergo a spin-flip transition. Therefore, the local magnetic field felt by Er^{3+} ions is expected to change, leading to a shift of the crystal field levels. To minimize this effect, increasing the splitting of the Zeeman levels helps to suppress dephasing effects. This can be performed by increasing the magnetic field or by choosing the appropriate direction for the external magnetic field to maximize the g-factor. It is important to consider that both sites (1 and 2) contribute to the broadening of the linewidth due to this interaction. Thus, both g-factors should be considered while analyzing the strategy to decrease optical dephasing.

  The second processes that can be included in the ion-ion interaction is the instantaneous spectral diffusion (ISD). As it was pointed out in chapter 2.3, the g-factors of the ground and excited state are not, in general, the same. Thus, optical excitation of neighboring ions will lead to a change in the local magnetic field. ISD has an important role in the performance of our storage protocol, for that reason it will be analyzed separately in section 2.6.

By definition, the homogeneous broadening is the same for the whole system. However, rare earth ions exhibit a distribution of dipoles with different transitions energies due to the changes in their local environment. This gives place to the inhomogeneous linewidth, which I introduce in the following section.

2.5 Inhomogeneous broadening

If the environment were the same for all ions, they would have the same linewidth with a Lorentzian profile [47] (see figure 2.9).
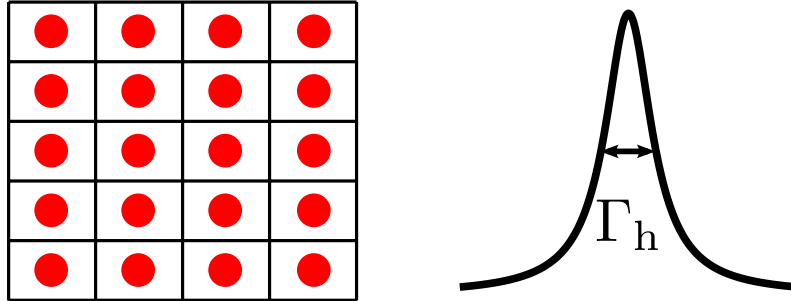
Figure 2.9: Homogeneous broadening on a material where each ion is exposed to the same environment.

However, because of defects each optical center is exposed to a different environment which leads to a Stark shift of the profile [48]. This change of the environment is due to crystalline local strains and distortions during crystal growth, impurities and dislocations. This gives rise to the inhomogeneous broadening shown in figure 2.10.
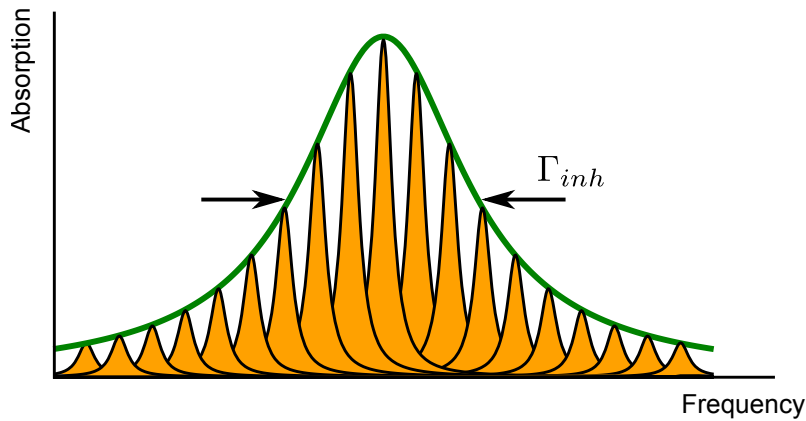
Figure 2.10: Illustration of the inhomogeneous and homogeneous broadening.

In Er^{3+}:Y_2SiO_5 different inhomogeneous linewidth were measured for different erbium concentrations [36]. It was found that the inhomogeneous linewidth was of 180 MHz, 390 MHz and 510 MHz for crystals doped with 15 ppm, 50 ppm and 200 ppm of erbium respectively. For optical processing, the inhomogeneous bandwidth provides limited information regarding its processing capacity. However, the ratio between the inhomogeneous and homogeneous linewidth gives the number of spectral channels or bins. For a crystal doped with 50 ppm of erbium, for example, this ratio

is:

$$\#\text{bins} = \frac{\Gamma_{inh}}{\Gamma_{hom}} \approx \frac{300 \text{ MHz}}{100 \text{ Hz}} = 3.10^6 \tag{2.14}$$

2.6 Instantaneous spectral diffusion (ISD)

In section 2.4, we have seen that several dynamical processes can contribute to a line broadening, affecting the coherence time of the sample. In $Er^{3+}:Y_2SiO_5$ one of the most important contributions to this effect comes from the dipole-dipole interaction between erbium ions. This interaction may induce different shifts caused by static electric or magnetic dipole-dipole interactions when ions are promoted to the excited state. This source of broadening is usually called instantaneous spectral diffusion (ISD). Although ISD is a broadening source due to the average shift caused by the interaction, it should be distinguished from spectral diffusion. ISD generates an abrupt change of the transition frequency of an ion due to some change in its environment, that contributes to the dephasing processes when ions are excited.

The first studies of ISD were performed by Mims and coworkers [49], while studying spectral diffusion in electron spin resonance experiments. These experiments were explained by Klauder and coworkers [50], showing that RF π-pulses could change the environment that a certain spin feels by flipping its neighboring spins. This change of the environment comes from the dipolar interaction between the spins and is observed as a broadening of the resonance line. Mims used the statistical method set up by Stoneham [51] and computed the broadening caused by any dipolar interaction [52]:

$$\Delta\omega = \frac{16\pi^2}{9\sqrt{3}} A n_e, \tag{2.15}$$

where A is a constant that describes the interaction (either magnetic or electric) in $m^3 \, rad \, s^{-1}$ and n_e is the spatial density of excited ions. To have a general overview of line broadening due to ion-ion interaction it is possible to look at the magnetic dipole-dipole Hamiltonian. For two ions (1 and 2), 1 in the ground state and 2 in the excited state (see figure 2.11), the change in the Hamiltonian can be written as follows:

$$\Delta\mathcal{H}_{d_1 d_2} = \mu_1 (\mu_2' - \mu_2) \frac{(1 - 3\cos^2\theta)}{r_{d_1 - d_2}}, \tag{2.16}$$

where μ_1 (μ_2) is the magnetic dipole for the ion 1 (2), μ_2' is the magnetic dipole of the excited state for the ion 2 and $r_{d_1 - d_2}$ is the distance between the ions.

As it was shown in section 2.4, the g-factors are not the same in the ground state and in the excited state, quantifying the difference of magnetic dipole when the ion gets excited. Equation (2.16) can be alternatively written as a function of

the g-factors:

$$\Delta\mathcal{H}_{d_1 d_2} = \mu_B^2 g_{1_g}(g_{2_e} - g_{2_g})\frac{(1 - 3\cos^2\theta)}{r_{d_1 - d_2}} \,, \tag{2.17}$$

If the g-factors of the ground state and the excited states were equal, there would not be any ISD. Additionally, increasing the distance between the ions reduces the change in the energy. This shows why a lower concentration crystal should exhibit less ISD. ISD has been studied in photon echo experiments. For example, Liu and Cone showed the power dependence of ISD for a Tb^{3+}:$LiYF_4$ crystal [53, 54]. Using the model presented on equation (2.15), they were able to characterize ISD by photon echo experiments.
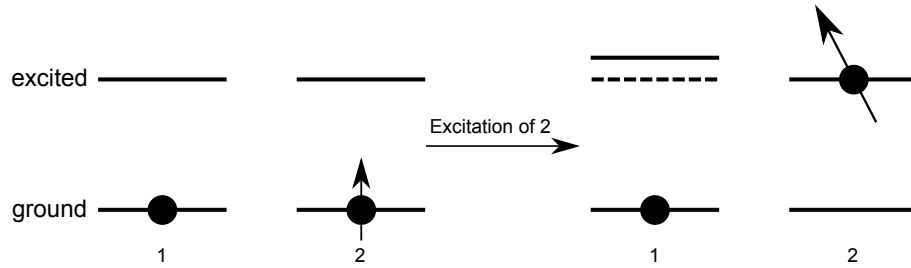
Figure 2.11: Scheme of the processes that gives place to ISD in Er^{3+}:Y_2SiO_5 because of the change in the magnetic dipole from the ground state to the excited state.

In chapter 8, I present a series of measurements to characterize ISD in Er^{3+}:Y_2SiO_5 whose effect has to be considered for the implementation of ROSE protocol. Furthermore, I will show how to calculate the ISD from microscopic parameters pushing further the model introduced here.

Light-Matter Interaction
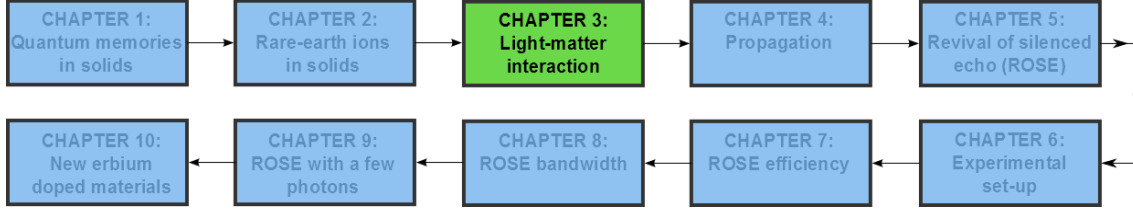
Light encoded information can be converted into a matter state and vice versa. This conversion allows to store quantum and classical information in a material [55, 56, 57]. In this work, I present a reversible way of transferring information from photons to a rare earth material. To understand how this process is carried out, we need to understand how a light state interacts with matter. The medium is described as an ensemble of two-level atoms. In this chapter, the light-matter interaction is explained while using three different approaches useful to understand our system of interest: the Schrödinger model, the density matrix and the Bloch vector.

The Schrödinger model deals with pure states. In problems where an atomic system interacts with its environment, the state cannot be described by a wavefunction (i.e. a pure state). Due to decoherence, a pure state becomes a mixed state. In those cases, the density matrix needs to be used in order to analyze the evolution of the system.

On the other hand, I will also present another state representation known as the Bloch vector. Although this approach does not add any additional information to the density matrix approach, it appears as a geometrical interpretation on the so-called Bloch sphere of a two-level system and its interaction with light.

Using theses approaches, I will analyze two cases of interest: free evolution and Rabi oscillations. These effects are the basis of the photon echo protocols that I will discuss at the end of this chapter.

3.1 Schrödinger model

In this section I will briefly explain the free evolution of a two-level system while using the Schrödinger equation. Then, the Hamiltonian including the light-matter

interaction will be presented. Finally, I will explain the limitations of using the Schrödinger approach.

3.1.1   Free evolution of a two-level system

The state of a two-level system (see figure 3.1, $|a\rangle$ is the ground state and $|b\rangle$ the excited state), reads as:
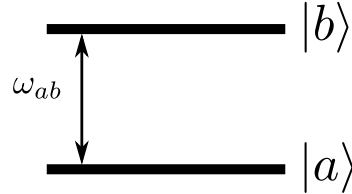
Figure 3.1:   Scheme of a two-level system.

$$|\psi(t)\rangle = a(t)|a\rangle + b(t)|b\rangle \text{ (where } a(t)^2 + b(t)^2 = 1)$$
(3.1)

The evolution of the system is given by the Schrödinger equation:

$$i\hbar\frac{d}{dt}|\psi(t)\rangle = \mathcal{H}(t)|\psi(t)\rangle$$
(3.2)

If the system is isolated from any other system, the free evolution Hamiltonian is:

$$\mathcal{H}_0 = \hbar\begin{pmatrix} 0 & 0 \\ 0 & \omega_{ab} \end{pmatrix},$$
(3.3)

where ω_{ab} is the frequency of the transition $|a\rangle$-$|b\rangle$. Solving the Schrödinger equation with this Hamiltonian, the evolution of the system will be given by:

$$|\psi(t)\rangle = a(0)|a\rangle + b(0)e^{-i\omega_{ab}t}|b\rangle$$
(3.4)

This two-level system is the one used in this thesis to store information. In the following sections, the interaction with a light field will be introduced.

3.1.2   Interaction with light

As we want to convert information encoded in a light state into a matter state, it is necessary to analyze how light interacts with matter. To do this, we have to add the interaction between electrons and an electromagnetic field to the Hamiltonian shown in equation (3.3). Under the dipole approximation ($r \ll \lambda$, with r the distance between dipoles and λ the wavelength of the light), the coupling with the laser field

will be done through the electric dipole moment. The Hamiltonian which describes this interaction is given by:

$$\mathcal{H}_D = -\vec{d}\vec{E}, \tag{3.5}$$

where $\vec{d}$ is the dipole moment and $\vec{E}$ the electric field. As $\mathcal{H}_D$ is odd parity (i.e. it links different parity states in the atomic basis), $\langle 1|\mathcal{H}_D|1\rangle = \langle 2|\mathcal{H}_D|2\rangle = 0$. On the other hand, the off-diagonal states can be written as follows:

$$d_{ab}\vec{E} = \langle 1|\vec{d}\vec{E}|2\rangle = \langle 2|\vec{d}\vec{E}|1\rangle^*, \tag{3.6}$$

where d_{ab} is the dipole moment of the atoms. In the case of erbium, the transition of interest is a 4f to 4f transition. In Er^{3+} this transition is, in principle, forbidden because of the parity selection rules. However, because of the mixing with opposite parity states, the intra 4f transitions become slightly allowed [26]. The total Hamiltonian is:

$$\mathcal{H} = \mathcal{H}_0 + \mathcal{H}_D = \mathcal{H}_0 + \vec{d}\vec{E} \tag{3.7}$$

The state vector for this Hamiltonian can be found using the Schrödinger's equation. However, if we consider that the system is a subsystem of a larger space, the state description given by $|\psi\rangle$ is no longer complete. If the two-level system is not isolated from its environment the density matrix has to be used as it allows the description of a statistical mixture [58].

3.2   Density matrix

Let $|\phi(t)\rangle$ be the wavefunction of the two-level system and the environment. The density matrix ρ_S of the whole system is given by:

$$\rho_S = |\phi(t)\rangle\langle\phi(t)| \tag{3.8}$$

The density ρ_S includes the state we want to analyze and its bath. To obtain the state of the system we have to trace ρ_S over the states of the environment. This trace, known as partial trace, will give place to the reduced density matrix ρ describing our system of interest:

$$\rho = \text{Tr}_E(\rho_S) = \begin{pmatrix} \rho_{aa} & \rho_{ab} \\ \rho_{ba} & \rho_{bb} \end{pmatrix} \tag{3.9}$$

This matrix will be the one I will use to describe the evolution of the system. It is important to notice that, in general, this state cannot be written using a wavefunction. The diagonal terms ρ_{aa} and ρ_{bb} will give information about the population in

the ground state and the excited state as they are defined as:

$$\rho_{aa} = \mathrm{Tr}(\rho_E |a\rangle\langle a|)$$
$$\rho_{bb} = \mathrm{Tr}(\rho_E |b\rangle\langle b|),$$

where $|a\rangle$ and $|b\rangle$ are the ground and excited state respectively. The non-diagonal terms ρ_{ab} and ρ_{ba} are the coherences. They dictate the behavior of the macroscopic polarization of the atomic system. The polarization is indeed given by:

$$P(\vec{r}, t) = N < D >= N\mathrm{Tr}(D\rho), \tag{3.10}$$

where N is the atomic density per unit of volume and D the transition dipole matrix. As the transition dipole matrix is only composed of non-diagonal terms, the expectation value is given by:

$$P(\vec{r}, t) = -Nd_{ab}(\rho_{ab}(\vec{r}, t) + \rho_{ba}(\vec{r}, t)), \tag{3.11}$$

where d_{ab} is the dipole transition moment for the transition a-b. Equation (3.11) gives the polarization when the medium shows an homogeneous distribution of frequencies. As it was pointed out in section 2.5, the material used in this work presents an inhomogeneous linewidth. Thus, the spectral density of the dipoles should be considered to obtain the polarization. Taking this into account, equation (3.11) can be written as:

$$P(\vec{r}, t) = -\int d_{ab}G(\omega_{ab})(\rho_{ab}(\vec{r}, t) + \rho_{ba}(\vec{r}, t))d\omega_{ab}, \tag{3.12}$$

where $G(\omega_{ab})$ is the spectral density of dipoles normalized to the atomic density per volume unit. Finally, the evolution of $\rho(t)$ is given by the Von Neumann equation:

$$i\hbar\frac{\partial\rho}{\partial t} = [\mathcal{H}, \rho] \tag{3.13}$$

This is the equation of motion for the elements of the density matrix. These equations are also known as the optical Bloch equations (OBE) and they will describe both the coherences and the population evolution. In section 3.2.1, I will remind the OBE for an atom interacting with a light field, while in section 3.2.2, the environment will be phenomenologically included.

3.2.1   Interaction between light and a two-level system

Using the formalism presented above, I will first calculate the evolution of the state
when the system is isolated from the environment. To obtain the evolution of the
system, equation (3.13) needs to be solved for the following Hamiltonian:

$$\mathcal{H} = \begin{pmatrix} 0 & d_{ab}E \\ d_{ab}^*E^* & \hbar\omega_{ab} \end{pmatrix} , \tag{3.14}$$

where the electromagnetic field $\vec{E}$ will be written in the following way:

$$\vec{E}(\vec{r},t) = \frac{1}{2}\left(\vec{\epsilon}(\vec{r},t) + \vec{\epsilon}^*(\vec{r},t)\right) = \frac{1}{2}\left(\vec{A}(\vec{r},t)e^{i(\omega_L t - \vec{k}\vec{r})} + \vec{A}^*(\vec{r},t)e^{-i(\omega_L t - \vec{k}\vec{r})}\right) , \tag{3.15}$$

where ω_L is the frequency of the electromagnetic field and $\vec{A}(\vec{r},t)$ is the envelope,
which varies slowly in time and space with respect to $e^{i(\omega_L t - \vec{k}\vec{r})}$. From equation
(3.13), the evolution of the different terms of the density matrix is driven by:

$$\begin{cases} \dot{\rho}_{aa} = i(\rho_{ab} - \rho_{ba})\left(\Omega e^{i(\omega_L t - \vec{k}\vec{r})} + \Omega^* e^{-i(\omega_L t - \vec{k}\vec{r})}\right) \\ \dot{\rho}_{bb} = -\dot{\rho}_{aa} \\ \dot{\rho}_{ab} = i(\rho_{aa} - \rho_{bb})\left(\Omega e^{i(\omega_L t - \vec{k}\vec{r})} + \Omega^* e^{-i(\omega_L t - \vec{k}\vec{r})}\right) + i\omega_{ab}\rho_{ab} \end{cases} \tag{3.16}$$

where $\Omega(\vec{r},t) = \frac{d_{ab}A(\vec{r},t)}{2\hbar}$ is the Rabi frequency, which characterizes the coupling
between the transition and the light field. In order to simplify the resolution of the
equations, a change of variable into a rotating frame is usually performed:

$$\rho_{ab} = \widetilde{\rho}_{ab}e^{i(\omega_L t - \vec{k}\vec{r})} \tag{3.17}$$

This change of variable allows us to neglect the rapid oscillations of the system by
writing equation (3.16) as:

$$\begin{cases} \dot{\rho}_{aa} = i(\widetilde{\rho}_{ab}e^{i(\omega_L t - \vec{k}\vec{r})} - \widetilde{\rho}_{ba}e^{-i(\omega_L t - \vec{k}\vec{r})})\left(\Omega e^{i(\omega_L t - \vec{k}\vec{r})} + \Omega^* e^{-i(\omega_L t - \vec{k}\vec{r})}\right) \\ \dot{\rho}_{bb} = -\dot{\rho}_{aa} \\ (\dot{\widetilde{\rho}}_{ab} + \widetilde{\rho}_{ab}i\omega_L)e^{i(\omega_L t - \vec{k}\vec{r})} = i(\rho_{aa} - \rho_{bb})\left(\Omega e^{i(\omega_L t - \vec{k}\vec{r})} + \Omega^* e^{-i(\omega_L t - \vec{k}\vec{r})}\right) + i\omega_{ab}\widetilde{\rho}_{ab}e^{i(\omega_L t - \vec{k}\vec{r})} \end{cases} \tag{3.18}$$

We define the detuning Δ as the difference between the frequency of resonance of
the transition and the frequency of the laser ($\Delta = \omega_{ab} - \omega_L$). Additionally, the
system of equations (3.18) shows terms in $e^{\pm 2i\omega t}$, which can be neglected by using
the Rotating Wave approximation (RWA). This allows us to suppress the terms
which go as overtones of ω_L as they will average to 0 in any reasonable time scale.

The OBE are then given by:

$$\begin{cases} \dot{\rho}_{aa} = i(\widetilde{\rho}_{ab}\Omega^* - \widetilde{\rho}_{ba}\Omega) + \rho_{bb} \\ \dot{\rho}_{bb} = -\dot{\rho}_{aa} \\ \dot{\widetilde{\rho}}_{ab} = i(\rho_{aa} - \rho_{bb})\Omega + i\Delta\widetilde{\rho}_{ab} \end{cases} \quad (3.19)$$

Equations (3.19) describe the evolution of the coherences and the population under interaction with light. As the two-level system is not isolated, its interactions with the environment should be included in our model. In the next section, I will phenomenologically include relaxation terms to account for it.

3.2.2 Relaxation terms

Processes related to decoherence and population relaxation can be included in the model that describes the system by modifying equation (3.13) with [59]:

$$i\hbar\frac{\partial\rho}{\partial t} = [\mathcal{H}, \rho] + \frac{d\rho}{dt}\bigg|_{\text{relaxation}}, \quad (3.20)$$

where the last term involves the relaxation of the system due to the interaction with the environment. There are two magnitudes that expose this interaction. The first one is related to the population lifetime, called T_1 and defined as $\gamma_{bb} = \frac{1}{T_1}$. The other one is related to the decoherence processes, called T_2 and defined as $\gamma_{ab} = \frac{1}{T_2}$. Including these interactions, equation (3.19) can be rewritten as:

$$\begin{cases} \dot{\rho}_{aa} = i(\widetilde{\rho}_{ab}\Omega^* - \widetilde{\rho}_{ba}\Omega) + \gamma_{bb}\rho_{bb} \\ \dot{\rho}_{bb} = -\dot{\rho}_{aa} \\ \dot{\widetilde{\rho}}_{ab} = i(\rho_{aa} - \rho_{bb})\Omega + (i\Delta - \gamma_{ab})\widetilde{\rho}_{ab} \end{cases} \quad (3.21)$$

As T_2 is limited by the population lifetime T_1 (see equation (2.12)), ρ always remains as a positive operator. We are particularly interested in the evolution of the coherences, given by the non-diagonal terms of the density matrix. The solution can be given by a formal integration of $\dot{\widetilde{\rho}}_{ab}$:

$$\widetilde{\rho}_{ab} = \widetilde{\rho}_{ab_{homog}} + \widetilde{\rho}_{ab_{partic}} = \overbrace{\widetilde{\rho}_{ab}(t_0)e^{(i\Delta - \gamma_{ab})(t-t_0)}}^{\text{Free evolution}} + \overbrace{i\int_{t_0}^{t}\Omega n_{ab}e^{(i\Delta - \gamma_{ab})(t-t')}dt'}^{\text{Interaction field-coherences}}, \quad (3.22)$$

where $n_{ab} = \rho_{aa} - \rho_{bb}$ is the population level.

The first term of equation (3.22) is related to the free evolution of the coher-

ences and the second term, to the interaction with a light field. In the following section, a geometrical interpretation of the problem of the interaction between an atomic system and a light field will be laid out.

3.3   Bloch vector

Although the dynamics of the coherences and the population is described completely by the equations (3.21), a geometrical interpretation is particularly enlightening. A geometrical representation has been given for an electron spin in a constant magnetic field (which is a two-level system) by Bloch in the 40s [41, 60]. This representation of the state evolution is the basis of electron spin resonance and nuclear magnetic resonance. In 1957, Feynman and coworkers shown that this representation can be extended to any two level problem [61].

In this section I will present the optical analog of the spin geometrical representation. This analogy is useful to predict the behavior of the atoms while interacting with a light field.

3.3.1   Geometrical interpretation

In agreement with the spin theory, it is possible to define a 3-vector $\vec{B} = (u, v, w)$, called the Bloch vector, which fully defines the state of the system.

If we consider a pure state $|\psi\rangle = a|a\rangle + b|b\rangle$, the components of the Bloch vector are given by [61]:

$$\begin{cases} u(t) = a(t)b(t)^* + b(t)a(t)^* \\ v(t) = i(a(t)b(t)^* - b(t)a(t)^*) \\ w(t) = a(t)a(t)^* - b(t)b(t)^* \end{cases} \tag{3.23}$$

The definition of the Bloch vector $\vec{B}$ and its components comes from the spin theory. u, v and w are defined by taking the expectation value of the 3 Pauli matrices: $u = \langle\psi|\sigma_x|\psi\rangle$, $v = \langle\psi|\sigma_y|\psi\rangle$ and $w = \langle\psi|\sigma_z|\psi\rangle$; where σ_x, σ_y and σ_z are the Pauli matrices. For mixed states, the Bloch vector is defined as follows:

$$\begin{cases} u = Tr(\sigma_x\rho) \\ v = Tr(\sigma_y\rho) \\ w = Tr(\sigma_z\rho) \end{cases} \tag{3.24}$$

In figure 3.2 the Bloch sphere is shown.
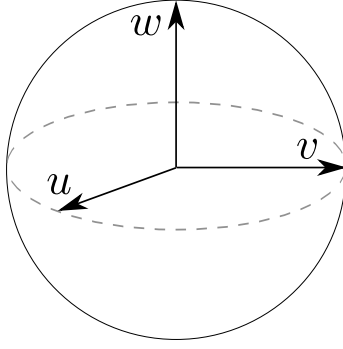
Figure 3.2: Bloch sphere.

Using the equations (3.24) it is possible to find the relation between u, v, w and the elements of the density matrix in the rotating frame:

$$\begin{cases} u(t) = \tilde{\rho}_{ba} + \tilde{\rho}_{ab} \\ v(t) = i(\tilde{\rho}_{ba} - \tilde{\rho}_{ab}) \\ w(t) = \rho_{bb} - \rho_{aa} \end{cases} \tag{3.25}$$

As it was shown in equation (3.12), the macroscopic polarization is calculated from the non diagonal elements of density matrix. Therefore, the elements of $\vec{B}$ can be also used to calculate the macroscopic polarization. Writing ρ_{ab} and ρ_{ba} as a function of the Bloch vector and using equation (3.12), the macroscopic polarization can be written as follows:

$$\vec{P}(t) = d_{ab} \int G(\omega_{ab}) \operatorname{Re}((u(t) + iv(t))e^{i\omega t}) d\omega_{ab}, \tag{3.26}$$

where the term e^{iwt} comes from the fact the u and v are defined in the rotating frame. Additionally, as ρ_{aa} and ρ_{bb} are the population of the ground state and the excited state respectively, $w(t)$ is the population difference. Thus, for example, $w = -1$ means that the ions are in the ground state, while $w = 1$ in the excited state. Finally, using equation (3.21), it is possible to rewrite the OBE with the Bloch vector components:

$$\begin{cases} \dot{u}(t) = -\Delta v(t) - \gamma_{ab} u(t) \\ \dot{v}(t) = \Delta u(t) - \gamma_{ab} v(t) + \Omega w(t) \\ \dot{w}(t) = -\gamma_{bb}(w(t) + 1) - \Omega v(t) \end{cases} \tag{3.27}$$

In the following sections, the effect of different fields on the Bloch vector will be analyzed. Although equation (3.27) can be solved analytically for steady fields [62], I will consider easily solvable situations and their representation on the sphere,

namely the free evolution (or free precession), the Rabi oscillations and the time sequence of the two-pulse photon echo. In the following sections, I will assume that the decoherence and the population decay are negligible ($\gamma_{ab} = 0$ and $\gamma_{bb} = 0$).

3.3.2   Free precession

One case of interest is given by the free evolution of the Bloch vector when no field is applied ($\Omega = 0$). In that case the system is described by:

$$\begin{cases} \dot{u}(t) = -\Delta v(t) \\ \dot{v}(t) = \Delta u(t) \\ \dot{w}(t) = 0 \end{cases} \tag{3.28}$$

If the system is initially set in the following condition $\vec{B}_0 = (u_0, v_0, w_0)$, the solution to the Bloch equations are given by the rotation matrix:

$$\begin{pmatrix} u(t) \\ v(t) \\ w(t) \end{pmatrix} = \begin{pmatrix} \cos(\Delta t) & -\sin(\Delta t) & 0 \\ \sin(\Delta t) & \cos(\Delta t) & 0 \\ 0 & 0 & 1 \end{pmatrix} \begin{pmatrix} u_0 \\ v_0 \\ w_0 \end{pmatrix} \tag{3.29}$$

The Bloch vector precesses around the w-axis. The speed of precession is the detuning Δ.
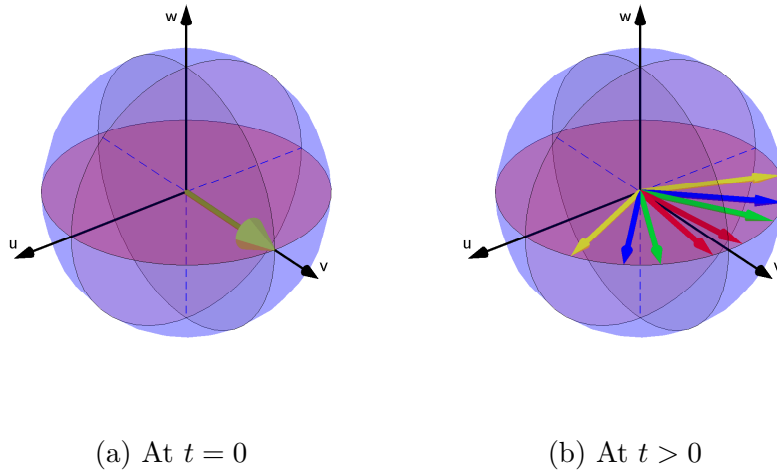

(a) At $t = 0$ (b) At $t > 0$

Figure 3.3: Bloch sphere: in (a) the Bloch vector at $t = 0$ and in (b) the Bloch vector at $t > 0$.

As an example, let's take a Bloch vector on the equatorial plane: $\vec{B}_0 = (0, 1, 0)$; and consider a set of dipoles with different frequencies (different detunings) within

the inhomogeneous broadening. Equation (3.29) predicts that as time evolves, the dipoles will start to dephase (see figure 3.3) represented by different precession speed. This behavior of the coherences is also predicted by the evolution of the non-diagonal terms of the density matrix. When no field is applied on the system, the first term of equation (3.22) explains the free evolution of the system.

3.3.3 Rabi oscillations

Another case of interest is when a constant field is applied on the system. If we only consider on resonance atoms ($\Delta = 0$), the OBE are:

$$
\begin{cases}
\dot{u}(t) = 0 \\
\dot{v}(t) = \Omega w(t) \\
\dot{w}(t) = -\Omega v(t)
\end{cases}
\tag{3.30}
$$

Assuming that the Bloch vector is initially $\vec{B}_0 = (u_0, v_0, w_0)$, the solution to OBE is also given by a rotation matrix:

$$
\begin{pmatrix} u(t) \\ v(t) \\ w(t) \end{pmatrix} = \begin{pmatrix} 1 & 0 & 0 \\ 0 & \cos(\Omega t) & \sin(\Omega t) \\ 0 & -\sin(\Omega t) & \cos(\Omega t) \end{pmatrix} \begin{pmatrix} u_0 \\ v_0 \\ w_0 \end{pmatrix}
\tag{3.31}
$$

The solution shows that the Bloch vector will perform a nutation around the u-axis. The Bloch vector will go back and forth from w_0 to $-w_0$, corresponding to Rabi flopping of the population.

If atoms off resonance were also considered, the behavior of the Bloch vector is not the same. As the detuning is increased, it is harder to achieve the population inversion [47]. In general, the detuning can be neglected only if it is smaller than the driving Rabi frequency. In the case of π-pulses, it is possible to efficiently invert the population depending on the duration of the pulses (i.e. its bandwidth is proportional to the inverse of the duration). If the duration of the pulses is δt and the detuning is Δ, we can fully invert the medium if $\delta t^{-1} >> \Delta$. In this way, the effect of the detuning is not appreciable and we can use (3.31) to calculate the effect of the pulses.

So far we have assumed that the field is constantly applied for a duration t, defining a square pulse. Rabi oscillations are also observed for other type of pulses, such as Gaussian pulses. The behavior of the Bloch vector will be also given by equation (3.31) where Ωt is replaced by the pulse area defined as $\theta = \int \Omega(t) dt$. I will analyze two kind of pulses: $\theta = \pi$, known as π-pulse, and $\theta = \pi/2$, both are

building blocks of the two-pulse photon echo.

For $\theta = \pi$, using equation (3.31) we can see that the components of the Bloch vector are transformed as:

$$
\begin{cases}
u \to u \\
v \to -v \\
w \to -w
\end{cases}
\tag{3.32}
$$

If, for example, the atoms are initially in the ground state $\vec{B}_0 = (0, 0, -1)$, the effect of the π-pulse is to bring all the atoms to the excited state, as shown in figure 3.4.

(a) At $t = 0$ (b) After the π pulse
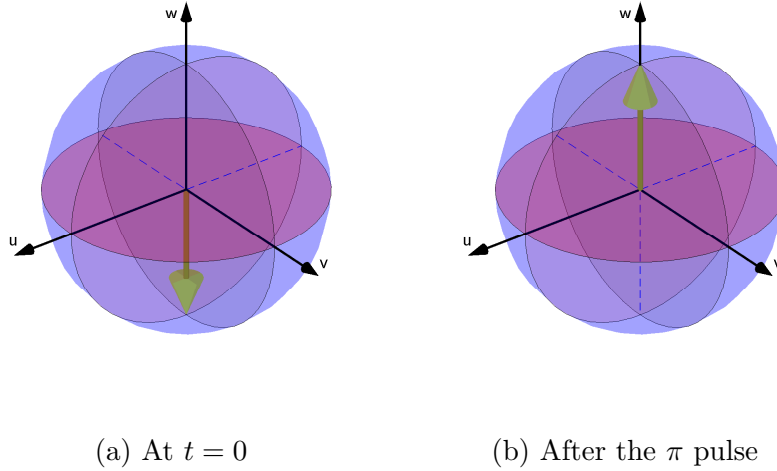
Figure 3.4: Bloch sphere: in (a) the Bloch vector at $t = 0$ and in (b) the Bloch vector after applying the π-pulse.

For $\theta = \pi/2$, using (3.31) we obtain after the $\pi/2$-pulse:

$$
\begin{cases}
u \to u \\
v \to w \\
w \to -v
\end{cases}
\tag{3.33}
$$

If, for example, the atoms are initially in the ground state ($\vec{B}_0 = (0, 0, -1)$), the effect of the $\pi/2$-pulse is to bring the Bloch vector to the equatorial plane, as shown in figure 3.5. As it was pointed out at the beginning of this section, equation (3.22) explains all the dynamics of the system regarding its coherences. The Bloch vector is a different way to study the evolution of the coherences. However, both approaches are linked. The Rabi oscillations presented in this section show how the interaction between an external field and the coherences is done. This interaction is clearly described by the second term of equation (3.22). The Bloch vector is its graphical representation.

(a) At $t = 0$ (b) After the $\pi/2$ pulse
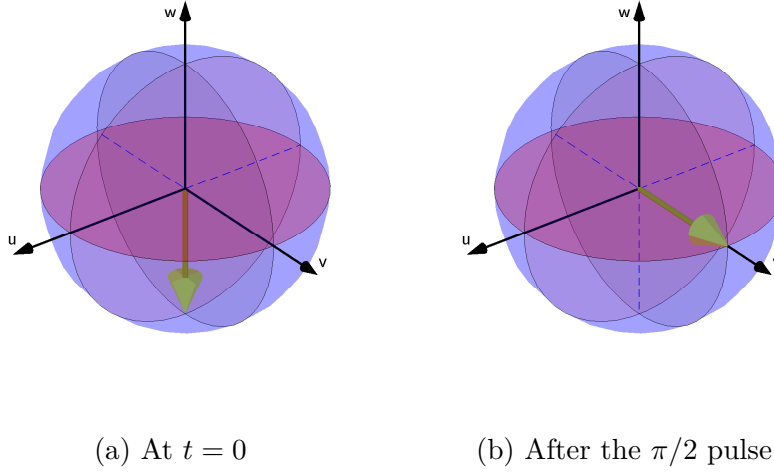
Figure 3.5: Bloch sphere: in (a) the Bloch vector at $t = 0$ and in (b) the Bloch vector after the $\pi/2$-pulse is applied.

In the next section I will present a protocol, the two-pulse photon echo, which is based on Rabi oscillations ($\pi/2$-pulse and π-pulse) and the free precession.

3.3.4 Two-pulse photon echo

Photon echo protocols are an interesting way to control the evolution of the dipoles. A few years after the development of the spin echo in the 50's [63], the photon echo was proposed and observed [64, 65]. The photon echo is based on the excitation of the transition dipole, analogous to the magnetic moment for the spin echo. This is an elegant way to measure the homogeneous linewidth of an inhomogeneous sample.

The two-pulse photon echo protocol uses both the Rabi oscillations and the free precession. In figure 3.6, a time sequence is presented.
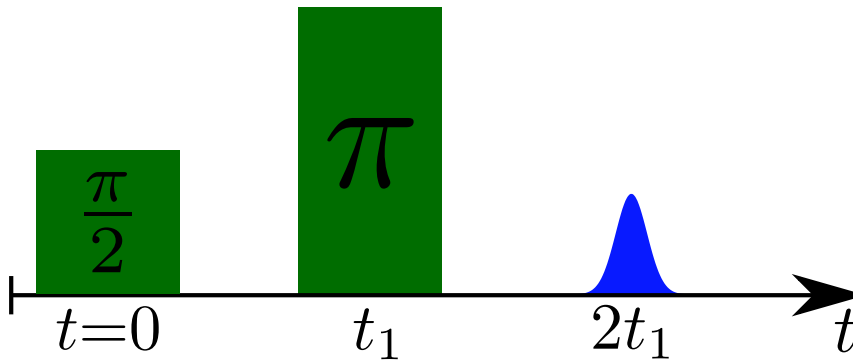
Figure 3.6: Two-pulse photon echo sequence. At $t = 0$, a $\pi/2$ pulse creates a coherent state $|\psi\rangle = \frac{1}{\sqrt{2}}|0\rangle + e^{i\varphi}\frac{1}{\sqrt{2}}|1\rangle$ and the dipoles start to the dephase. At $t = t_1$, a π-pulse is applied to rephase the dipoles, which is achieved at $t = 2t_1$.

First, a $\pi/2$-pulse is applied to create a coherent state $|\psi\rangle = \frac{1}{\sqrt{2}}|0\rangle + e^{i\varphi}\frac{1}{\sqrt{2}}|1\rangle$

(see figure 3.5). Starting from the ground state, the Bloch vector pointing down undergoes a $\pi/2$ rotation on the Bloch sphere to reach $u(0) = 0$, $v(0) = 1$ and $w(0) = 0$ right after the pulse at $t = 0^+$.

From equation (3.29), we can predict how the different dipoles within the inhomogeneous profile will evolve for $t > 0$:

$$
\begin{cases}
u(t) = -\sin(\Delta t) \\
v(t) = \cos(\Delta t) \\
w(t) = 0
\end{cases}
\tag{3.34}
$$

According to equation (3.34), the Bloch vector associated to different inhomogeneous detunings Δ will precess around the axis w at a precession speed Δ.

To illustrate the concept of dephasing, we can consider the evolution of the macroscopic polarization. This latter can be calculated using equation (3.26). For this illustration, I will consider that the pulse spectrally covers the whole inhomogeneous linewidth or, in the time domain, that the pulse duration is much shorter than $1/\Gamma_{inh}$. The inhomogeneous profile is assumed Gaussian (see figure 3.7).
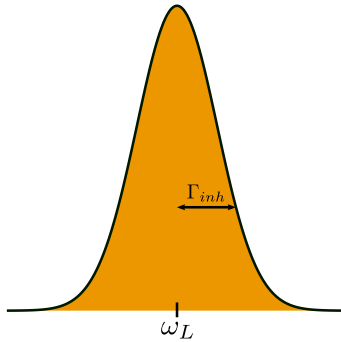
Figure 3.7: Absorption profile of the material with a Gaussian shape.

If the pulse does not cover the whole line, we cannot say that all the dipoles "see" a uniform $\pi/2$-pulse. After the $\pi/2$-pulse is applied, the dipoles will start to dephase as illustrated in figure 3.3. This dephasing modifies the macroscopic polarization which can be analyzed by combining equation (3.26) with (3.34):

$$
P(t) = d_{ab} \int e^{-\frac{\Delta^2}{\Gamma^2}} \mathrm{Re}((\sin(\Delta t) + i\cos(\Delta t))e^{iwt})d\Delta \, ,
\tag{3.35}
$$

If we consider $\Gamma_{inh} = 2\pi \times$ 200 MHz, which is in the order of magnitude of the crystals considered in this work, the macroscopic polarization will be reduced by e^{-1} after a time equal to $2/\Gamma = 0.01\,\mu$s, as equation (3.35) is the Fourier transform of the inhomogeneous Gaussian profile. In figure 3.8, the total polarization as a

function of time is shown. After a time $1/\Gamma_{inh}$, the total polarization vanishes because of the dipoles dephasing.
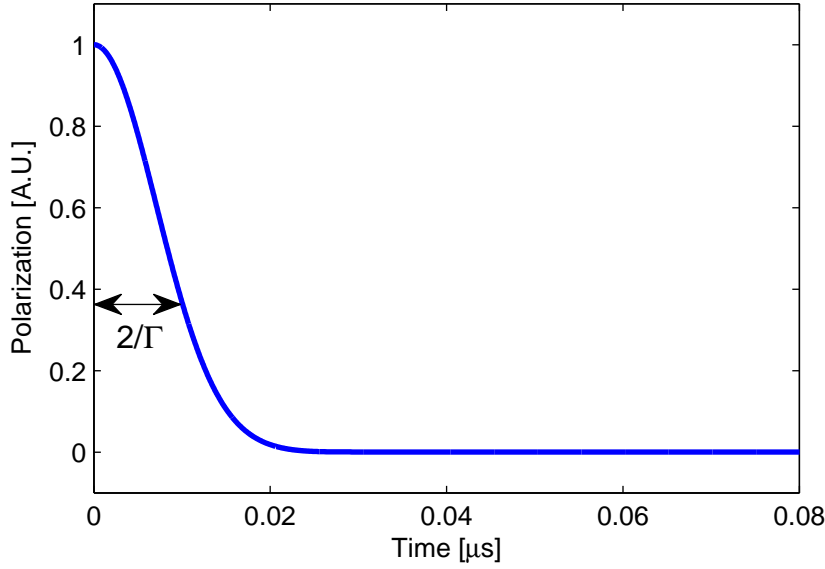
Figure 3.8: Evolution of the macroscopic polarization after a $\pi/2$-pulse.

This effect, known as free induction decay (FID), was first studied in the frame of nuclear magnetic resonance by Hahn [66] and, then, was observed in the optical domain by Brewer [67]. Photon echo protocols can be seen as a reconstruction of the polarization by rephasing the dipoles.

In order to revert the dephasing process, a π-pulse is applied at $t = t_1$.

(a) At $t = t_1$ (b) At $t = 2t_1$
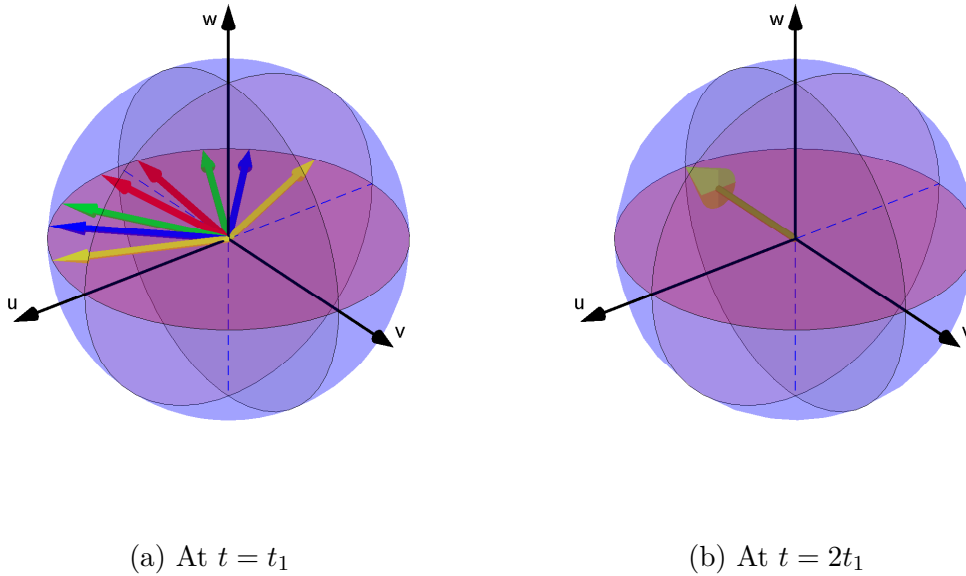
Figure 3.9: Bloch sphere: the Bloch vector at $t = t_1$ (a) and at $t = 2t_1$ (b).

The Bloch vector undergo a rotation of 180° around the w-axis (see figure 3.9):

$$\begin{cases} u(t_1) = \sin(\Delta t_1) \\ v(t_1) = -\cos(\Delta t_1) \\ w(t_1) = 0 \end{cases} \tag{3.36}$$

From t_1, the dipoles freely evolve. We can study how the system will evolve by finding the solution of equations (3.28) with the initial condition given by (3.36):

$$\begin{cases} u(t) = \sin(\Delta t_1)\cos(\Delta(t-t_1)) - \cos(\Delta t_1)\sin(\Delta(t-t_1)) \\ v(t) = -\sin(\Delta t_1)\sin(\Delta(t-t_1)) - \cos(\Delta t_1)\cos(\Delta(t-t_1)) \\ w(t) = 0 \end{cases} \tag{3.37}$$

Rearranging the sinus and the cosinus, it is possible to rewrite the solution in the following way:

$$\begin{cases} u(t) = \sin((2t_1 - t)\Delta) \\ v(t) = \cos((2t_1 - t)\Delta) \\ w(t) = 0 \end{cases} \tag{3.38}$$

Independently of the value of the detuning Δ, all the dipoles will be in phase again at $t = 2t_1$, as shown in figure 3.10.
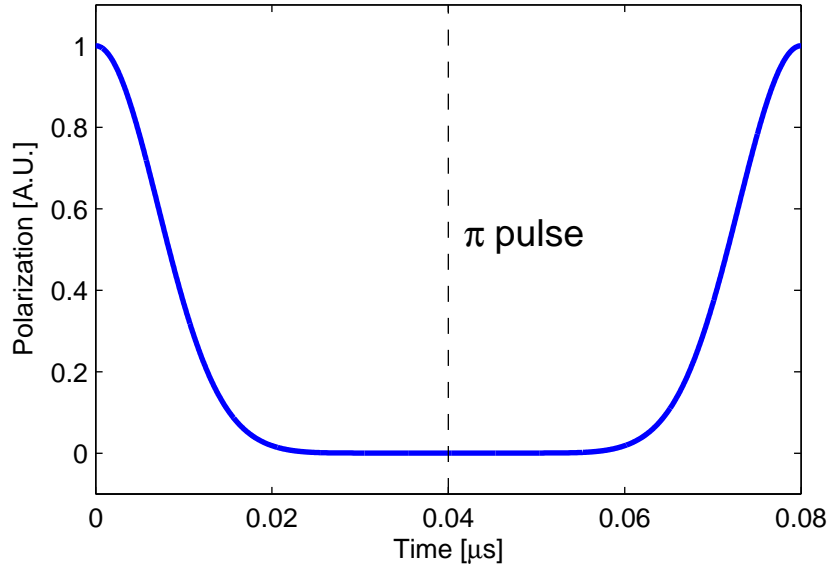
Figure 3.10:   Macroscopic polarization as a function of time after. At t=0 a $\pi/2$ pulse is applied and at $t = 0.04\mu$s a π-pulse is applied.

Thus, the effect of the π-pulse can be considered as a time reversal: $\Delta t \rightarrow -\Delta t$.

The two-pulse photon echo presented in this section shows a way to control the evolution of a matter state. The tools presented here are the basis of the photon echo protocols used to store information.

The propagation of the different pulses including the echo has not been considered so far. In the next chapter, I will analyze how the pulses are absorbed and, more generally, how they propagate through the medium in order to quantify the efficiency of the process from the point of view of information storage.

Propagation

CHAPTER 1: Quantum memories in solids	CHAPTER 2: Rare-earth ions in solids	CHAPTER 3: Light-matter interaction	**CHAPTER 4:** **Propagation**	CHAPTER 5: Revival of silenced echo (ROSE)
CHAPTER 10: New erbium doped materials	CHAPTER 9: ROSE with a few photons	CHAPTER 8: ROSE bandwidth	CHAPTER 7: ROSE efficiency	CHAPTER 6: Experimental set-up
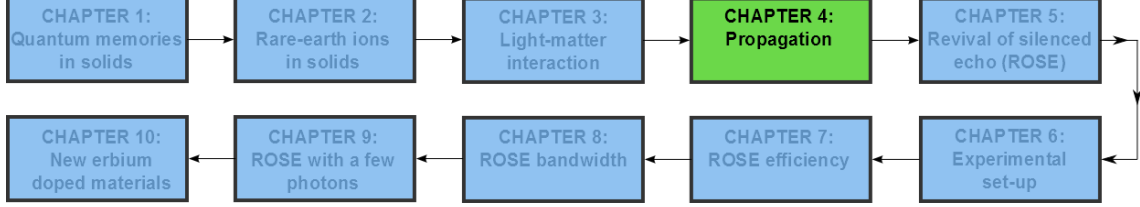
In the former section, the interaction between light and matter was presented. As it was shown, a light state can be converted into a matter state because of the interaction of the dipoles with a light field. The polarization shows how the dipoles store the information of the incoming field. Controlling the evolution of the dipoles is a possible way to restore the information as a light state. This is done through the radiative response of the medium.

In this chapter I will introduce the pulse propagation that I have neglected so far. This analysis will be done using the Maxwell equations that relate the polarization of the medium and the output field of an optical thick sample. The propagation of a weak pulse will be analyzed first in order to see how the information carried by the pulse is absorbed by a crystal. Then, two protocols to store and retrieve the information will be presented. First, the two-pulse photon echo in which the first pulse is now weak and, then, a variation of this protocol which I call double inversion photon echo.

4.1 Derivation of the propagation equations

To analyze the radiative response of an optical thick medium it is necessary to introduce the Maxwell equations using the polarization. The Maxwell equations for a dielectric material are given by:

$$\nabla \vec{D}(\vec{r},t) = \rho$$

$$\nabla \times \vec{E}(\vec{r},t) = -\frac{\partial \vec{B}(\vec{r},t)}{\partial t}$$

$$\nabla \vec{B}(\vec{r}, t) = 0$$

$$\nabla \times \vec{E}(\vec{r}, t) = \frac{1}{c^2} \frac{\partial \vec{E}(\vec{r}, t)}{\partial t} + j$$

Additionally, $\rho = 0$, $j = 0$ and $\vec{D}(\vec{r}, t) = \epsilon_0 \vec{E}(\vec{r}, t) + \vec{P}(\vec{r}, t)$. Thus, the only source term for the fields comes from the polarization $\vec{P}$. The wave equation for the electric field reads as:

$$\nabla^2 \vec{E}(\vec{r}, t) - \frac{\partial^2 \vec{E}(\vec{r}, t)}{\partial t^2} = \mu_0 \frac{\partial^2 \vec{P}(\vec{r}, t)}{\partial t^2} \tag{4.1}$$

We assume that medium will interact linearly with the electromagnetic field and that they are related by a constitutive relation [68]:

$$\vec{P}(\omega) = \epsilon_0 \chi(\omega) \vec{E}(\omega) \tag{4.2}$$

To use this relation between $\vec{P}$ and $\vec{E}$ we need to convert the wave equation (4.1) from the time domain to the frequency domain:

$$\nabla^2 \vec{E}(\vec{r}, \omega) + k^2 \vec{E}(\vec{r}, \omega) = \omega^2 \vec{P}(\vec{r}, \omega) \tag{4.3}$$

This equation can be solved to obtain the output field. However, it is possible to simplify it by using the slowly varying envelope approximation (SVEA). We consider that the field $\vec{E}$ is the product of an envelope that varies little over the period or frequency considered, multiplied by an exponential which includes the rapid oscillations (see equation (3.15)).

Writing the field $\vec{E}(r, \omega) = A(\vec{r}, \omega) e^{-i \vec{k}\vec{r}}$, the SVEA approximation can be summarized as follows:

$$\left| \nabla^2 A \right| \ll |k \nabla A| \tag{4.4}$$

Using this approximation equation (4.3) becomes:

$$\nabla A(\vec{r}, \omega) e^{-i \vec{k}\vec{r}} = \omega^2 P(\vec{r}, \omega) \tag{4.5}$$

The pulse propagation analysis is simplified. In the next section I will use it to study the absorption of a weak pulse.

4.2   Propagation of a small area pulse

First of all, I will analyze what happens when a small area pulse, much smaller than a π-pulse, is sent to a crystal of length L, as depicted in figure 4.1. I will consider the evolution of the coherences by using equation (3.22).
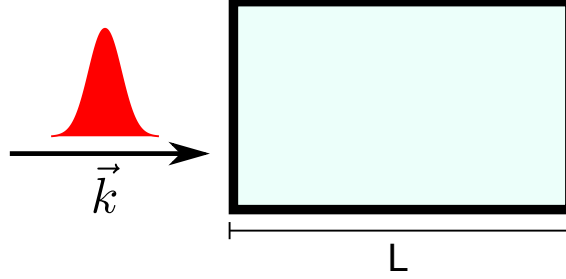
Figure 4.1:   A small area pulse is sent to a crystal of length L.

Initially, the atoms are in the ground state: $\tilde{\rho}_{ab}(t_0) = 0$ and $n_{ab}(t_0) = -1$. If the input pulse is weak enough, the population is unaffected (weak area pulse condition): $n_{ab}(t) = -1$ for $t > t_0$. Therefore, only the second term of equation (3.22) will contribute to the coherences:

$$\tilde{\rho}_{ab}(\omega_{ab}, \vec{r}, t) = -\frac{id_{ab}}{2\hbar} \int_{t_0}^{t} dt' A(\vec{r}, t') e^{(i\Delta - \gamma_{ab})(t - t')} , \tag{4.6}$$

where $\Omega(\vec{r}, t)$ was replaced by $d_{ab}A(\vec{r}, t)/2\hbar$. Multiplying by $e^{i(\omega_L(t-t') - \vec{k}\vec{r})}$, the coherences in the non-rotating frame (ρ_{ab}) can be easily calculated. As in section 3.3.4, in order to understand the behavior of the system, the macroscopic polarization needs to be calculated using equation (3.12):

$$\vec{P}(\vec{r}, t) = \frac{id_{ab}^2}{2\hbar} \int_{t_0}^{t} dt' \vec{\epsilon}(\vec{r}, t') e^{-\gamma_{ab}(t-t')} \int d\omega_{ab} G(\omega_{ab}) e^{i\omega_{ab}(t-t')} , \tag{4.7}$$

where $A(\vec{r}, t)e^{-i\vec{k}\vec{r}}$ has been replaced by $\vec{\epsilon}(\vec{r}, t)$. The real part of equation (4.7) should be taken to analyze the evolution of the polarization, but I decide not to write it explicitly to simplify the notation. In practice, the signal bandwidth is smaller than the inhomogeneous broadening of the medium. With this assumption, it is worth multiplying by $e^{i\omega_L(t-t')}$ and $e^{-i\omega_L(t-t')}$ to obtain something that goes as the difference $\omega_{ab} - \omega_L$:

$$\vec{P}(\vec{r}, t) = \frac{id_{ab}^2}{2\hbar} \int_{t_0}^{t} dt' \vec{\epsilon}(\vec{r}, t') e^{-\gamma_{ab}(t-t')} e^{i\omega_L(t-t')} \int d\omega_{ab} G(\omega_{ab}) e^{i(\omega_{ab} - \omega_L)(t-t')} \tag{4.8}$$

For the frequency integral, we can say that it will peak around $\omega_{ab} \approx \omega_L$:

$$\vec{P}(\vec{r},t) = \frac{id_{ab}^2}{2\hbar} \int_{t_0}^{t} dt' \vec{\epsilon}(\vec{r},t') e^{-\gamma_{ab}(t-t')} e^{i\omega_L(t-t')} G(\omega_L) 2\pi\delta(t-t') \tag{4.9}$$

To simplify the time integral, we will assume that the coherence time (γ_{ab}^{-1}) is much longer than the duration of the pulses $(e^{-\gamma_{ab}(t-t')} \approx 1)$. Finally, we obtain:

$$\vec{P}(\vec{r},t) = \frac{i\pi d_{ab}^2}{2\hbar} G(\omega_L) \vec{\epsilon}(\vec{r},t) \tag{4.10}$$

In order to use the propagation equation (4.5), we rewrite the previous result in the frequency domain:

$$\vec{P}(\vec{r},\omega) = i\pi \frac{d_{ab}^2}{2\hbar} G(\omega_L) \vec{\epsilon}(\vec{r},\omega) \tag{4.11}$$

Combining equation (4.11) and equation (4.5), and looking for a solution of the type $\vec{\epsilon}(\vec{r},\omega) = \vec{A}(z,\omega)e^{-ikz}$:

$$\frac{\partial A(z,t)}{\partial z} e^{-ikz} = -\omega^2 \mu_0 \pi \frac{d_{ab}^2}{2\hbar} G(\omega_L) A(z,t) e^{-ikz} \tag{4.12}$$

Using that $c = 1/\sqrt{\mu_0\epsilon_0}$ and $k = \omega/c$, we write:

$$\frac{\partial A(z,t)}{\partial z} e^{-ikz} = -\frac{1}{2} \overbrace{\frac{\pi k d_{ab}^2}{\hbar\epsilon_0} G(\omega_L)}^{\alpha} A(z,t) e^{-ikz} \ , \tag{4.13}$$

where the absorption coefficient is defined as follows:

$$\alpha = \frac{\pi k d_{ab}^2}{\hbar\epsilon_0} G(\omega_L) \tag{4.14}$$

Integrating equation (4.13) we can see how a signal is absorbed by the medium with a coefficient α:

$$\frac{\partial A}{\partial z} = -\frac{1}{2}\alpha A \Rightarrow A(z,\omega) = e^{-\frac{1}{2}\alpha_0 z} A(0,\omega) \tag{4.15}$$

Therefore, the field ϵ can be written as:

$$\epsilon(z,\omega) = \epsilon(0,\omega) e^{-\frac{1}{2}\alpha z} e^{-ikz} \tag{4.16}$$

And for the intensity in the time domain:

$$I(z,t) = I(0,t) e^{-\alpha z} \tag{4.17}$$

Equation (4.17) shows how a pulse is absorbed by the crystal. This is the information

that we want to store. The exponential decay that the input pulse suffers is the Beer's law. In figure 4.2 the process is depicted. Depending on the strength and the density of the dipoles and the frequency of the laser respect to the frequency of resonance, the absorption that the input pulse suffers will be different.
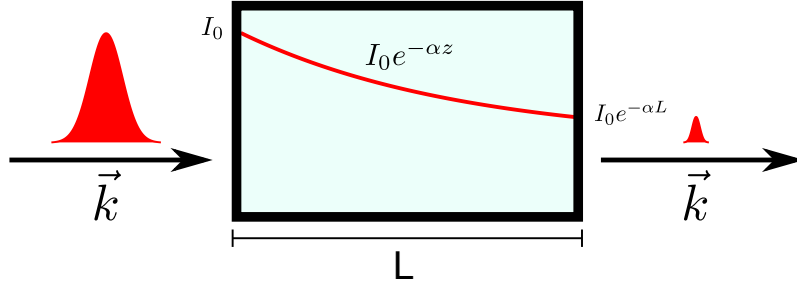
Figure 4.2: Scheme of the absorption process of a weak pulse while it passes through a crystal. α is the absorption coefficient and αL the optical depth.

A weak pulse vanishes into the medium. The information that it contains is not lost but it is actually stored in the coherences. In the next section, I will show how to retrieve this information.

4.3   Propagation of two-pulse photon echo

In this section, I will show how to control the evolution of the coherences in order to retrieve the information stored in the medium. The two-pulse photon echo sequence presented in section 3.3.4 can be adapted to store information, replacing the first $\pi/2$-pulse by a small area pulse. The scheme of the sequence is the following (see figure 4.3):

1. the signal to be stored is sent at $t = t_1$.

2. the rephasing pulse is sent at $t = t_2$.

3. the echo is emitted at $t_3 = 2t_2 - t_1$.

Regarding the pulse to be stored, a few considerations will be done:

- Its area is small: The area of the signal will be much smaller than the one from a π-pulse. Thus, as in the former section, I will consider that after the pulse is absorbed by the medium the population remains in the ground state $(n_{ab} = -1)$.

- Its bandwidth is much smaller than the inhomogeneous linewidth.

- The rephasing pulse covers the region excited by the signal both spectrally and spatially, in such way that all the atoms excited by the signal "feel" the same field for the rephasing pulse. Although π-pulses are deformed while propagating through an absorbing medium [69], the inversion quality does not have a strong dependence on the optical depth of the medium [70]. Thus, the deformation of the π-pulse is not considered here.
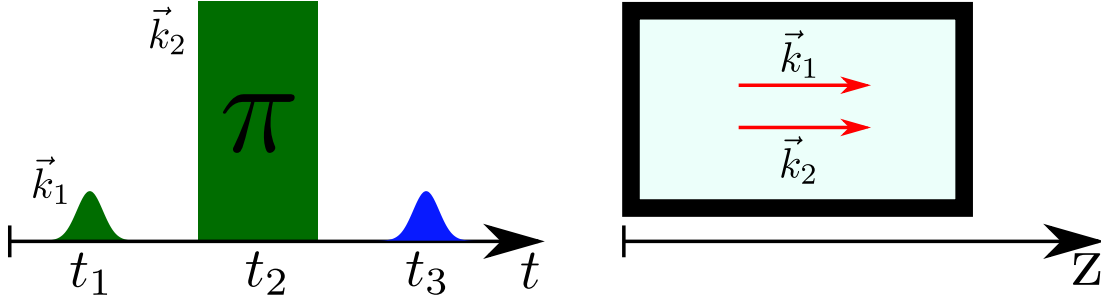
Figure 4.3: Scheme of the two-pulse photon echo protocol. At t_1 a small pulse is sent to the medium and, at t_2, a π-pulse is applied. Both pulses have the same wavevector (direction).

The procedure to calculate the output field is similar to the one presented in section 4.2. First, the coherences will be considered and, then, the polarization. Finally, the Maxwell equation will be solved to obtain the retrieval efficiency (amplitude of the echo).

Using equation (3.22) we can calculate the coherences. The first term of this equation can be disregard because $\widetilde{\rho}_{ab}(t_0) = 0$ as the atoms are initially in the ground state. The coherences before applying the π-pulse can be written as follows:

$$\widetilde{\rho}_{ab}(\omega_{ab}, \vec{r}, t_2^-) = \frac{i d_{ab}}{2\hbar} \int_{t_2}^{\infty} dt' A_{in}(\vec{r}, t') e^{(i\Delta - \gamma_{ab})(t_2 - t')} \,, \tag{4.18}$$

where t_2^- has been used to reference the time just before t_2 and $\Omega(\vec{r}, t)$ was replaced by $d_{ab} A_{in}(\vec{r}, t)/\hbar$.

It is possible to visualize the effect of the first pulse by looking at the Bloch sphere in figure 4.4. For $t < t_1$, the Bloch vector is pointing down and, at $t = t_1$, the input pulse arrives. Afterwards, the dipoles start to dephase because of the inhomogeneous broadening.

At $t = t_2$, a π-pulse is applied in order to revert the evolution and get the dipoles in phase. The effect of the π-pulse is to conjugate the coherences, turning $\omega_{ab}(t_2 - t_1)$ into $-\omega_{ab}(t_2 - t_1)$. In figure 4.5, the Bloch sphere is shown after applying the π-pulse on the left and, on the right, the rephasing achieved a time later.
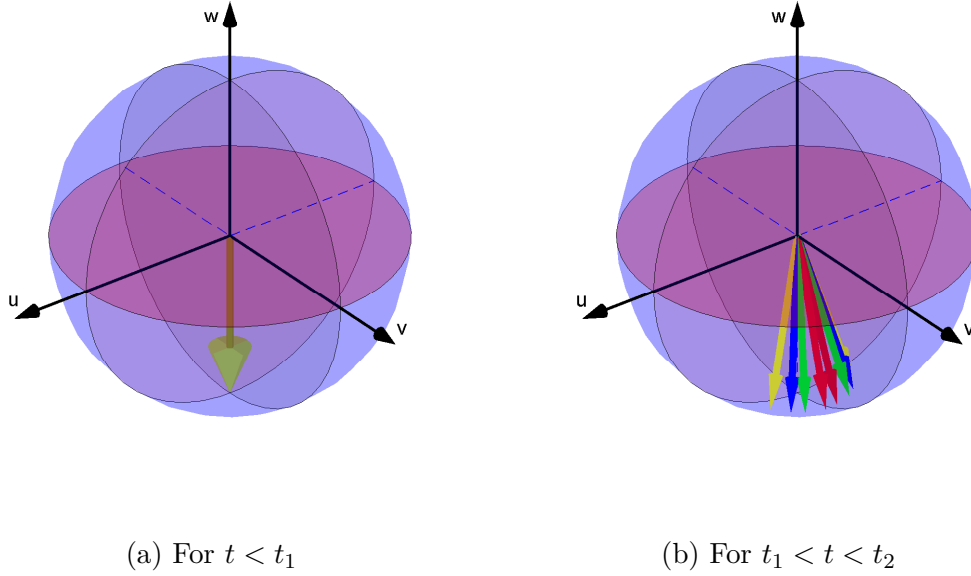
(a) For $t < t_1$ (b) For $t_1 < t < t_2$

Figure 4.4: Bloch sphere: in (a) the Bloch vector for $t < t_1$ and in (b) the Bloch vector for $t_1 < t < t_2$.

(a) For $t_2 < t < 2t_2 - t_1$ (b) At $t = 2t_2 - t_1$
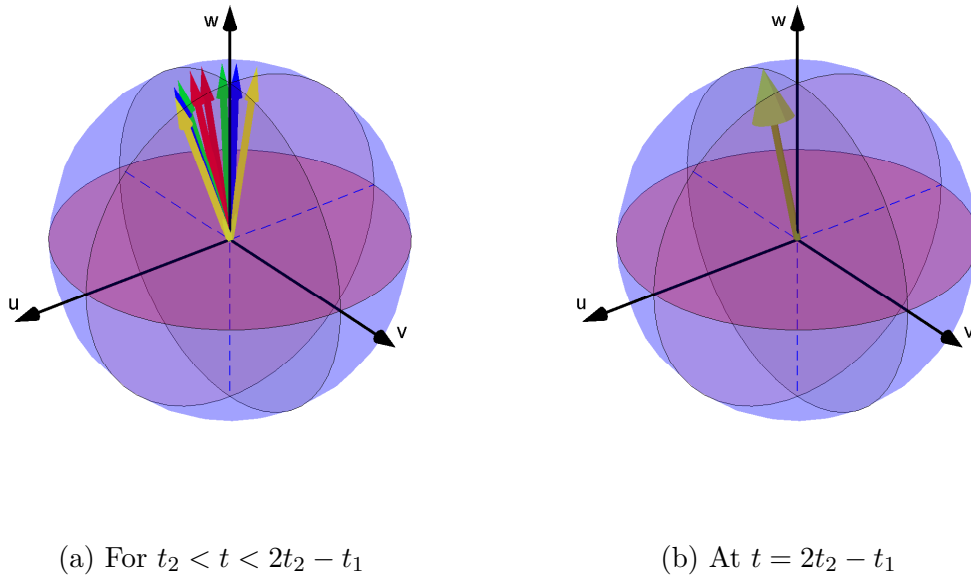
Figure 4.5: Bloch sphere: in (a) the Bloch vector for $t_2 < t < 2t_2 - t_1$ and in (b) the Bloch vector at $t = 2t_2 - t_1$.

For the coherences, we can write the effect of the π-pulse at $t = t_2$ as a conjugation:

$$\widetilde{\rho}_{ab}(\omega_{ab}, \vec{r}, t_2^+) = \widetilde{\rho}_{ba}(\omega_{ab}, \vec{r}, t_2^-) \,, \tag{4.19}$$

where t_2^+ has been used to reference the time after t_2. Then, we use equation (3.22) to calculate the evolution after t_2. This latter should include the output field A_{out}

that is emitted later on.

$$\tilde{\rho}_{ab}(\omega_{ab}, \vec{r}, t) = \tilde{\rho}_{ab}(\omega_{ab}, \vec{r}, t_2^+)e^{(i\Delta - \gamma_{ab})(t - t_2)} + \frac{id_{ab}}{2\hbar}\int_{t_2}^{t} dt' A_{out}(\vec{r}, t')e^{(i\Delta - \gamma_{ab})(t - t')} \quad (4.20)$$

This is the equation we have to solve to obtain the coherences as a function of time. At the boundary t_2, we connect equations (4.18) and (4.19) with equation (4.20). The conjugation of equation (4.18) leads to coherences at t_2^+:

$$\tilde{\rho}_{ab}(\omega_{ab}, \vec{r}, t_2^+) = (\tilde{\rho}_{ab}(\omega_{ab}, \vec{r}, t_2^-))^* = \frac{-id_{ab}}{2\hbar}\int_{-\infty}^{t_2} dt' A_{in}^*(\vec{r}, t')e^{(-i\Delta - \gamma_{ab})(t_2 - t')} \quad (4.21)$$

As we want to calculate the coherences $\rho_{ab}(t)$, we have to multiply this last equation by $e^{i(w_L(t-t_2) - \vec{k}\vec{r})}$ and, using equation (3.15) for the fields, we obtain:

$$\rho_{ab}(\omega_{ab}, \vec{r}, t) = \frac{-id_{ab}}{2\hbar}\int_{-\infty}^{t_2} dt' \epsilon_{in}^*(\vec{r}, t')e^{i\omega_{ab}(t+t'-2t_2)}e^{-\gamma_{ab}(t-t')} + \frac{id_{ab}}{2\hbar}\int_{t_2}^{t} dt' \epsilon_{out}(\vec{r}, t')e^{(i\omega_{ab} - \gamma_{ab})(t-t')}, \quad (4.22)$$

where ϵ_{out} represents the field radiated by the atoms after t_2.

As in section 3.3.4, the physical quantity we are interested in is the macroscopic polarization. To calculate it we can use equation (3.12). In equation (4.22) there are two terms. The first term is related to the free precession of the coherences and the second term related to the interaction with the field. Let's start studying the polarization of the first term which I will call P_1:

$$P_1(\vec{r}, t) = \frac{id_{ab}^2}{2\hbar}\int_{-\infty}^{t_2} dt' \epsilon_{in}^*(\vec{r}, t')e^{-\gamma_{ab}(t-t')}\int d\omega_{ab}G(\omega_{ab})e^{i\omega_{ab}(t+t'-2t_2)} \quad (4.23)$$

Taking into account that the signal bandwidth is much smaller than the inhomogeneous broadening of the medium and that the coherence time (inverse of γ_{ab}) is much longer than the duration of the pulses, the polarization can be written in the following way:

$$P_1(\vec{r}, t) = \frac{i\pi d_{ab}^2}{\hbar}G(\omega_L)\epsilon_{in}^*(\vec{r}, 2t_2 - t)e^{-2\gamma_{ab}(t-t_2)} \quad (4.24)$$

Now we have to look at the second term of the equation (4.22), which I will call P_2:

$$P_2(\vec{r}, t) = -\frac{id_{ab}^2}{2\hbar}\int_{t_2}^{t} dt' \epsilon_{out}(\vec{r}, t')e^{-\gamma_{ab}(t-t')}\int d\omega_{ab}G(\omega_{ab})e^{-i\omega_{ab}(t-t')} \quad (4.25)$$

For the same reasons used to obtain P_1, P_2 can be written as:

$$P_2(\vec{r}, t) = -i\pi\frac{d_{ab}^2}{2\hbar}G(\omega_L)\epsilon_{out}(\vec{r}, t) \quad (4.26)$$

If we combine P_1 and P_2 we obtain:

$$P(\vec{r}, t) = P_1(\vec{r}, t) + P_2(\vec{r}, t) = -i\pi \frac{d_{ab}^2}{2\hbar} G(\omega_L) \left[\epsilon_{out}(\vec{r}, t) - 2\epsilon_{in}^*(\vec{r}, t) e^{-2\gamma_{ab}(t_2-t_1)} e^{-2i\omega t_2} \right] \quad (4.27)$$

To derive the echo propagation using equation (4.5), equation (4.27) should be written in the frequency domain. In the case of $P_2(r, t)$ (equation (4.26)), its Fourier transform is:

$$P_2(\vec{r}, \omega) = -i\pi \frac{d_{ab}^2}{2\hbar} G(\omega_L) \epsilon_{out}(\vec{r}, \omega) \quad (4.28)$$

For $P_1(r, t)$, the Fourier transform is given by:

$$P_1(\vec{r}, \omega) = \frac{i\pi d_{ab}^2}{\hbar} G(\omega_L) e^{-2\gamma_{ab}(t_2-t_1)} e^{-2i\omega t_2} \epsilon_{in}^*(\vec{r}, \omega) \quad (4.29)$$

Combining equations (4.29) and (4.28), the total polarization in the frequency domain can be written as:

$$P(\vec{r}, w) = -i\pi \frac{d_{ab}^2}{2\hbar} G(\omega_L) \left[\epsilon_{out}(\vec{r}, \omega) - 2\epsilon_{in}^*(\vec{r}, \omega) e^{-2\gamma_{ab}(t_2-t_1)} e^{-2i\omega t_2} \right] \quad (4.30)$$

We look for a solution of the Maxwell equation (equation (4.5)) of the type $\epsilon_{out}(\vec{r}, \omega) = \vec{A}(z, \omega) e^{-ikz}$, using that $\alpha = \frac{\pi k d_{ab}^2}{2\hbar\epsilon_0} G(\omega_L)$, we obtain:

$$\frac{\partial A(z, \omega)}{\partial z} e^{-ikz} = \frac{1}{2}\alpha \left[A(z, \omega) e^{-ikz} - 2A_{in}^*(\vec{r}, \omega) e^{-i(\omega_L t - \vec{k}\vec{r})} e^{-2\gamma_{ab}(t_2-t_1)} e^{-2i\omega t_2} \right] \quad (4.31)$$

This fundamental propagation equation connects the amplitude of the incoming pulse and the outgoing echo. Using equation (4.16) for the field ϵ_{in} and integrating from 0 to z, the echo amplitude at the output of the crystal reads as:

$$A(z, \omega) = -A_{in}^*(0, \omega) e^{-i\omega_L t} e^{-2\gamma_{ab}(t_2-t_1)} e^{-2i\omega t_2} 2\sinh\left(\frac{\alpha z}{2}\right) \quad (4.32)$$

Or equivalently in the time domain:

$$A(z, t) = A_{in}^*(0, 2t_2 - t) e^{-i\omega_L(2t_2-t)} e^{-2\gamma_{ab}(t_2-t_1)} 2\sinh\left(\frac{\alpha z}{2}\right) \quad (4.33)$$

Equation (4.33) shows that the echo is release at $t = 2t_2 - t_1$ as $A_{in}^*(0, 2t_2 - t)$ is centered at $t = t_1$. It is now possible to calculate the efficiency η of the protocol:

$$\eta = \left[2\sinh\left(\frac{\alpha z}{2}\right) \right]^2, \quad (4.34)$$

where the decoherences processes have not been considered ($\gamma_{ab} = 0$). In figure 4.6 a scheme of the two-pulse photon echo protocol is shown.
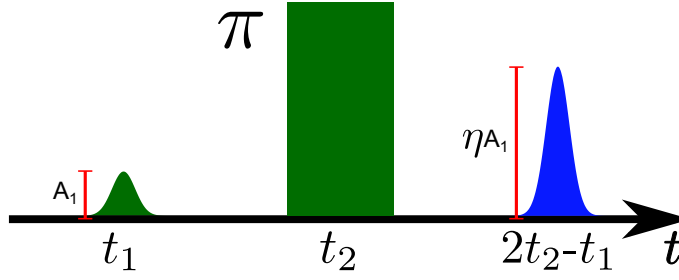
Figure 4.6: Scheme of the two-pulse photon echo with a weak input pulse. The echo is released at $t = 2t_2 - t_1$ with an efficiency η.

And the efficiency, given by equation (4.34), is shown in figure 4.7.
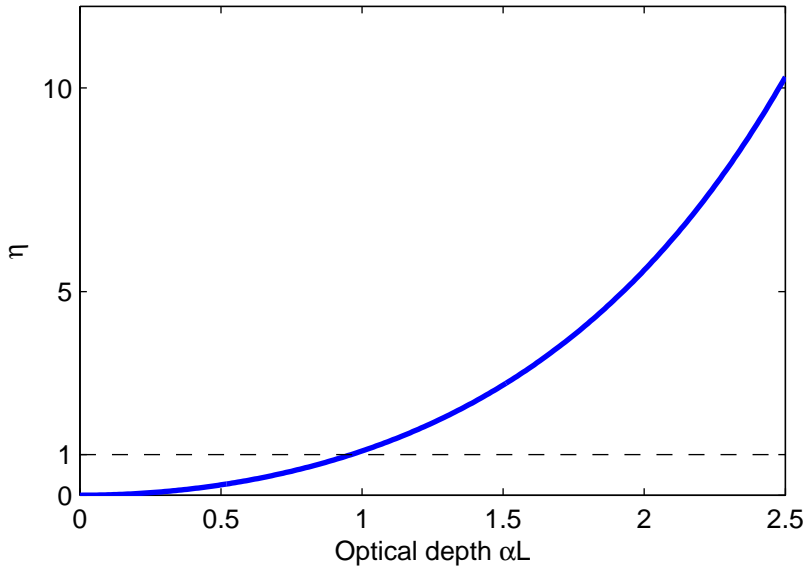
Figure 4.7: Efficiency as a function of the absorption for the two-pulse photon echo protocol without including decoherence $(\gamma_{ab} = 0)$.

Finally, the coherences for any time $t > t_2$ are given by:

$$
\rho_{ab}(\omega_{ab}, \vec{r}, t) = \frac{-id_{ab}}{2\hbar} e^{-\gamma_{ab}(t-t_1)} \left[\int_{-\infty}^{2t_2-t} dt' \epsilon_{in}^*(\vec{r}, t') e^{i\omega_{ab}(t+t'-2t_2)} + \right.
$$

$$
\left. 2\sinh\left(\frac{\alpha z}{2}\right) \int_{2t_2-t}^{t_2} dt' \epsilon_{in}^*(0, t') e^{i\omega_{ab}(t+t'-2t_2)} \right] \tag{4.35}
$$

This modified version of the two-pulse echo protocol has been studied to store information as the echo is proportional to the input pulse [71, 72]. It cannot be used to store quantum information [73] because it is possible to have an efficiency greater than one. This means that the initial state is amplified. Because of the no-cloning theorem [74], a quantum state cannot be copied. The amplification comes from the

fact that the echo is emitted in an inverted medium, as the π-pulse bring all the ions to the excited state. The π-pulse is necessary to achieve the rephasing of the coherences. Thus, the amplification cannot be avoided.

In the next section a variation of the protocol is presented in order to have an echo emitted with all the atoms in the ground state.

4.4 Propagation of double inversion photon echo

To avoid the emission of the echo with the atoms in the excited state, it is possible to apply another π-pulse to bring the atoms back to the ground state.
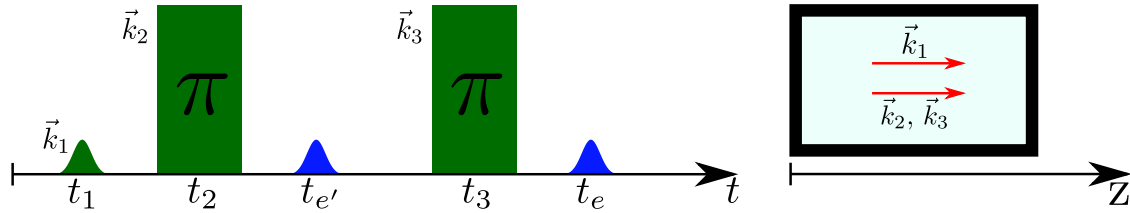
Figure 4.8: Scheme of the three-pulse photon echo protocol. At t_1 a small pulse is sent to the medium, at t_2 the first π-pulse and at t_3 the second π-pulse is applied.

The scheme of this protocol is described as follows (see figure 4.8):

1. the signal to be stored is sent at $t = t_1$.

2. the first rephasing pulse is sent at $t = t_2$.

3. a first echo is emitted at $t_{e'} = 2t_2 - t_1$.

4. the second rephasing pulse is sent at $t = t_3$.

5. a second echo is emitted at $t_e = 2t_3 - 2t_2 - t_1$.

To calculate the evolution of the coherences, equation (3.22) needs to be used again. As in the former section a few considerations, for the pulse to be stored and the rephasing pulses, will be done:

- The input pulse area is small so the population is not modified and keeps the constant value $n_{ab} = -1$.

- The input bandwidth is much smaller than the inhomogeneous linewidth.

- The rephasing pulses cover the region excited by the signal both spectrally and spatially, in such way that all the atoms excited by the signal "feel" the same field for the rephasing pulses. As in the former section, the deformation

that a π-pulse suffers while propagating through an absorbing medium [69] is not considered.

I will start using the value of the coherences obtained in the last section and I will consider the effect of applying another π-pulse that will bring back the atoms in the ground state and rephase the coherences once again. From equation (4.35) we obtain the coherences at $t = t_3^-$, the time when the second π-pulse is applied on the system:

$$\rho_{ab}(\omega_{ab}, \vec{r}, t_3^-) = \frac{-id_{ab}}{2\hbar} e^{-\gamma_{ab}(t_3 - t_1)} \left[\int_{-\infty}^{2t_2 - t_3} dt' \epsilon_{in}^*(\vec{r}, t') e^{i\omega_{ab}(t_3 + t' - 2t_2)} + \right.$$
$$\left. 2\sinh\left(\frac{\alpha z}{2}\right) \int_{2t_2 - t_3}^{t_2} dt' \epsilon_{in}^*(0, t') e^{i\omega_{ab}(t_3 + t' - 2t_2)} \right] \quad (4.36)$$

A second π-pulse inversion is applied at $t = t_3$ so the value of n_{ab} should then be -1. Also, at $t = t_3$, we have to conjugate $\tilde{\rho}_{ab}$ in order to revert the dephasing process. Thus, the coherences after the second π-pulse are given by:

$$\rho_{ab}(\omega_{ab}, \vec{r}, t) = \rho_{ab}(\omega_{ab}, \vec{r}, t_3^+) e^{(i\omega_{ab} - \gamma_{ab})(t - t_3)} - \frac{id_{ab}}{2\hbar} \int_t^{t_3} dt' \epsilon_{out}(\vec{r}, t') e^{(i\omega_{ab} - \gamma_{ab})(t - t')}, \quad (4.37)$$

where $\rho_{ab}(\omega_{ab}, \vec{r}, t_3^+) = \rho_{ab}(\omega_{ab}, \vec{r}, t_3^-)^*$. Using this condition in equation (4.37) we obtain:

$$\rho_{ab}(\omega_{ab}, \vec{r}, t) = \frac{id_{ab}}{2\hbar} e^{-\gamma_{ab}(t - t_1)} \left[\int_{-\infty}^{2t_2 - t_3} dt' \epsilon_{in}(\vec{r}, t') e^{-i\omega_{ab}(t_3 + t' - 2t_2)} \right.$$
$$\left. + 2\sinh\left(\frac{\alpha z}{2}\right) \int_{2t_2 - t_3}^{t_2} dt' \epsilon_{in}(0, t') e^{-i\omega_{ab}(t_3 + t' - 2t_2)} \right] e^{-i\omega_{ab}(t - t_3)}$$
$$- \frac{id_{ab}}{2\hbar} \int_t^{t_3} dt' \epsilon_{out}(\vec{r}, t') e^{(i\omega_{ab} - \gamma_{ab})(t - t')} \quad (4.38)$$

Again, the polarization needs to be calculated to analyze the response of the system. First, we look at the term related to the free evolution (first two terms of equation (4.38)):

$$P_1(\vec{r}, t) = \frac{id_{ab}^2}{2\hbar} e^{-\gamma_{ab}(t - t_1)} \left[\int_{-\infty}^{2t_2 - t_3} dt' \epsilon_{in}(\vec{r}, t') \int d\omega_{ab} G(\omega_{ab}) e^{-i\omega_{ab}(t_3 + t' - 2t_2)} e^{i\omega_{ab}(t - t_3)} + \right.$$
$$\left. 2\sinh\left(\frac{\alpha z}{2}\right) \int_{2t_2 - t_3}^{t_2} dt' \epsilon_{in}(0, t') \int d\omega_{ab} G(\omega_{ab}) e^{-i\omega_{ab}(t_3 + t' - 2t_2)} e^{i\omega_{ab}(t - t_3)} \right] \quad (4.39)$$

As in section 4.2, it is possible to calculate the polarization in the frequency domain:

$$P_1(\vec{r}, \omega) = \frac{id_{ab}^2 \pi}{\hbar} e^{-2\gamma_{ab}(t_3 - t_2 - t_1)} e^{-2i\omega(t_3 - t_2)} G(\omega_L) \left[\epsilon_{in}(\vec{r}, \omega) + \epsilon_{in}(0, \omega) 2\sinh\left(\frac{\alpha z}{2}\right) e^{\frac{1}{2}\alpha z} \right] \quad (4.40)$$

We now consider the second term of equation (4.38). Following the same steps as in section 4.2, we obtain:

$$P_2(\vec{r},\omega) = \frac{i\pi d_{ab}^2}{2\hbar}\epsilon_{out}(\vec{r},\omega)G(\omega_L) \tag{4.41}$$

Combining P_1 and P_2 gives the total polarization:

$$P(\vec{r},\omega) = -\frac{i\pi d_{ab}^2}{2\hbar}G(\omega_L)\left[\epsilon_{out}(\vec{r},\omega)\right.$$
$$\left. + 2e^{-2\gamma_{ab}(t_3-t_2-t_1)}e^{-2i\omega(t_3-t_2)}\left(\epsilon_{in}(\vec{r},\omega) + \epsilon_{in}(0,\omega)2\sinh\left(\frac{\alpha z}{2}\right)e^{\frac{1}{2}\alpha z}\right)\right] \tag{4.42}$$

Looking for a solution of the type $\epsilon_{out}(\vec{r},\omega) = A(z,\omega)e^{-ikz}$ and writing the field ϵ_{in} as something proportional to the signal just before the crystal (see equation (4.16)), the efficiency is given by:

$$\eta = \left|2\left[\sinh\left(\frac{\alpha z}{2}\right)\right]\right|^2, \tag{4.43}$$

where the decoherence is not included ($\gamma_{ab} = 0$). Additionally, the envelope of the output field is given by:

$$A(z,t) = -2A_{in}(0, 2t_3 - 2t_2 + t)e^{i\omega_L(2t_3-2t_2+t)}e^{-2\gamma_{ab}(t_3-t_2-t_1)}e^{-2i\omega(t_3-t_2)}\sinh\left(\frac{\alpha z}{2}\right) \tag{4.44}$$

Equation (4.44) shows that the echo will be released at $t_e = 2t_3 - 2t_2 + t_1$ because A_{in} is centered at $t = t_1$.

As in the case of the two-pulse photon echo protocol, the double inversion photon echo cannot be used as a quantum memory because the amplification is still present [75]. Although the final echo is emitted with the atoms in the ground state, the amplified echo after the first π-pulse affects the polarization of the medium. This effect can be understood by looking at the polarization as a function of the optical depth, before and after the first echo is released. In figure 4.9, it is possible to see in blue the polarization after the input pulse absorption and, in red, the polarization after the first echo is released (and before the second π-pulse is applied). The change in the polarization generated by the emission of the first echo affects the efficiency of the second echo.

It is remarkable that the efficiency of this protocol is the same than the one presented in the two-pulse photon echo protocol (equation (4.34)). This happens because the emission of the first echo transfers the coherences in such way that all the energy stored in the crystal can be released without being reabsorbed. This behavior is analogous to photon echo protocols where the echo is emitted in the backward direction. In that case, if the echo between the π-pulses is not emitted,

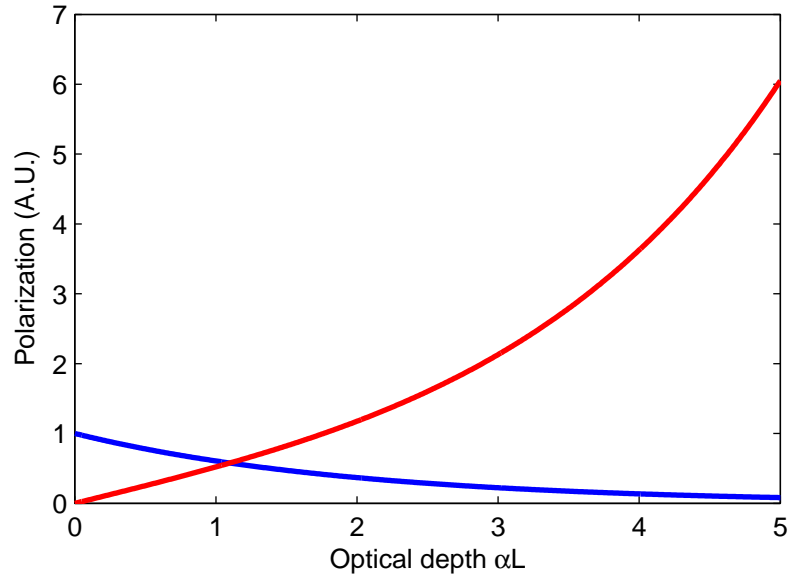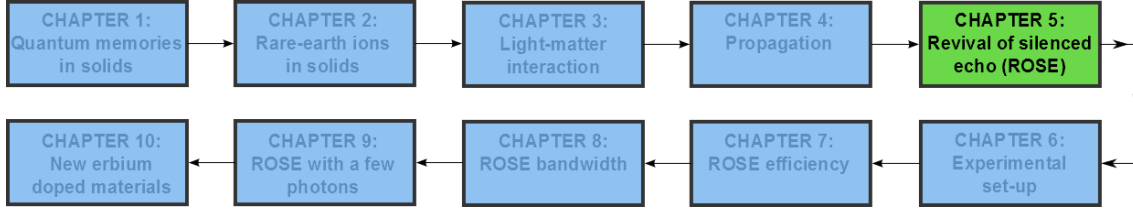all the energy can be released by the medium (i.e. 100% of storage efficiency) [76].

Figure 4.9: Polarization as a function of the absorption. In blue the polarization after the input is absorbed by the crystal and, in red, the polarization after the first echo emission.

Revival of Silenced Echo (ROSE)

In the former chapter, two protocols to store information directly derived from the two-pulse photon echo were presented. They cannot be envisaged as quantum memories because of the amplifying effect that the information suffers. If the echo is emitted in an inverted medium, the amplification cannot be avoided. In the case of the double inversion photon echo, although the echo is emitted with the ions in the ground state, the amplification is not avoided. This is related to the emission of the primary echo which modifies the distribution of the coherences. If it were possible to avoid the emission of the primary echo, the secondary echo should not suffer any amplification. The Revival of Silenced Echo (ROSE) photon echo protocol is based on this approach [24].

ROSE takes advantage of the phase matching condition between the beams (signal and rephasing pulses) to avoid the emission of the primary echo. In this chapter, I will introduce ROSE protocol which is based on the double inversion photon echo but that can be used for a quantum memory. I will present the ROSE protocol, the expected performances and compare it with other protocols that succeeded in storing information at telecom wavelength.

5.1 Phase matching condition

ROSE protocol relies on the phase matching condition to silence the first echo. In this section I will go back to the two-pulse photon echo sequence to show how to avoid the emission of its echo. To do this, I will consider the phase matching condition: the wave vector of the input pulse and the rephasing pulse do not have necessarily the same direction as depicted in figure 5.1.
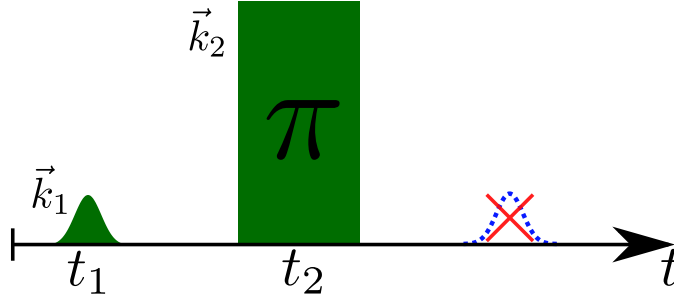
Figure 5.1: Two-pulse photon echo with phase matching condition. At t_1 a small area pulse with a wavevector $\vec{k}_1$ is sent to the medium and, at t_2, a π-pulse with wavevector $\vec{k}_1$
.

At $t = t_1$, a weak pulse (weak pulse) with a wavevector $\vec{k}_1$ is sent to the crystal. This pulse will be absorbed by the medium and the coherences will freely evolve following the first term of equation (3.22):

$$\tilde{\rho}_{ab}(\vec{r}, t) = \tilde{\rho}_{ba}(\vec{r}, t_1^+) e^{i\Delta(t-t_1)} \tag{5.1}$$

This can be rewritten in the non-rotating system:

$$\rho_{ab}(\vec{r}, t) = \tilde{\rho}_{ba}(\vec{r}, t_1^+) e^{i\Delta(t-t_1)} e^{i(\omega_L t - \vec{k}_1 \vec{r})} \tag{5.2}$$

In this case, the coherences are referenced to the first pulse. When applying a second pulse, the rotating frame should be changed taking into account that $\vec{k}_1$ is not necessary equal to $\vec{k}_2$ (π-pulse). At $t = t_2$, as in equation (4.19), the coherences are modified as follows:

$$\tilde{\rho}_{ab}(\omega_{ab}, \vec{r}, t_2^+) = \tilde{\rho}_{ba}(\omega_{ab}, \vec{r}, t_2^-) \tag{5.3}$$

In chapter 4.3 the calculation of this part only consisted of conjugating $\tilde{\rho}_{ab}$ after applying the π-pulse, here that is not sufficient. As the pulses have different wavevectors, the rotating frame is different. At $t = t_2^+$, the coherences in the rotating frame are given by:

$$\tilde{\rho}_{ab}(\vec{r}, t_2^+) = \tilde{\rho}_{ba}(\vec{r}, t_1^+) e^{-i(\Delta(t_2-t_1)+(\vec{k}_2-\vec{k}_1)\vec{r})} \tag{5.4}$$

For $t > t_2$, the system freely evolves:

$$\tilde{\rho}_{ab}(\vec{r}, t) = \tilde{\rho}_{ba}(\vec{r}, t_1^+) e^{-i(\Delta(t_2-t_1)+(\vec{k}_2-\vec{k}_1)\vec{r})} e^{-i\Delta(t-t_2)} \tag{5.5}$$

Finally, the coherences in the non rotating frame can be obtained by multiplying by $e^{i(\omega_L t - \vec{k}_2 \vec{r})}$:

$$\rho_{ab}(\vec{r}, t) = \tilde{\rho}_{ba}(\vec{r}, t_1^+) e^{-i(\Delta(2t_2-t_1-t)+(2\vec{k}_2-\vec{k}_1)\vec{r})} e^{i\omega_L t} \tag{5.6}$$

From this equation, we see that the polarization is associated with a wavevector $\vec{k}_e = 2\vec{k}_2 - \vec{k}_1$. Additionally, as it was demonstrated in section 3.3.4, the coherences are in phase again at $t_e = 2t_2 - t_1$. Up to now, I did not consider any particular direction for the wavevectors. To simplify the calculation I will now consider that both beams propagate along the z-axis. In order to obtain the efficiency, we have to modify the resolution of the Maxwell equation for the two-pulse photon echo (equation (4.31)) by adding the spatial phase that comes from equation (5.6):

$$\frac{\partial A(z,\omega)}{\partial z}e^{-ikz} = \frac{1}{2}\alpha \left[A(z,\omega)e^{-ikz} - 2A_{in}^*(z,\omega)e^{i\omega_L t}e^{-2\gamma_{ab}(t_2-t_1)}e^{-2i\omega_L t_2}e^{-i(2k_2-k_1)z} \right] \quad (5.7)$$

Making the change of variables $A(z,\omega) = B(z,\omega)e^{\frac{1}{2}\alpha z}$ and using that $A_{in}^*(z,\omega) = A_{in}^*(0,\omega)e^{-1/2\alpha z}$, the equation becomes:

$$\frac{\partial B(z,\omega)}{\partial z} = -2\alpha A_{in}^*(0,\omega)e^{-2\gamma_{ab}(t_2-t_1)}e^{-2i\omega_L t_2}e^{i\omega_L t}e^{-i(2k_2-k_1-k)z}e^{-\alpha z} \quad (5.8)$$

Which we can rewrite in the following way:

$$\frac{\partial A(z,\omega)}{\partial z} = C(\omega)e^{-i(2k_2-k_1-k)z}e^{-\alpha z} \quad (5.9)$$

If the phase matching condition is not satisfied

$$\frac{|2k_2 - k_1 - k|\mathrm{L}}{2} > \frac{\pi}{2} , \quad (5.10)$$

the first term $-i(2k_2 - k_1 - k)z$ of equation (5.9) varies rapidly respect to the second term $-\alpha z$. After integrating from $z = 0$ to $z = \mathrm{L}$, the intensity of the output field is zero. There is no echo.

Although the echo is not emitted, the coherences will continue evolving without any modification. It is important to notice that at $t = 2t_2 - t_1$ the dipoles are in phase again but there is no emission to avoid the violation of the phase matching condition. This phase matching condition is the ROSE protocol basis.

5.2   ROSE efficiency

The unsatisfied phase matching condition silence the echo of the two-pulse photon echo scheme. In order to obtain a rephasing of the coherences with the emission of the echo, a second π-pulse can be applied. In figure 5.2 a temporal scheme is presented. It is important to notice that after the second π-pulse is applied, the atoms are in the ground state, assuring that the second echo is not emitted in an
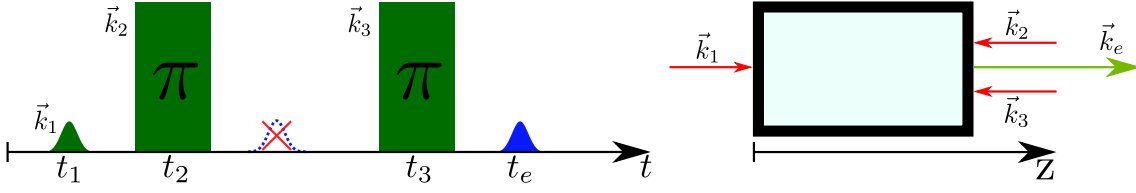
inverted medium.

Figure 5.2: Scheme of ROSE protocol. At t_1, a small pulse is sent to the medium, at t_2 the first π-pulse and, at t_3, the second π-pulse is applied. The π-pulses are counterpropagative with respect to the signal in order to avoid the emission of the echo in between the rephasing pulses.

We can now consider the phase matching of this echo. At $t = t_3$, as in equation (4.19), the coherences satisfy the following condition:

$$\widetilde{\rho}_{ab}(\omega_{ab}, \vec{r}, t_3^+) = \widetilde{\rho}_{ba}(\omega_{ab}, \vec{r}, t_3^-), \tag{5.11}$$

Or in the non rotating frame where the second pulse is taken as a reference:

$$\rho_{ab}(\omega_{ab}, \vec{r}, t_3^-) = \widetilde{\rho}_{ab}(\omega_{ab}, \vec{r}, t_3^-)e^{i(\omega_L(2t_2 - t_1) - (2k_2 - k_1)z)} \tag{5.12}$$

Using equation (5.11) it is possible to calculate the coherences after the π-pulse:

$$\rho_{ab}(\omega_{ab}, \vec{r}, t_2^+)e^{-i(\omega_L t_2 - \vec{k}_2\vec{r})} = \widetilde{\rho}_{ba}(\omega_{ab}, \vec{r}, t_1^-)e^{-i(\omega_L(2t_2 - t_1) - (2k_2 - k_1)z)}e^{i(\omega_L t_3 - k_3 z)}, \tag{5.13}$$

where the coherences are now referred to the third pulse. Rearranging the terms we obtain:

$$\rho_{ab}(\omega_{ab}, \vec{r}, t_3^+) = \widetilde{\rho}_{ba}(\omega_{ab}, \vec{r}, t_3^-)e^{i(\omega_L(2t_3 - 2t_2 + t_1) - (2k_3 - 2k_2 + k_1)z)} \tag{5.14}$$

As in the former section, we can calculate the phase matching condition, which is satisfied if:

$$\frac{|2(k_3 - k_2) + k_1 - k_e|\text{L}}{2} < \frac{\pi}{2} \tag{5.15}$$

The echo will be emitted if $k_e = 2(k_3 - k_2) + k_1$. As $k_3 = k_2$, the echo has the same wavevector of the input pulse $k_e = k_1$ and it will be emitted at $t_e = 2t_3 - 2t_2 + t_1$.

To calculate the efficiency of the echo it is possible to use the polarization from the double inversion photon echo (equation (4.42)). However, as there is no emission of the echo after the first π-pulse, we have to remove the term related to its emission:

$$P(\vec{r}, \omega) = -\frac{1}{2}\alpha\left[\epsilon_{out}(\vec{r}, \omega) + 2e^{-2\gamma_{ab}(t_3 - t_2 - t_1)}e^{-2i\omega(t_3 - t_2)}\epsilon_{in}(\vec{r}, \omega)\right] \tag{5.16}$$

Using this polarization as a source of the Maxwell equation (4.5), and integrating from 0 to L, it is possible to calculate the output field for the echo giving the efficiency of the protocol:

$$\eta = \left| (\alpha L)^2 e^{-\alpha L} e^{-\frac{4t_{23}}{T_2}} \right|, \tag{5.17}$$

where $t_{23} = t_3 - t_2$, $\gamma_{ab} = 1/T_2$ and where I considered that the input pulse is sent at $t_1 = 0$. In figure 5.3, the efficiency of the ROSE protocol as a function of the optical depth is shown. This function has a maximum at $\alpha L = 2$, where the efficiency is 54%. The recovered echo can have a maximum efficiency of 54% because of the beams configuration chosen here. As the echo is released in the forward direction, reabsorption of the echo occurs. Thus, not all the energy can leave the medium.
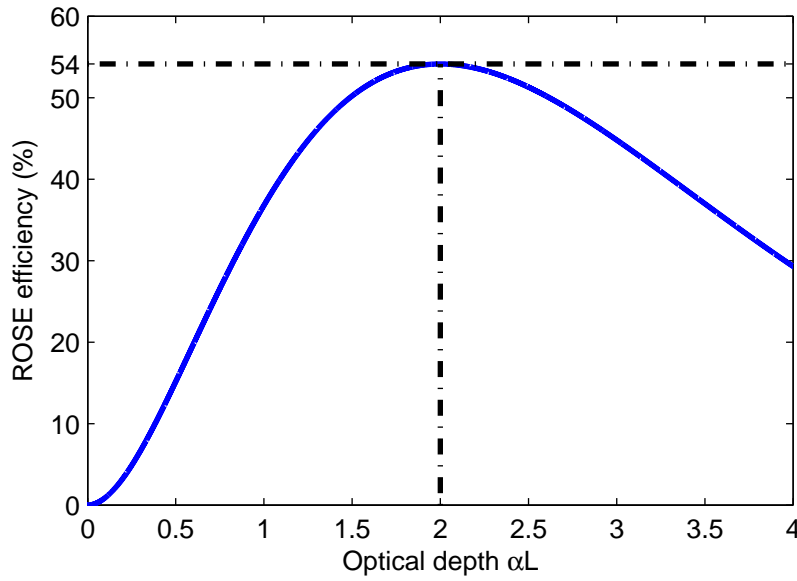
Figure 5.3: ROSE efficiency as a function of the optical depth αL.

However, as it was demonstrated by Sangouard and coworkers [76] in the case of CRIB protocol, a 100% efficiency can be obtained if the echo leaves the medium in the backward direction. This can be done by illuminating the medium from the side, with the rephasing pulses making an angle of $\pi/3$ [24].

Although it was not included in the former calculation, the performance of the protocol strongly depends on the quality of the π-pulses to invert the medium, as it will be explained in section 5.5. Imperfect π-pulses not only partially rephase the coherences but leave also the medium partially inverted. In the next section I will introduce the adiabatic rapid passages which produces the same result as π-pulses but are known to be more robust.

5.3   An extra ingredient: adiabatic rapid passages (ARP)

Adiabatic rapid passages (ARP) have been shown to be a more robust way to invert the population in a inhomogeneously broadened optically thick medium. The ARP technique was initially used in magnetic resonance to achieve population inversion of the spins [77]. A few years later, the same technique was applied in the optical regime to achieve population inversion on an optical transition [78].

ARP consist of chirped laser pulses that are swept through the resonance of a transition. In figure 5.4 an example of an ARP is shown. On the left the absorption profile and, on the right, the ARP frequency dependence. Provided the pulses satisfy the adiabatic condition, that we will consider later, these pulses will have a greater efficiency to invert the population than using regular π-pulses.

Although a better inversion is obtained while using chirped pulses, we also need to consider the evolution of the coherences as the main purpose of the rephasing pulses is to get a rephasing of the coherences. Chirped pulses excite the coherences in a different way than π-pulses. While these pulses excite all the atoms at the same instant, ARP pulses excite sequentially the atoms. In other words, they induce an extra dephasing that partially silence the first echo independently of the phase matching condition.

Nevertheless the second ARP compensates the dephasing induced by the first one as discussed in [79]. In that sense, a pair of ARP is equivalent to a pair of π-pulses rendering our calculation perfectly valid. This particularity is not the scope of the present discussion but this should be kept in mind when ARP pulses are used.
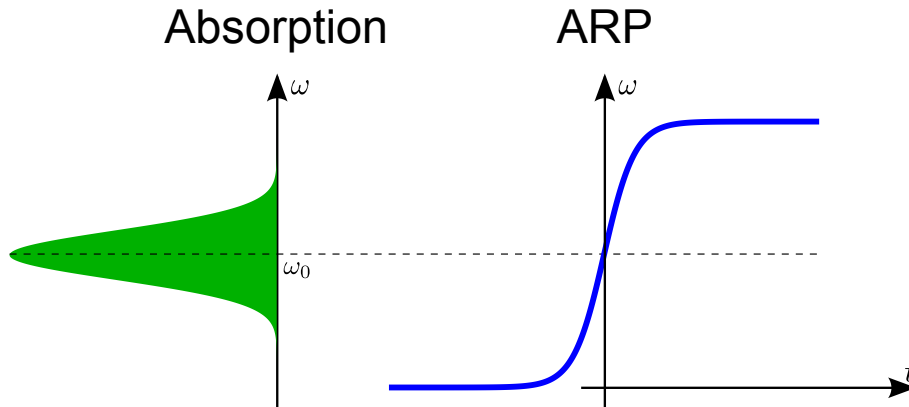

Figure 5.4: Frequency sweep of an adiabatic rapid passage with respect to the absorption profile. The laser is chirped across the resonance of the transition.

In equation (3.27), I have derived the optical Bloch equations for the Bloch vector $\vec{B} = (u, v, w)$. To graphically represent how adiabatic pulses work, I will

rewrite the Bloch vector dynamics in the following way:

$$\dot{\vec{B}} = \vec{D} \wedge \vec{B}, \tag{5.18}$$

where $\vec{D} = (-\Omega, 0, \Delta)$ is known as the driving vector (without decoherence). Equation (5.18) indicates that the vector $\vec{B}$ is precessing around the vector $\vec{D}$ at a frequency given by its module.

We now consider a linear chirp. The Bloch vector is said to adiabatically follow the driving vector if the Bloch vector $\vec{B}$ precesses at a much faster rate around the driving vector $\vec{D}$ compared to the tilting rate of the driving vector, which tilts because of the light field applied on the transition.

If the chirping rate is given by r, the adiabatic condition can be expressed in the following way:

$$\Omega^2 >> r, \tag{5.19}$$

In figure 5.5, a geometrical interpretation of the adiabatic following is presented.
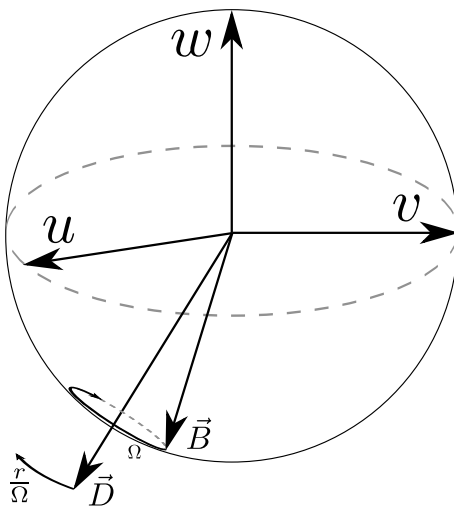
Figure 5.5: Geometrical representation of the Bloch vector $\vec{B}$ and the driving vector $\vec{D}$. The adiabatic condition is accomplished if the precession rate Ω of the Bloch vector around the driving vector is much faster than the tilting rate r/Ω of the driving vector.

It is also possible to generalize this equation to obtain the adiabatic condition for any detuning and for any type of chirped pulses. If we consider that the electric field is given by $E(t) = \varepsilon(t)e^{i\omega t + i\phi(t)}$, the adiabatic condition can be expressed as follows [80]:

$$\left| \frac{\dot{\Omega}(t)(\Delta - \dot{\phi}(t)) + \Omega(t)\ddot{\phi}(t)}{\left[\Omega(t)^2 + (\Delta - \dot{\phi}(t))^2 \right]^{3/2}} \right| < 1, \tag{5.20}$$

There are several types of pulses used to perform ARP. In the context of the ROSE protocol, the pulses used are known as complex hyperbolic secant (CHS). In the

following section I will introduce the CHS and specify the adiabatic condition for this kind of pulses.

5.3.1 Complex Hyperbolic secant (CHS)

A complex hyperbolic secant (CHS) is a chirped pulse that can be used to execute ARP. An analytical solution of the Bloch equations can be derived for CHS pulses, as shown by Silver and coworkers in 1985 [81]. The CHS pulses are defined, using a complex notation, as:

$$E(t) = E(t_0) \left[\text{sech}(\beta(t - t_0))\right]^{1-i\mu}, \tag{5.21}$$

where μ is a constant and $1/\beta$ the pulse duration. The time dependent Rabi frequency and the instantaneous frequency (shown in figure 5.6) are:

$$\Omega(t) = \Omega(t_0)\text{sech}(\beta(t - t_0)) \tag{5.22}$$

$$\omega(t) = \omega(t_0) + \mu\beta\text{tanh}(\beta(t - t_0)) \tag{5.23}$$

In order to use the CHS as ARP we have to satisfy the adiabatic condition.
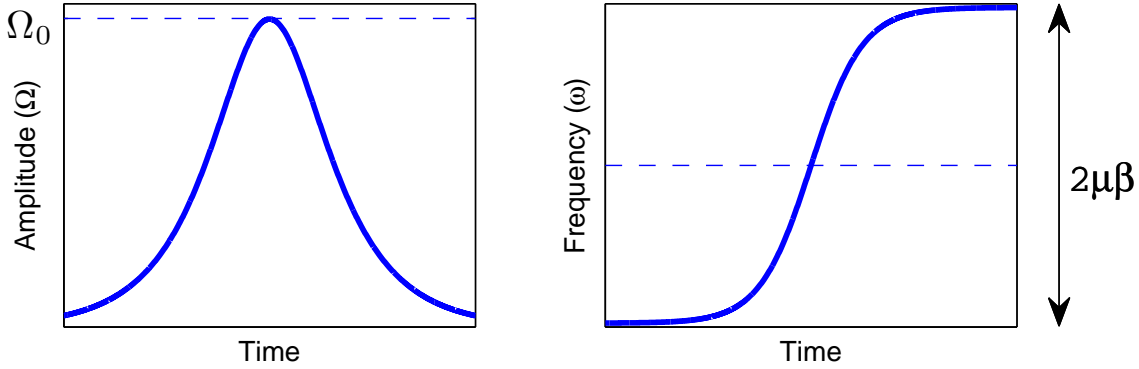
Figure 5.6: Amplitude (Ω) and instantaneous frequency (ω) as a function of time for a CHS pulse. Ω_0 is the Rabi frequency and $2\mu\beta$ the bandwidth.

Using equation (5.20) and the definition of the CHS, the adiabatic condition for CHS pulses is given by:

$$\left| \frac{\mu\Omega_0\beta^2 \cosh(\beta t)^2}{[\Omega_0^2 + \mu^2\beta^2 \sinh^2(\beta t)]^{3/2}} \right| < 1, \tag{5.24}$$

where I considered only atoms in resonance ($\Delta = 0$). The ratio is maximum at $t = 0$, where the adiabatic condition should be precisely satisfied for CHS, leading

to:

$$\mu\beta^2 < \Omega_0^2 \tag{5.25}$$

This inequality relates the chirp rate of the CHS with the Rabi frequency. As the chirp rate r is given by $r = d\omega/dt = \mu\beta^2$, equation (5.25) can be rewritten in the form of equation (5.19):

$$r < \Omega_0^2 \tag{5.26}$$

Therefore, the chirp rate of the CHS pulses is limited by the Rabi frequency.

In the following section, I compare the CHS pulses and the π-pulses regarding their transfer of energy to an optically absorbing medium.

5.3.2 CHS vs π-pulses

Chirped pulses have shown to be an efficient way to invert population in an absorbing material [82, 83]. This is related to the way they transfer energy to the medium. Compared to regular π-pulses, chirped pulses lose much less energy during their propagation.

In this section, I will present a simple energetic calculation to analyze the energy fraction transfered by CHS pulses and by π-pulses to an absorbing medium. This analysis was already performed by our group in the past [24, 70]. However, it is useful to illustrate the difference between CHS pulses and π-pulses, and why the CHS pulses can keep their properties during propagation. This makes them more robust for ROSE implementation.

For a π-pulse, the energy of the field over a cross sectional area A is given by:

$$W_\pi = \frac{Ac\epsilon_0\hbar^2\pi}{2d_{ab}^2}\Omega_0 \tag{5.27}$$

If we consider that the π-pulse inverts perfectly the medium, the energy of the atoms promoted to the excited state is given by:

$$W_{at} = \frac{Ac\epsilon_0\hbar^2}{\pi d_{ab}^2}\alpha L\Omega_0 \tag{5.28}$$

Therefore, the energy transfered by the π-pulses to the medium can be written as follows:

$$R_\pi = \frac{W_{at}}{W_\pi} = \frac{2}{\pi^2}\alpha L \tag{5.29}$$

As ROSE protocol reaches its maximum efficiency at $\alpha L = 2$, this ratio is close to 1. This means that most of the energy is transferred to the ions. On the other hand,

the energy of a CHS pulse is given by:

$$W_{CHS} = \frac{Ac\epsilon_0 \hbar^2}{2d_{ab}^2 \beta} \Omega_0^2 \tag{5.30}$$

And the energy of the atoms excited by the CHS pulse becomes:

$$W_{at} = 2\mu\beta ALN\hbar\omega_L \,, \tag{5.31}$$

Now the energy transferred to medium is given by:

$$R_{CHS} = \frac{W_{at}}{W_{CHS}} = \frac{2}{\pi^2} \frac{\mu\beta^2}{\Omega_0^2} \alpha L \tag{5.32}$$

R_{CHS} is proportional to the ratio between the chirp rate $(\mu\beta^2)$ and the Rabi frequency. If the adiabatic condition is accomplished for the ARP pulses (equation (5.25)), we can assure that:

$$R_{CHS} < 1 \,, \tag{5.33}$$

as $\mu\beta^2/\Omega_0^2 < 1$. Furthermore, the following relation between π-pulses and ARP pulses can be shown:

$$R_{CHS} < R_\pi \tag{5.34}$$

This means that the fraction of energy transferred by a CHS is smaller than the fraction of energy transferred by a π-pulse. Additionally, π-pulses have an energy which is quite similar to the energy of the atoms, while the energy of the CHS pulses is clearly greater due to the adiabatic condition, therefore:

$$W_{CHS} > W_\pi \approx W_{at} \tag{5.35}$$

Thus, the CHS pulses will pass through the medium with less distortion because they lose much less energy. Furthermore, regular π-pulses suffer from a technical limitation regarding their bandwidth. To increase the bandwidth of a π-pulse, the pulses must be shorten. Although, nowadays it is not difficult to achieve extremely short pulses, in order to keep constant the area of the pulse, we need to increase its amplitude. In the case of CHS, we can easily change the bandwidth by modifying the parameters μ and β with the only constraint given by the adiabatic condition.

5.4   Protocol bandwidth

As explained in section 1.2.4, the bandwidth of the protocol is an important performance of a memory protocol. In the case of CHS, the bandwidth, which I will call BW, is given by: $BW = 2\mu\beta$. Due to the adiabatic condition, the parameters μ and β cannot be independently modified. Equation (5.25) sets a limit to the chirp rate of the CHS pulses for a given laser power. Thus, the bandwidth of the protocol and the duration of the pulses $(1/\beta)$ are related.

To clarify the relation between the bandwidth and the pulse duration, we can rewrite the adiabatic condition (equation (5.25)) as:

$$BW \times \beta < 2\Omega_0^2 \tag{5.36}$$

To keep this relation constant when we increase the bandwidth BW, we have to decrease β. Or, in other words, to use longer pulses as its duration is proportional to $1/\beta$. Thus, in order to prevent an overlap between CHS, the time between CHS pulses (t_{23}) may need to be changed. In chapter 8, I discuss how t_{23} has to be modified to measure the efficiency of the protocol as a function of the bandwidth.

5.5   Imperfect inversion and rephasing

In the calculations presented until here, all the π-pulses (or CHS pulses) were considered to fully invert the medium and completely rephase the coherences. However, it is reasonable to question the effect of imperfect pulses on the efficiency. The imperfection of the pulses can be phenomenologically included in the efficiency modeling. To do so, we can analyze the Maxwell equation that gives place to the ROSE echo (equation (5.7)):

$$\frac{\partial A(z,\omega)}{\partial z} = -\frac{1}{2}\alpha A(z,\omega) + \alpha A_{in}^*(0,\omega)e^{-\frac{2t_{23}}{T_2}}e^{-\frac{\alpha z}{2}} \tag{5.37}$$

In equation (5.37), there are two terms on the right side. We can recall equation (3.22) to understand the meaning of each term. The first term, $1/2\alpha A(z,\omega)$, is related to the second term of equation (3.22), which contains n_{ab}, the population level. Up to now, we consider that the inversion made by the π-pulses is perfect (i.e. a π pulse brings all the atoms from the ground state to the excited state and vice versa).

On the other hand, the second term of equation (5.37) is related to the first term of equation (3.22). This terms gives place to the free evolution of the system, to the dephasing of the dipoles. We did not consider any imperfection in the dephasing

(or rephasing process).

In order to consider both, the imperfect return of the ions from the excited state to ground state and the imperfect rephasing of the dipoles, we can add two phenomenological terms η_{pop} and η_{phase} respectively to equation (5.37):

$$\frac{\partial A(z,\omega)}{\partial z} = -\eta_{\text{pop}}\frac{1}{2}\alpha A(z,\omega) + \eta_{\text{phase}}\alpha A_{in}^{*}(0,\omega)e^{-\frac{2t_{23}}{T_2}}e^{-\frac{\alpha z}{2}}, \qquad (5.38)$$

If we make a change of variables $A(z,\omega) = B(z,\omega)e^{-\eta_{\text{pop}}\frac{\alpha}{2}z}$, and integrate from $z=0$ to $z=$L, we obtain:

$$B(z,\omega) = \frac{4\eta_{\text{phase}}\alpha A_{in}^{*}(0,\omega)e^{-\frac{2t_{23}}{T_2}}}{(1-\eta_{\text{pop}})}e^{-\frac{\alpha L}{4}(1-\eta_{\text{pop}})}\sinh\left[-\frac{\alpha L}{4}(1-\eta_{\text{pop}})\right] \qquad (5.39)$$

This equation can be simplified assuming that $\alpha L(1-\eta_{\text{pop}})/4 << 1$, which leads to the following expression for the efficiency:

$$\eta \approx \eta_{\text{phase}}(\alpha L)^2 e^{-\alpha L\frac{1+\eta_{\text{pop}}}{2}}e^{-\frac{2t_{23}}{T_2}} \qquad (5.40)$$

In figure 5.7, we can see the effect of changing either η_{pop} or η_{phase}. If the inversion is not perfectly done ($\eta_{\text{pop}} \neq 1$), we should not only expect a decrease in the efficiency but, also, a change in the position of the maximum. While if the imperfection comes from the rephasing process ($\eta_{\text{phase}} \neq 1$), the efficiency is reduced.
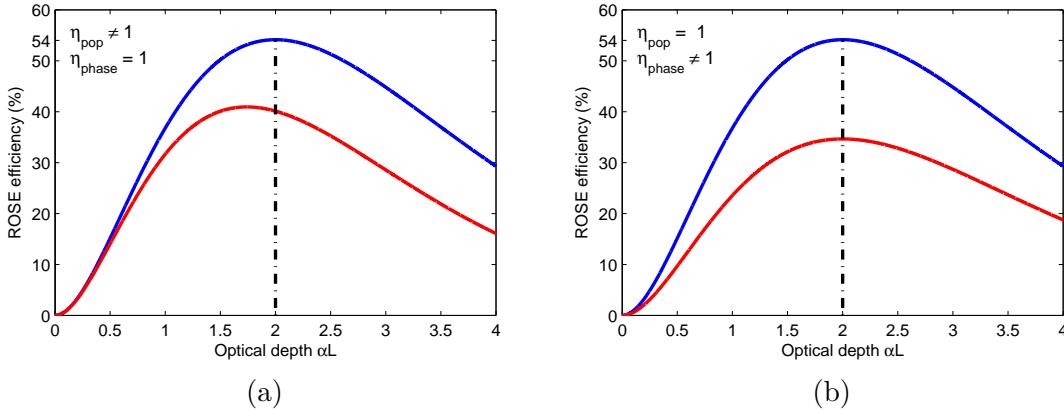
Figure 5.7: ROSE efficiency as a function of the optical depth αL. In blue the efficiency without taking any imperfections. The red curve represents the efficiency taking into account in (a) an imperfect inversion ($\eta_{\text{pop}} \neq 1$) and, in (b), an imperfect rephasing ($\eta_{\text{phase}} \neq 1$).

In section 7.2 I will present ROSE efficiency for different optical depths and, also, how the imperfect inversion of the medium modifies the efficiency.

5.6 Advantages and disadvantages against other protocols

As discussed in section 1.3, there are two protocols that succeeded in storing information at the single photon level in the telecom wavelength range. One of those protocols is given by the atomic frequency comb (AFC). Although AFC has succeeded in storing information at different wavelengths, it remains still quite inefficient at telecom wavelength. First of all, it is important to point out that using AFC requires a third spin ground state level to be able to perform an on-demand memory. Additionally, a good branching between optical and spin levels; and a long lifetime of the spin level are desirable. Er^{3+}:Y_2SiO_5 does not accomplish any of this condition, limiting the perspectives of this protocol. However, it remains as a material limitation and not as a theoretical limitation of the protocol. Furthermore, efficient optical pumping from one ground state to another is required to prepare the comb. In the case of erbium doped materials, this is quite inefficient. Although it has been shown that this process can be performed by optical pumping via an excited state[18], the long lifetime of the excited state limits the pumping efficiency in such way that the optical depth of comb is reduced, limiting the efficiency of the protocol.

The other protocol discussed in section 1.3.2, is called controlled reversible inhomogeneous broadening (CRIB). This protocol has also achieved good efficiencies at several wavelengths. However, it is still inefficient at telecom wavelength. To perform CRIB protocol, optical pumping is needed to create a narrow absorption linewidth within the inhomogeneous linewidth of the transition. CRIB suffers the same limitations as the AFC protocol in terms of optical pumping (i.e. transfer to the other ground state via the excited state), reducing the initial absorption. An important limitation of this protocol is also its storage bandwidth. To increase the bandwidth it is necessary to increase the initial broadening. When the broadening is increased the optical depth diminishes. As the efficiency depends on the absorption of the system, there is a trade off between the bandwidth and the efficiency of the protocol.

ROSE protocol does not have any complex preparation to program the material to store the information. While AFC and CRIB protocols require another ground state to prepare the system, ROSE protocol does not need any other ground state. Furthermore, ROSE protocol does not need to transfer the coherences to a long lifetime spin level to be on demand, as it is the case for the AFC. ROSE is set up to be an on-demand memory protocol that only requires a minimum of two levels. However, longer storage times could be achieved if an additional spin level were used

to transfer the coherences. In the case of erbium, this transfer is rather complicated because of the poor branching between the optical and spin levels. Furthermore, the coherence time of the optical levels in erbium is already quite high. ROSE protocol has a potential large bandwidth given by the inhomogeneous linewidth of the material. A high bandwidth may partially compensate a limited storage time depending on the application.

ROSE protocol is based on using strong pulses to rephase the coherences and, as they are applied in the same optical transition where the information is stored. Filtering the noise coming from the rephasing pulses is technically challenging. Furthermore, imperfections in the double inversion of the medium leads to spontaneous emission that fundamentally limits the signal to noise ratio. However, this appears as a technical limitation and not a fundamental one.

Experimental set-up
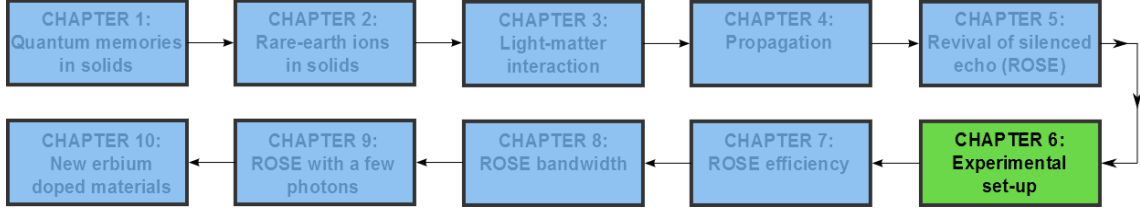
In the former section I introduced the protocol we use to store information: Revival of Silenced Echo (ROSE). In this chapter I will describe the optical set-up used to implement the ROSE protocol. Additionally, I will present a series of measurements, such as absorption profiles, coherence time and population lifetime, which characterize our sample.

6.1 Material

The experiments were performed using a Y_2SiO_5 crystal doped with erbium. As shown in chapter 2, this material has an optical transition at telecom wavelength and large coherence times on this transition. That justifies our choice.

The experiments were done in a 3 x 4 x 5 mm^3 Er^{3+}:Y_2SiO_5 crystal growth by Scientific Materials (from Bozeman, Montana, USA). The dopant concentration was 50 ppm (0.005%). As explained in section 2.1, Er^{3+}:Y_2SiO_5 is a birefringent crystal with 3 mutually perpendicular exctinction axes named D_1, D_2 and b.
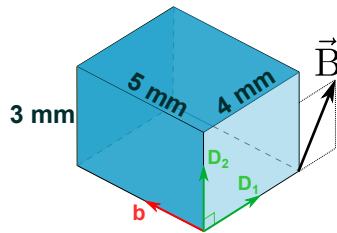
Figure 6.1: Orientation of an Er^{3+}:Y_2SiO_5 crystal respect to the external magnetic field $\vec{B}$, which is always kept in the plane D_1-D_2.

As presented in figure 2.4, the external magnetic field should be applied in the plane D_1-D_2 to keep the sites equivalent, maximizing the optical depth. Additionally, as explained in section 2.3, the largest g-factor is obtained by applying the magnetic

field in that direction, giving the longest coherence times. Thus, the crystal was set as shown in figure 6.1.

The crystal was cooled down in a variable temperature liquid helium cryostat, which was set, in most of the measurements, at 1.8 K. This temperature allows us to have good coherence times.

6.2 Optical Set-up

To implement ROSE protocol, we need two beams, the signal to be stored and the rephasing beam. The rephasing beam is used to apply the CHS pulses or the π-pulses. To accomplish the phase matching condition showed in section 5.1, a counterpropagative scheme between the beams was used. It is important to recall that the emission of the echo will have the same wavevector than the one for the signal one.

In figure 6.2 a sketch of the optical set-up, with the two beams, is presented. The laser source used in the experiments is a Koheras Adjustik commercial erbium-doped fiber laser with a wavelength centered at 1536.5 nm. The output of the laser was split into two beams using a fiber beam splitter. In order to apply the rephasing pulses, one of the output of the beam splitter injects a commercial fiber amplifier (Keopsys (ex- Manlight)) with a maximum output power of 20 dB.

The other output of the beam splitter, the weak signal, was sent to an acousto-optic modulator (AOM_1) and the strong beam (output of the amplifier) to another acousto-optic modulator (AOM_2), to shape them in time and frequency. Both AOM were controlled with an arbitrary wave generator AWG520 (Tektronix). After the AOM, both beams are guided in free space to the crystal. Two telescopes were used to change the waists of the beams. Additionally, quarter-wave plates and half-wave plates were used before the polarized beam splitters (PBS) to control the polarization of the beams after the fibers. Finally, the beams were focused in the crystal using plan-convex lenses. The waists of the beams in the crystal were $\omega = 52$ μm and $\omega = 115$ μm for the weak signal and the strong pulses respectively. In the following section, I will discuss more precisely the beam configuration in the crystal.

6.3 Beams configuration

As the rephasing pulses are much stronger than the signal, isolating the echo is a challenging task. To do this, first the cryostat was rotated to get rid of the reflections of the strong beam on the cryostat windows.
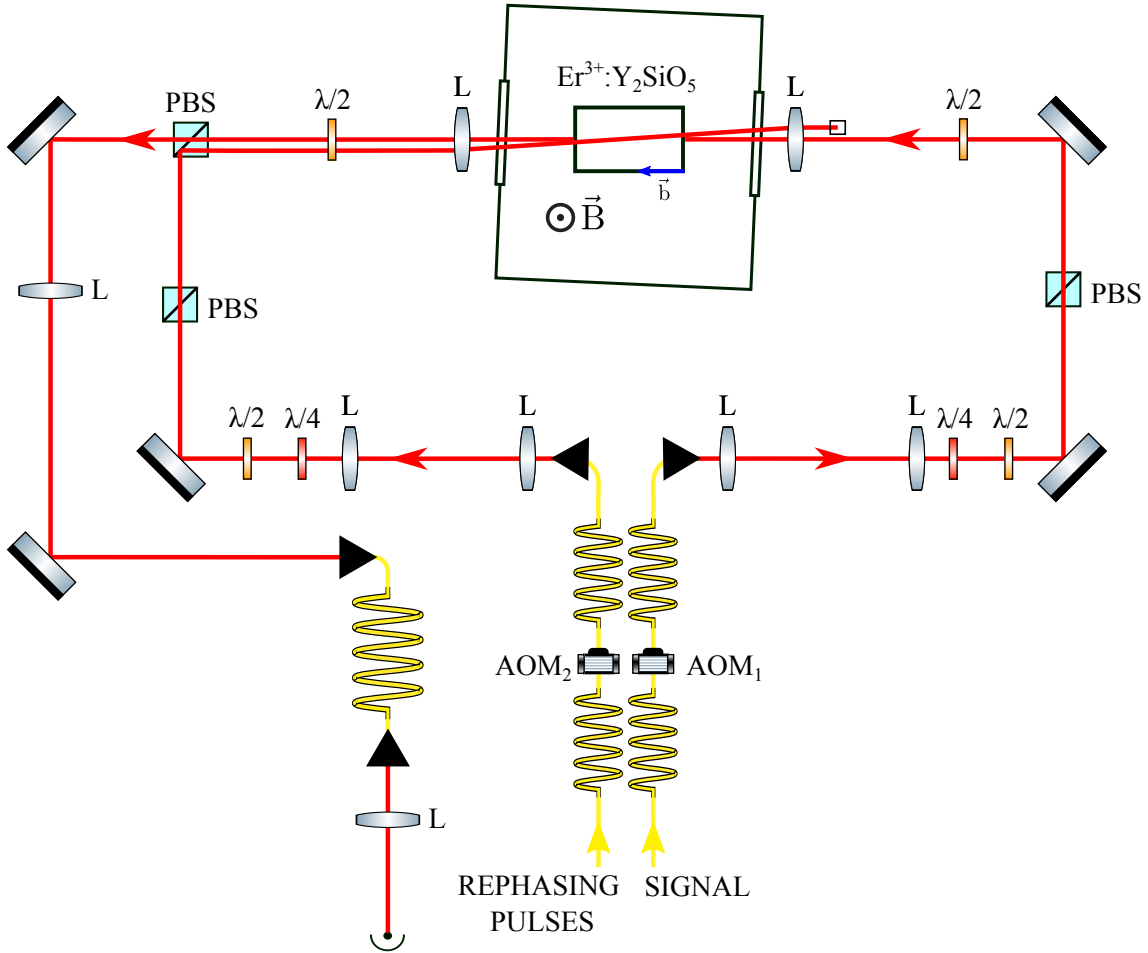
Figure 6.2: Set-up for the ROSE protocol. The weak pulse (signal) and the strong pulses (rephasing pulses) are almost counterpropagating to verify the appropriate phase matching condition. The small angle between the beams reduce the contamination of the echo by strong pulses or their specular reflections. The signal is polarized along D_2 while the rephasing pulses along D_1.

Additionally, the beams were cross-polarized, using the extinction axis with the highest absorption (D_2) for the signal and the one with the lowest absorption (D_1, which has approximately half the absorption of the axis D_2) for the strong pulses. Lastly, a small angle of a few milliradians between the signal and the strong pulses is adjusted without modifying the phase matching condition. The rephasing beams were directed to the crystal using a polarizing beam splitter (PBS). Because of the cross-polarized configuration of the beams, the signal is fully transmitted by the PBS. After the PBS, the transmitted signal is collected in a single-mode fiber, which acts as a spatial filter. Finally, the beam is coupled to free space again and focused in an avalanche photodetector APD110C/M (Thorlabs).

The orientation of the beams and their polarization are crucial because of the characteristics of the crystal. In figure 6.3, the beams configuration for a given angle of the magnetic field is presented summarizing the different choices.
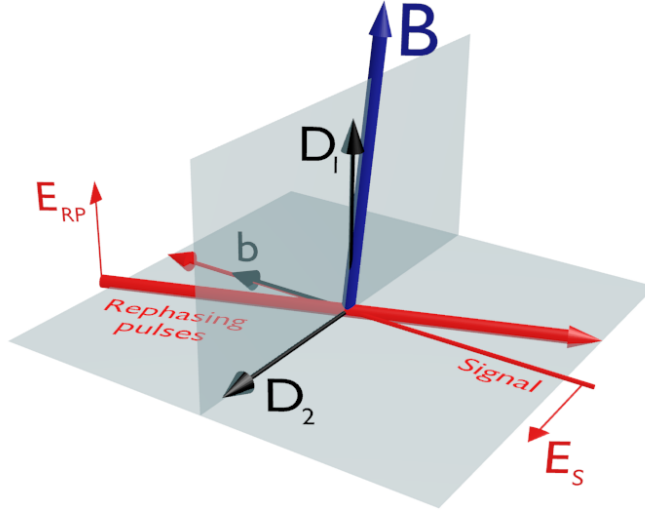
Figure 6.3: Sketch of the beams configuration (signal and rephasing pulses) their polarization (noted E_{RP} and E_S respectively) and the magnetic field $\vec{B}$ for a certain angle. D_1, D_2 and b are the Y_2SiO_5 optical extinction axes.

The external magnetic field was always placed perpendicularly with respect to the axis b to avoid the splitting of the magnetic sites and, also, to lengthen the coherence time. Furthermore, as presented in figure 6.3, the beams are cross polarized to be able to isolate the rephasing pulses reflections from the echo measurements.

       The focusing of the beams in the crystal is also crucial to run ROSE protocol. Concerning the beams sizes, we need to assure that all the ions excited by the signal beam "feel" a uniform field for the rephasing pulses. This implies that the rephasing pulses cover a larger excitation volume than the signal. In this experiment both beams were focused in the crystal using lenses with a focal length (f) of 15 cm. Prior focusing, their sizes are adjusted by the telescopes shown in figure 6.2. In figure 6.4 a diagram of the beams is presented.
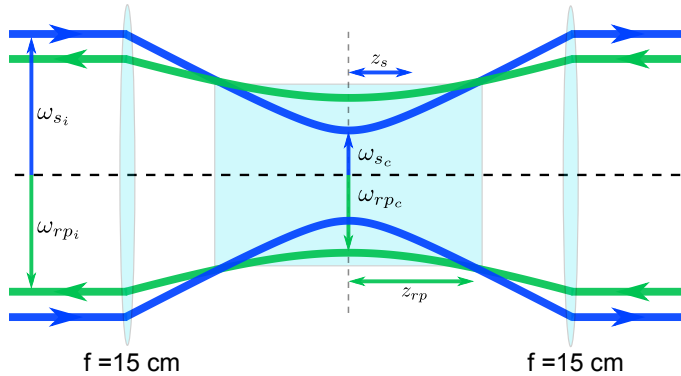

Figure 6.4: Beam diagram for the rephasing pulses (green) and the signal (blue). Both beams were focused in the crystal using lenses with a focal length f = 15 cm.

The waists were measured before focusing ω_i, the waist ω_f after focusing with a

focal length f can be computed using the following relation:

$$\omega_f = \frac{\lambda f}{\pi \omega_i} \tag{6.1}$$

In our case, the measured waists are $\omega_{s_i} = 1.42$ mm and $\omega_{rp_i} = 0.64$ mm. In order to assure the homogeneity of the rephasing pulses beams with respect to the signal field, we decided to take $\omega_{rp_c} \approx 2 \times \omega_{s_c}$. Using lenses with a focal length of 15 cm, the waists of the beams in the crystal were given by $\omega_{s_c} = 52$ μm and $\omega_{rp_c} = 115$ μm. We also have to consider the Rayleigh lengths longer than the crystal. The Rayleigh length z, for a given waist ω, is defined as follows:

$$z = \frac{\pi \omega^2}{\lambda} \tag{6.2}$$

From the waists we have the Rayleigh lengths $z_s = 5.5$ mm and $z_{rp} = 27.0$ mm. With this condition we are sure that the field "felt" by the atoms excited by the signal beam is uniform.

6.4   Inhomogeneous linewidth

As it was explained in section 2.5, when rare earth ions are placed into a host matrix they show an inhomogeneous broadening. In order to characterize the crystal, the inhomogeneous broadening was measured.

To measure the inhomogeneous linewidth we need to scan the frequency. This was done using a home-made laser (an external cavity diode laser) with an intra-cavity electro-optic modulator (EOM). Applying a high voltage to the EOM, we were able to sweep a few GHz. A Fabry-Perot interferometer is used to monitor the sweep and verify the absence of mode hops.

In figure 6.5, 6.6(a), 6.6(b) the absorption profile is presented for 0 T, 2 T and 2.7 T respectively. To calculate the inhomogeneous linewidth, the profiles were fitted with a Lorentzian function that are shown in red. From the fitting we obtain the inhomogeneous linewidth of 365 MHz at 0 T, 346 MHz at 2 T and 416 MHz at 2.7 T.

These measurements are also useful to estimate the maximum optical depth. From these measurements it is possible to see that the maximum is around $\alpha L = 3$. The change of the inhomogeneous linewidth when increasing the magnetic field is probably due to inhomogeneities of the magnetic field or due to the inequivalency among magnetic sites.
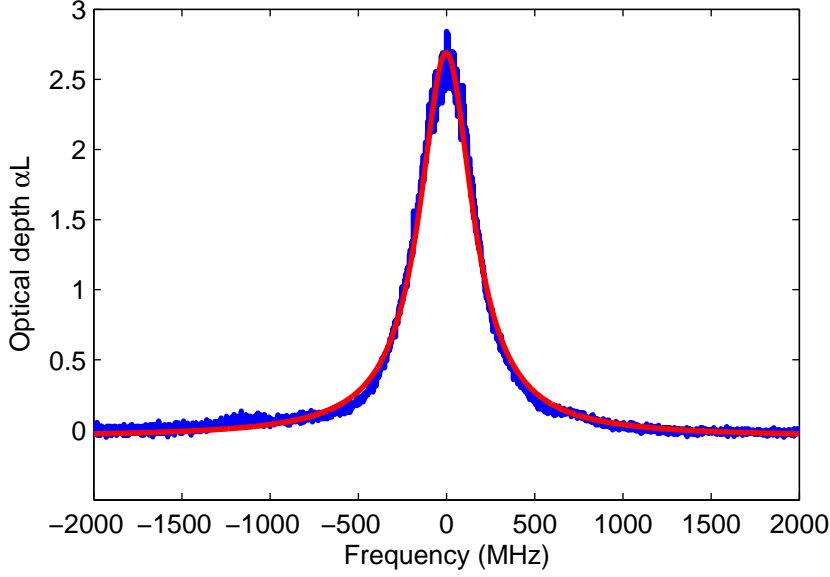
Figure 6.5: Absorption profile for Er^{3+}:Y_2SiO_5 without magnetic field. The measurement in blue and, in red, a Lorentzian fitting with a linewidth of $\Gamma_{inh} = 365$ MHz.

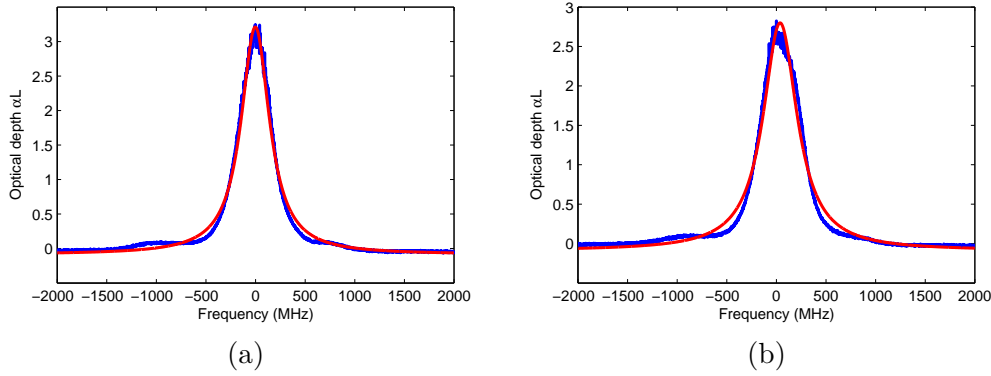**Figure 6.6:** Absorption profile for Er^{3+}:Y_2SiO_5 at 2 T in (a) and at 2.7 T in (b). The measurement in blue and, in red, a Lorentzian fitting with a linewidth of $\Gamma_{inh} = 346$ MHz for 2 T and $\Gamma_{inh} = 416$ MHz at 2.7 T.

This inequivalency appears because, although the crystal was placed with the axis b perpendicularly to the magnetic field, a small angle between them partially lifts the magnetic sites inequivalency, as explained in section 2.1.

In figure 6.7, another measurement of the inhomogeneous linewidth for a magnetic field of 2 T is presented. We can clearly see two peaks, each one corresponding to different magnetic sites. This effect strongly depends on the attachement of the crystal on its mount and its positioning in the cryostat.

The splitting of the sites does not have any effect on coherent experiments (i.e. two-pulse photon echo, ROSE, or other coherent protocols), but it reduces the absorption of the system.
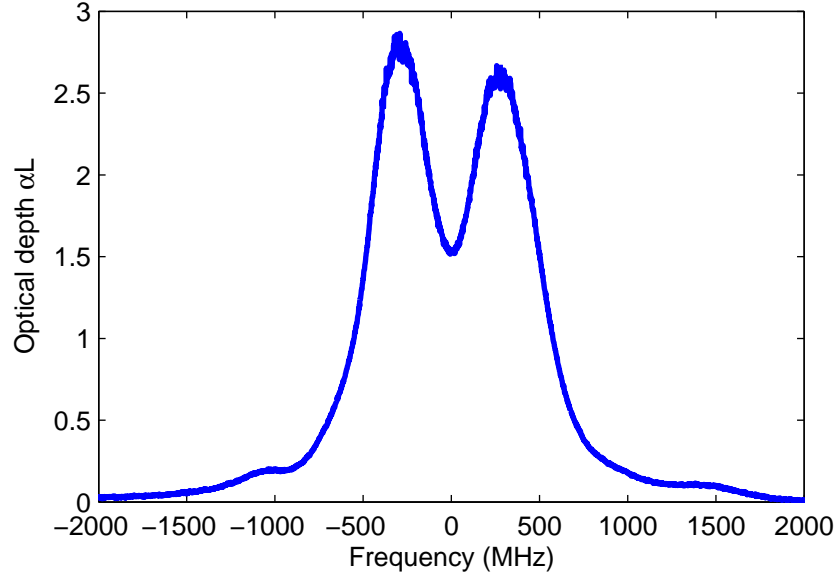
Figure 6.7: Absorption profile at 2 T. Each peak represents a different magnetic site.

For a 50 ppm crystal this is not problematic because the optical depth is still significant but for lower concentration crystals it might be critical.

6.5   Rabi frequency

The Rabi frequency constraints the adiabatic condition given by equation (5.25). In this section I will first describe the so-called optical nutation experiment that allows us to measure the Rabi frequency. Then, I will present the experimental measurement in our sample.

Optical nutation occurs when a strong monochromatic square pulse is sent through the medium [84]. Rabi oscillations can directly be observed on its transmission. The temporal shape of transmission curve can be understood from the Bloch vector equations (equations (3.30)) when the inhomogeneous broadening and the Gaussian profile of the beam are considered.

In order to understand this effect let's assume that there is no damping in the system (i.e. $\gamma_{bb} = 0$ and $\gamma_{ab} = 0$) and that a steady field is applied. In that case the optical Bloch equations are given by:

$$\begin{cases} \dot{u}(t) = -\Delta v(t) \\ \dot{v}(t) = \Delta u(t) + \Omega w(t) \\ \dot{w}(t) = \Omega v(t) \end{cases} \tag{6.3}$$

As shown in section 5.3, this equation can be thought as vector $\vec{B}$ precessing around the driving vector $\vec{D}$:

$$\dot{\vec{B}} = \vec{D} \wedge \vec{B} , \tag{6.4}$$

where $\left|\vec{D}\right| = \Omega_g = \sqrt{\Omega^2 + \Delta^2}$ is known as the generalized Rabi frequency. Let's suppose that at $t = 0$ all the atoms are in the ground state, thus, $u(0) = 0$, $v(0) = 0$ and $w(0) = -1$. And, at that time, a square pulse is applied. The Bloch vector will rotate at a frequency given by Ω_g. Therefore, it is natural to look for a solution for u,v and w of the form:

$$C_1 \cos(\Omega_g t) + C_2 \sin(\Omega_g t) + C_3 \tag{6.5}$$

Using the initial conditions ($u(0) = 0$, $v(0) = 0$ and $w(0) = -1$), the Bloch vector will be given by:

$$\begin{cases} u(t) = \frac{\Delta\Omega}{\Omega_g^2} \left(1 - \cos(\Omega_g t)\right) \\ v(t) = \frac{\Omega}{\Omega_g^2} \sin(\Omega_g t) \\ w(t) = -\frac{\Delta^2 + \Omega^2 \cos(\Omega_g t)}{\Omega_g^2} \end{cases} \tag{6.6}$$

Although this way to proceed is straightforward, the solution can be also unwrapped using rotation matrices because of the relation shown in equation (6.4). The radiated field is given by the polarization. Using equation (3.26) to write the polarization and making the assumption that the inhomogeneous profile is constant over the bandwidth of interest, we obtain the following:

$$P(t) = d_{ab} G(\omega_{ab}) \int_{-\infty}^{+\infty} \left(\frac{\Delta\Omega}{\sqrt{\Omega^2 + \Delta^2}} \left(1 - \cos(\sqrt{\Omega^2 + \Delta^2} t)\right) + i \frac{\Omega}{\sqrt{\Omega^2 + \Delta^2}} \sin(\sqrt{\Omega^2 + \Delta^2} t) \right) d\Delta , \tag{6.7}$$

where the term $e^{i\omega_L t}$ from equation (3.26) has not been included as $\omega_L \gg \sqrt{\Omega^2 + \Delta^2}$. The first integral, the one which contains u, is zero because the function is odd. Finally, the polarization will be given by:

$$P(t) = d_{ab} G(\omega_{ab}) \int_0^\infty \frac{\Omega}{\sqrt{\Omega^2 + \Delta^2}} \sin(\sqrt{\Omega^2 + \Delta^2} t) d\Delta \tag{6.8}$$

This equation can be rewritten using a Bessel function of the first kind because of the Mehler's Bessel function formula:

$$J_0(\Omega t) = \frac{2}{\pi} \int_0^\infty \frac{\sin(\sqrt{\Omega^2 + \Delta^2} t)}{\sqrt{\Omega^2 + \Delta^2}} d\Delta \tag{6.9}$$

Finally, the polarization is:

$$P(t) = d_{ab}G(\omega_{ab})\Omega\frac{2}{\pi}J_0(\Omega t) \tag{6.10}$$

If we look at the polarization as a function of the time, we see a damped oscillation. However, we need to go a step further and include the transverse Gaussian profile of the beam. We can consider the radiated intensity:

$$I(t) \propto \Omega E J_0(\Omega t), \tag{6.11}$$

where E is the input field. For a Gaussian beam profile, the total power will be given by:

$$W(t) \propto \int_0^\infty e^{-\frac{r^2}{\omega^2}} J_0(\Omega_0 e^{-\frac{r^2}{2\omega^2}} t)2\pi r dr \tag{6.12}$$

This equation can be solved by making a change of variables and using an identity for the Bessel integrals. The total radiated power is:

$$W(t) \propto \frac{J_1(\Omega t)}{\Omega t} \tag{6.13}$$

Optical nutation gives us a method to measure the Rabi frequency. In the figure 6.8, the intensity as a function of time is shown.
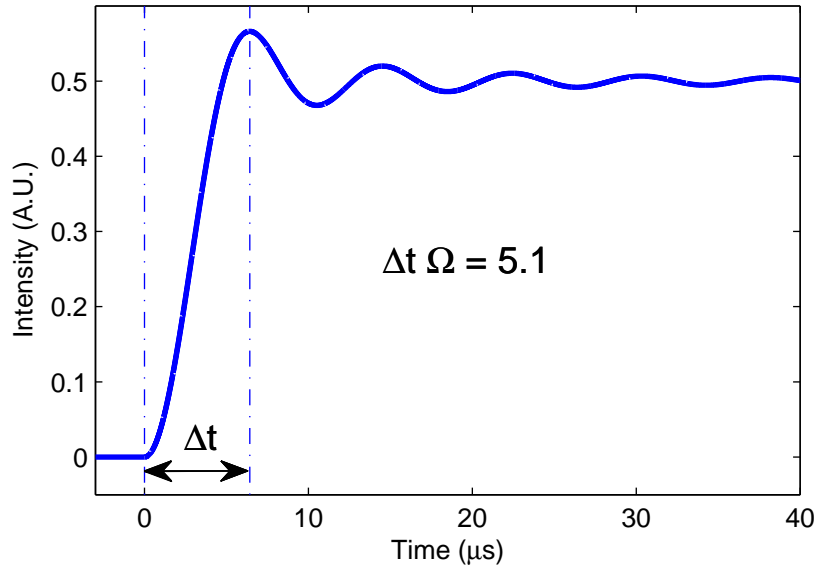

Figure 6.8: Polarization as a function of time while a field with constant amplitude is applied.

As the first maximum of the function is located at $\Omega\Delta t = 5.1$, we can easily estimate

the Rabi frequency from the nutation:

$$\Omega = \frac{5.1}{\Delta t}, \tag{6.14}$$

In figure 6.9, the nutation for the rephasing beam (polarized along D_1) is shown. This experiment is performed by sending a monochromatic light pulse, which brings the ions forth and back from the ground state to the excited state. Using equation (6.14), we obtain for the figure 6.9 a Rabi frequency of $\Omega_0 \approx 2\pi \times 800$ kHz.
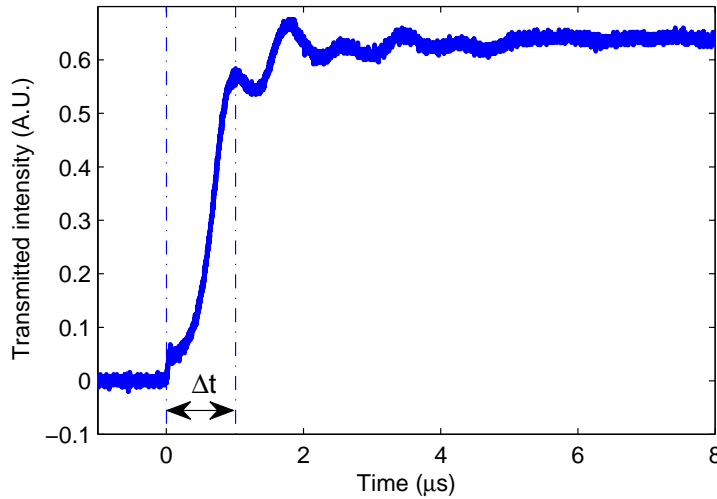

Figure 6.9: Nutation curve for rephasing beam. The Rabi frequency is given by $\Omega_0 \approx 2\pi \times 800$ kHz.

The curve does not really look like a Bessel function. This discrepancy is not fully understood but may be due to the interference between the electric and magnetic dipole transitions (both "allowed" in Er^{3+}).

6.6   Absorption

The optical depth scales ROSE efficiency. The optical depth was measured using the spectral hole-burning technique (SHB). In this section I will describe SHB technique and present a measurement.

Up to now, I have only considered coherent processes, where the evolution of the non diagonal terms of the density matrix (or u and v from the Bloch vector) were the protagonist. However, there are incoherent phenomenas, such as saturation, which are useful to characterize an atomic system.

Incoherent processes occur over time scales much longer than the coherence time T_2. As a consequence, equations (3.27) can be solved by considering u and v

in their steady states ($\dot{u} = 0$ and $\dot{v} = 0$):

$$\begin{cases} 0 = -\Delta v(t) - \frac{u(t)}{T_2} \\ 0 = \Delta u(t) - \frac{v(t)}{T_2} + \Omega w(t) \\ \dot{w} = -\frac{1}{T_1}(w(t) + 1) - \Omega v(t) \end{cases} \tag{6.15}$$

Solving the system of equation we can see how the population will vary as a function of the detuning Δ for a constant input field:

$$w = -\frac{1}{1 + \left(\frac{\Omega^2 T_1 T_2}{1 + (\Delta T_2)^2} \right)} \tag{6.16}$$

From this equation we can define a dimensionless saturation parameter S= $\Omega^2 T_1 T_2$ to analyze the behavior of the atomic population.
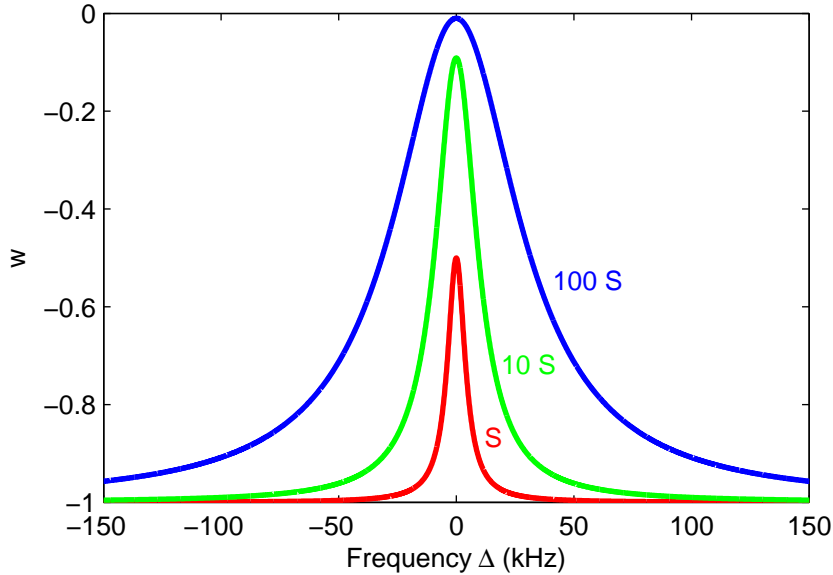
Figure 6.10:   Difference of population (w) as a function of the detuning. Each color corresponds to a different value of S.

In figure 6.10, w is showed as a function of Δ for different values of S for a coherence time $T_2 = 100\,\mu$s. Increasing the value of S (i.e. increasing the field) leads to a population w closer to zero. If we now consider that our material is inhomogeneously broadened, we will see a hole in its profile. The SHB technique allows us to measure the optical depth of the transition. Additionally, the width of the hole is proportional to the homogeneous linewidth.

To evaluate the optical depth of the transition we proceed in the following way:

- a monochromatic square pulse, with a duration much longer than T_2, saturates the transition. This is the burning process. The duration of the pulse in our experiments is 1 ms.

- a reading pulse, which consists of a weak pulse swept across the hole is applied. This chirped pulse has a central frequency equal to the frequency of the burning pulse. The chirp has a duration of 200 μs and sweeps 10 MHz.

In figure 6.11 the chirped pulse is shown. In red the transmission without the burning pulse and in blue the chirp when the burning pulse is applied. From this
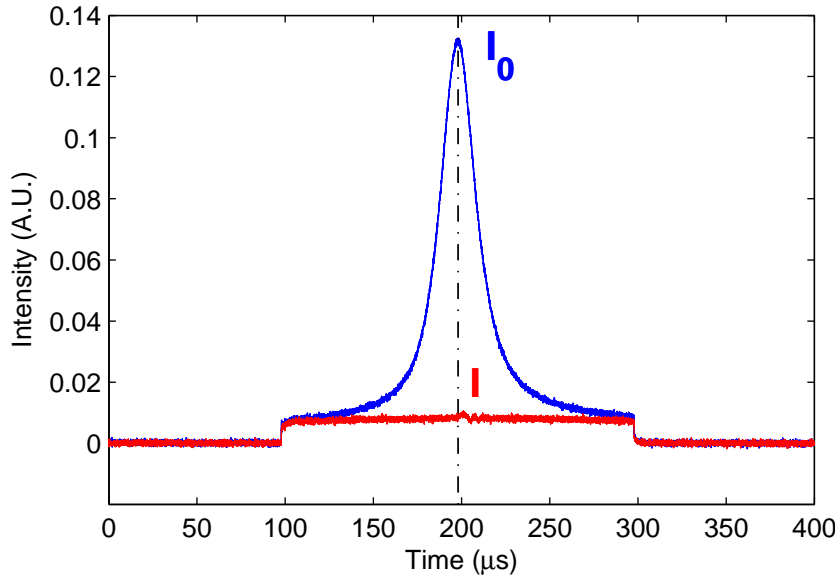

Figure 6.11: Hole burning spectrum. In blue, the chirp with the burning pulse and, in red, the chirp without the burning pulse. The chirp has a duration of 200 μs and sweeps 10 MHz.

measurement, it is possible to calculate the αL as the reading pulse is given by:

$$\mathrm{I} = \mathrm{I}_0 e^{\alpha \mathrm{L} w} \, , \tag{6.17}$$

where w is given by equation (6.16). The red curve from figure 6.11 represents the reading pulse absorbed by the media with $w = -1$ (all the ions in the ground state), while the blue curve is the input pulse absorbed according to (6.17) with w given by equation (6.16). If the burning pulse is strong enough, the population at the center of the reading pulse is given by $w = 0$. Thus, using the height of the blue peak and the value of the intensity for the red chirp, at the same time, the absorption is αL=-ln(I/I$_0$). Using this technique we were able to measure a range of αL from 0 to 3.9 for a Y$_2$SiO$_5$ crystal doped with 50 ppm of erbium, consistent with the absorption profiles presented in section 6.4.

6.7   Population lifetime (T_1) and coherence time (T_2)

The coherence time (T_2) was measured for different magnetic fields and temperatures. The orientation of the magnetic field with respect to the axes of the crystal (D_1 and D_2) has a strong effect on T_2. Regardless the axes configuration, increasing the magnetic field and lowering the temperature assures a higher T_2 [44].

The population lifetime sets an upper bond to the coherence time given by equation (2.12) and gives the time scale of the population dynamics. Therefore, we measured first the population lifetime of the transition. This was done by using the previously mentioned SHB technique. The transition was saturated using a monochromatic pulse. Then, a laser was swept across the transition to measure the hole height. This swept laser was applied after different time delays after the burning pulse. Measuring the height of the hole as a function of the delay between the sweep and the burning pulse is a way to estimate the population lifetime T_1. In figure 6.12, the logarithm of the amplitude of the hole as a function of time is presented.
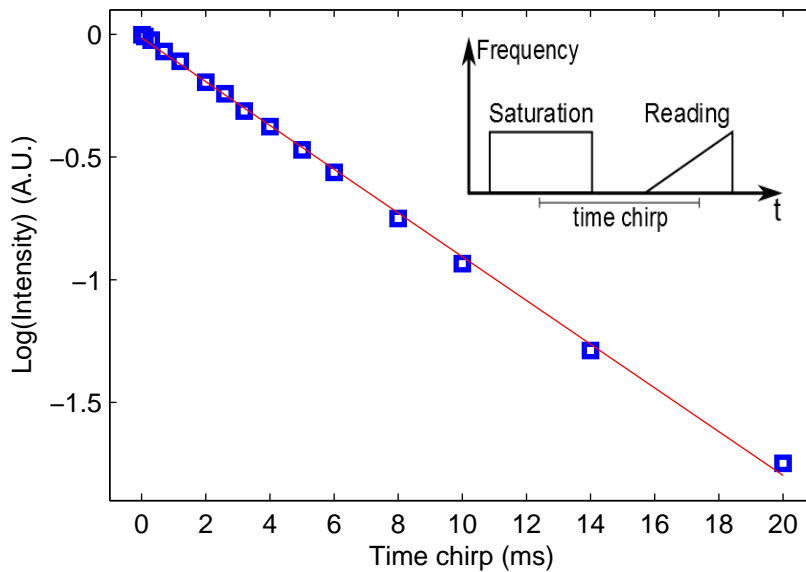
Figure 6.12: Logarithm of the hole amplitude as a function of the time between the pulse used to saturate the transition and the reading pulse. The population lifetime is given by $T_1= 11.2$ ms.

From the linear fitting of the data, the population lifetime of the excited state is given by: $T_1= 11.2$ ms. This value is in agreement with the values reported in section 2.4. However, as it was explained in section 2.4, different interactions affect the rephasing of the coherences. Additionally, Er^{3+}:Y_2SiO_5 is characterized by its high anisotropy regarding its g-factors for both ground and excited state (see figure 2.8).

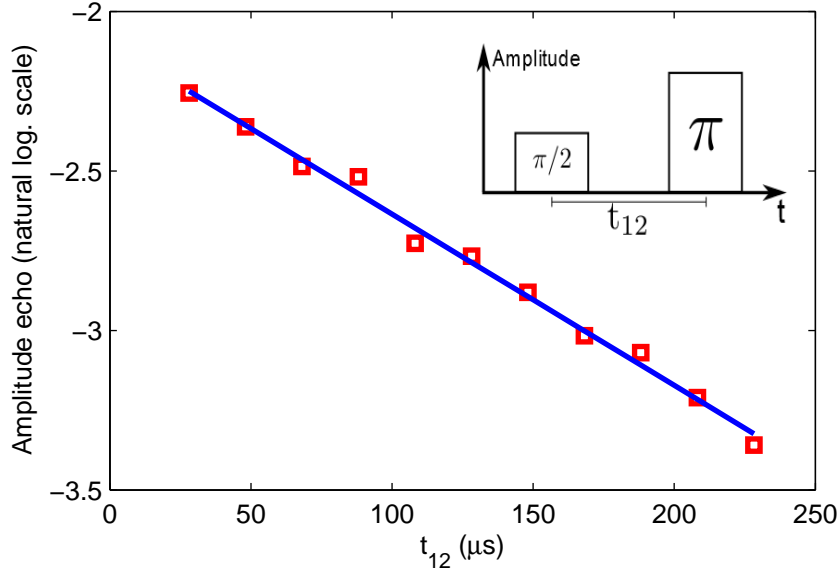**Figure 6.13:** Logarithm of the echo amplitude as a function of t_{12} for a two-pulse photon echo sequence at 2.6 T and 1.75 K. The coherence time for this measurement is given by $T_2 = 745$ μs.

Thus, the T_2 varies greatly for different orientations and magnitude of the magnetic field. In figure 6.13, a coherence time measurement performed using the two-pulse photon echo sequence is shown. This experiment was performed at 2.6 T and a temperature of 1.75 K, and the coherence time measured to be $T_2 = 745$ μs.

Even at a higher temperature (2 K) and a smaller magnetic field (2 T), we have measured a good coherence time: $T_2 = 307$ μs. This shows the potential of using erbium in a Y_2SiO_5 matrix. As the coherence time is quite dependent on the temperature, the orientation and the amplitude of the magnetic fields, it is important to remeasure the coherence time regularly for different experimental conditions.

ROSE efficiency
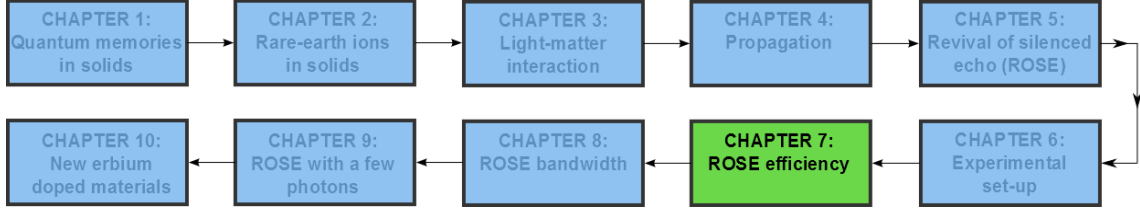
In this chapter I will present the first results of the ROSE protocol efficiently implemented in Er^{3+}:Y_2SiO_5. As ROSE protocol uses adiabatic rapid passages (ARP) instead of π-pulses, I start this chapter explaining how the pulses were chosen to accomplish the adiabatic condition. In the last section I will measure the efficiency of the protocol for a fixed bandwidth.

7.1 Characterization of the rephasing pulses

7.1.1 Investigating the adiabatic condition

As ROSE protocol uses ARP, we need to analyze the adiabatic condition in our system to accomplish a good rephasing of the coherences. The quality of the rephasing pulses can be evaluated by verifying the inversion of the medium after the first pulse and the return to the ground state (double inversion) after the second one.

The adiabatic condition (equation (5.25)) sets an upper bond to the chirp rate of the CHS. The CHS are chosen such as $\sqrt{\mu}\beta$ is less than the Rabi frequency. But how much less? We have to optimize the parameters to obtain a good inversion with a reasonable fast chirp rate.

This study was exceptionally done using a smaller crystal than the one presented in section 6.1. We initially studied the rephasing pulse inversion in a 1 x 1 x 10 mm^3 crystal, with the b-axis along the 10 mm side. First of all, as the upper bond of the inequality is given by the Rabi frequency, we measured the Rabi frequency using the nutation, as explained in section 6.5. In figure 7.1, the nutation for this crystal is presented. The Rabi Frequency in this case is given by $\Omega_0 \approx 2\pi \times 105$ kHz. This value is much shorter than the one presented in section 6.5 ($\Omega_0 \approx 2\pi \times 800$ kHz). This difference comes from the fact that the former measurement was done with a

smaller waist for a comparable laser power.
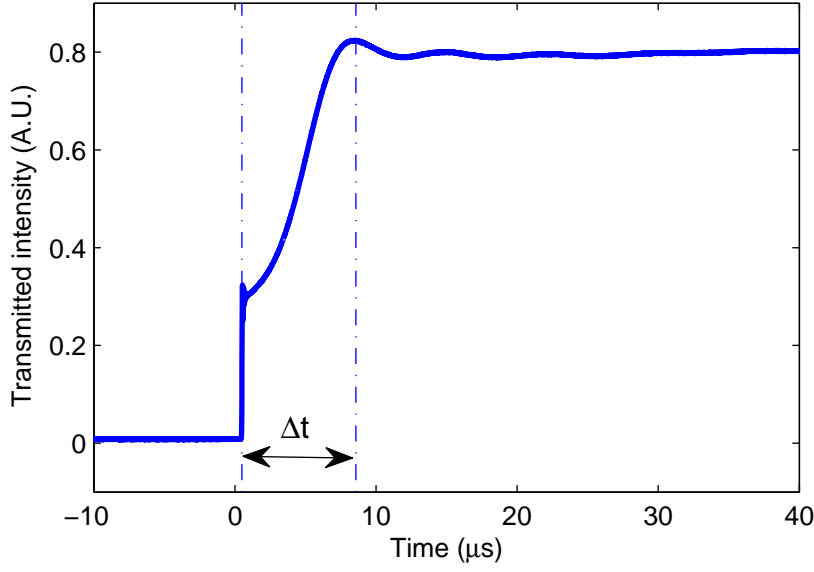
Figure 7.1: Nutation curve for the rephasing pulses beam in a 1 x 1 x 10 mm^3 Er^{3+}:Y$_2$SiO$_5$ crystal. The Rabi frequency is given by $\Omega_0 \approx 2\pi \times 105$ kHz.

To investigate the adiabatic condition, we decided to study the single and double inversion efficiency as a function of $\sqrt{\mu}\beta$. To measure the inversion efficiency, first a weak pulse was sent to the crystal. Then, one or two CHS were sent to the crystal to invert one or two times the medium respectively. Finally, a probe pulse was sent to the crystal.

In figure 7.2 I present an example of the single inversion in (a) and the double inversion in (b).

(a)   (b)

Figure 7.2: Single inversion measurement in (a) and double inversion in (b).

We can notice that after one CHS, as the medium is inverted, the probe is amplified. On the other hand, when two CHS are applied, a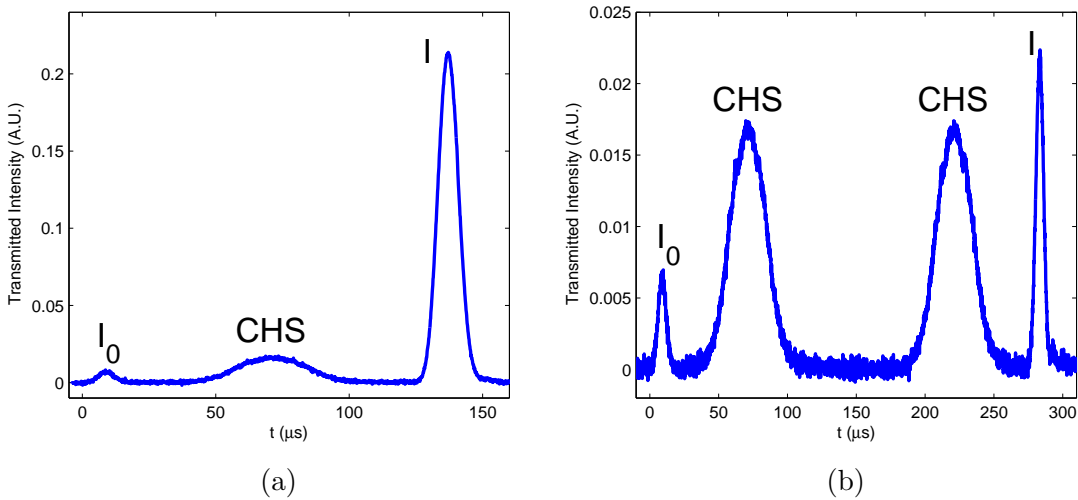s most of the atoms are in the ground state, the input pulse and the probe pulse are similar. Using the optical depth (measured using the SHB technique), the excited state population n_e is given by:

$$n_e = \frac{\ln(I/I_0)}{2\alpha\mathrm{L}} \tag{7.1}$$

Using this equation, the population transferred to the excited state (single inversion), shown in figure 7.3(a), and the excited state population (double inversion), shown in figure 7.3(b) were calculated. The solid curves in blue are drawn to guide the eye. These measurements were performed by fixing a value of μ, with $\mu = 1, 4, 16, 36$ and varying β from $2\pi \times 5$ kHz to $2\pi \times 25$ kHz. However, the measurements are presented as a function of $\sqrt{\mu}\beta$, the relevant parameter to estimate when the adiabatic condition is accomplished.

Figure 7.3: Excited state population as a function of $\sqrt{\mu}\beta$ after a single inversion in (a) and a double inversion in (b). Solid curves in blue are drawn to guide the eye.

The dotted lines in figure 7.3 show the maximum inversion efficiency. We can clearly see a decay of the efficiency around these lines. To the left of the dotted lines, the decay is related to the low μ parameter used to invert the medium. Even if the adiabatic condition is accomplished, it has been show that efficient population transfer can be achieved if $\mu > 1$. On the other hand, the decay that we see on the right side comes from the fact the value of $\sqrt{\mu}\beta$ is getting closer to the value of Ω_0^2. Thus, the Bloch vector does not follow adiabatically the driving vector.

These measurements show the importance of the inversion analysis to choose the best parameters for the CHS pulses. From the measurements presented in figure 7.3, we took the following relation between the CHS parameters and the Rabi

frequency to optimize the inversion of the medium:

$$\sqrt{\mu}\beta = \frac{\Omega_0}{2} \tag{7.2}$$

This relation was also verified for the crystal that we used to perform the ROSE protocol (3 x 4 x 5 mm^3 crystal instead of 1 x 1 x 10 mm^3). For this crystal, the Rabi frequency was given by $\Omega_0 = 2\pi \times 800$ kHz. Thus, the best inversion was obtained by taking:

$$\sqrt{\mu}\beta = 2\pi \times 400 \text{ kHz} \tag{7.3}$$

From now, all the measurements are performed under this condition, assuring the best double inversion efficiency.

7.1.2 Maintaining the adiabatic condition

For a fixed value of $\sqrt{\mu}\beta$ verifying the adiabatic condition, μ or β can still be changed. Keeping constant the adiabatic condition $\sqrt{\mu}\beta = 2\pi \times 400$ kHz, we measured the single and double inversion efficiency as a function of μ for αL= 3.15. The results are shown in figure 7.4.
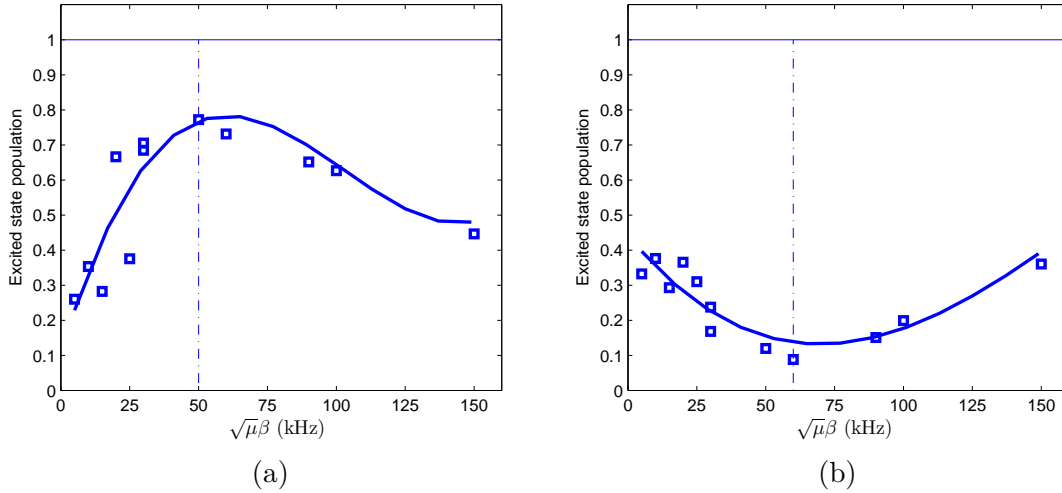

(a)   (b)
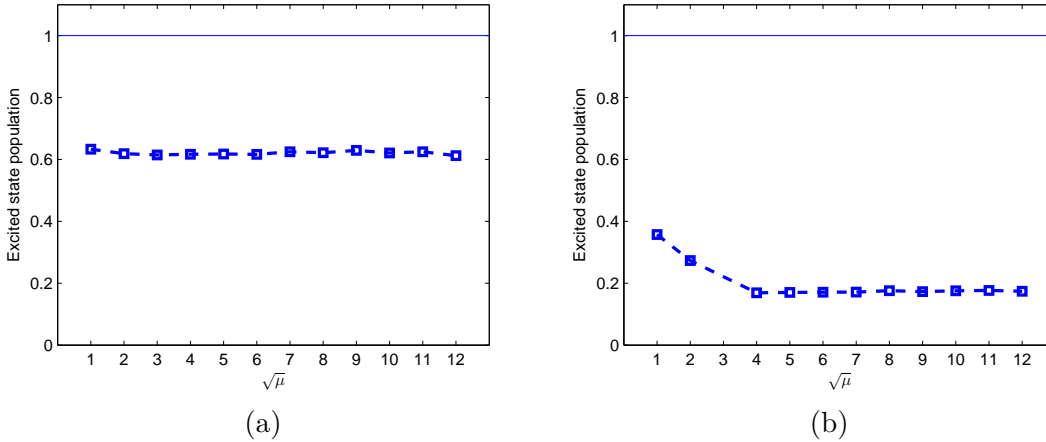
Figure 7.4: Excited state population as a function of $\sqrt{\mu}$ after a single inversion in (a) and a double inversion in (b) for a constant adiabatic condition $\sqrt{\mu}\beta = 2\pi \times 400$ kHz.

As we can appreciate from figure 7.4(b), the inversions are relatively constant because the adiabatic condition is maintained. The double inversion is still better when the value of μ is increased. However, increasing μ forces us to decrease β to keep the adiabatic condition constant. As the duration of the CHS is proportional to the inverse of β, we would have to make the total time sequence longer. This may limit the efficiency of the protocol.

Additionally, from figure 7.4, we can appreciate that the efficiency of the simple inversion (around 60%) is different from the double inversion (around 80%). It is possible to understand qualitatively this difference by looking at figure 7.5.
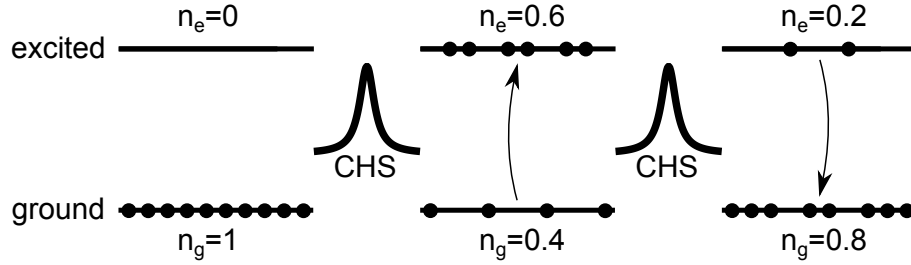
Figure 7.5: Levels scheme of the measurements presented in figure 7.4.

When the first CHS pulse inverts the medium, only 60% of the population is promoted to the excited state. When the second CHS pulse is applied on the system, as the medium is no longer absorbant, it is possible to consider that the CHS pulse only brings 60% of the excited atoms to the ground state, without modifying the atoms that were already in the ground state. This assumption allows us to estimate the ground state population after the two CHS, which will be $n_e = 0.6 \times 0.6 + 0.4 = 0.76$. Therefore, the expected double inversion efficiency is 76%, in agreement with our measurements.

Furthermore, the ions that remain in the excited state after applying the second CHS pulse may play a negative role when performing ROSE protocol at single photon level. These ions will spontaneously decay, emitting photons in the corresponding transition. In chapter 9, ROSE protocol is presented while working at single photon level.

Additionally, we measured the single and double inversion efficiency as a function of the optical depth, as shown in figure 7.6.
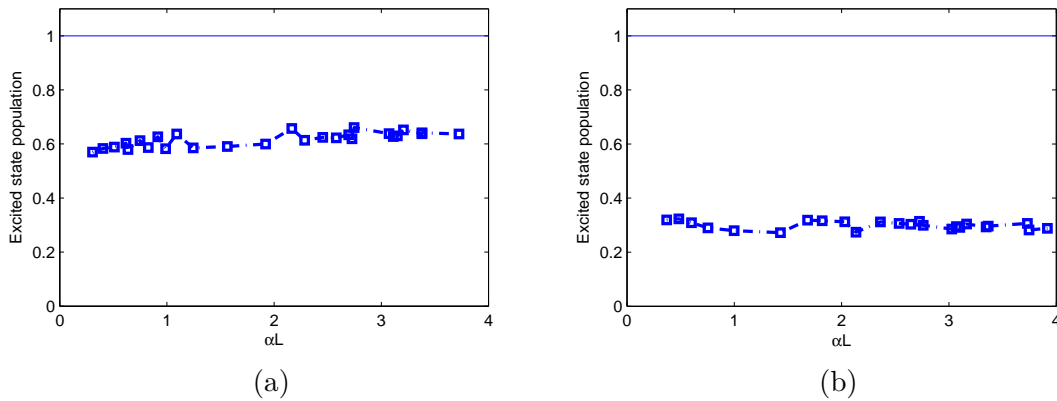

Figure 7.6: Excited state population as a function of the optical depth αL after a single inversion in (a) and a double inversion in (b).

The single and double inversion efficiency is approximately constant for different optical depths. The robustness of the CHS pulses even when propagating through a strongly absorbing medium is here verified.

7.2   ROSE efficiency

The efficiency of ROSE protocol was studied theoretically in section 7. To validate the model, we have measured the efficiency of the protocol as a function of the optical depth. The measurements were performed using $\mu = 1$ and $\beta = 2\pi \times 400$ kHz as parameters for the CHS. Although, the inversion efficiency is better for $\mu > 1$, when increasing its value we are forced to decrease β, resulting in longer CHS pulses. To avoid the overlapping between the CHS pulses, the time between them (t_{23}) has to be increased. This has a negative impact on the efficiency. In section 8.1, I will present in more detail how to adjust the time sequence to decrease β.

In figure 7.7 a measurement of the ROSE protocol is presented for $2t_{23} = 16$ μs and $t_{12} = 4$ μs. In red the input pulse (I_0), calculated using the optical depth and the blue pulse ($I_0 e^{-\alpha L}$), and, in blue, the output pulse (I). In between the blue pulses, I have represented the CHS pulses as a reference.
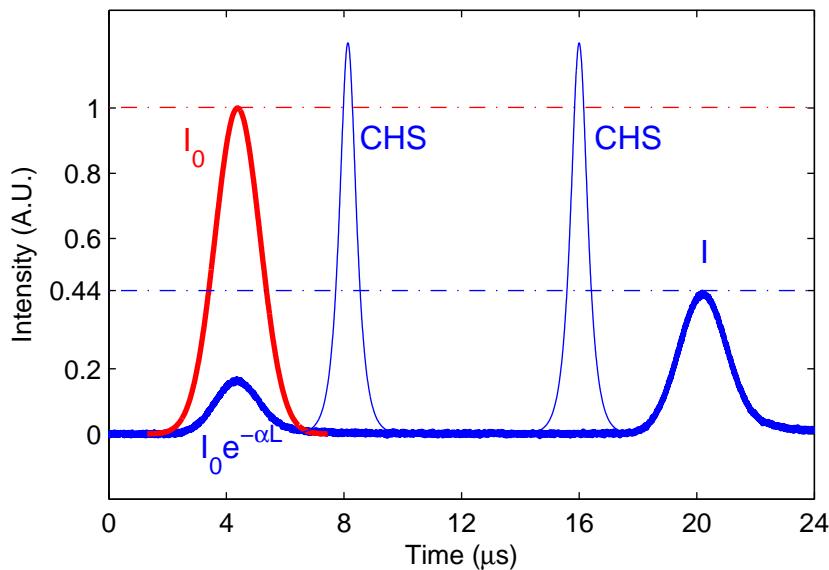

Figure 7.7: ROSE protocol for an optical depth of $\alpha L = 1.8$. The CHS pulses are drawn as a reference.

We have also studied the performance of the protocol while changing the duration of the input pulse (see figure 7.8). The other parameters (as μ and β) are fixed. As we use Gaussian pulses, the effective bandwidth corresponds to the inverse of their duration.
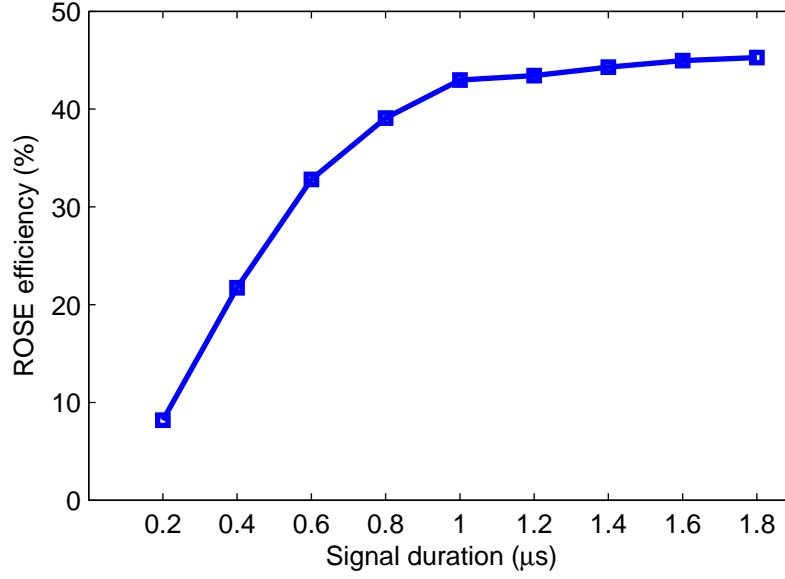
Figure 7.8: ROSE efficiency as a function of the signal duration for an optical depth of $\alpha L = 1.91$.

From a signal duration of approximately 1 μs, the efficiency is maximal. This result is reasonable for a Rabi frequency of 800 kHz. This latter parameter fixes the CHS parameters and the inversion bandwidth. Thus, all measurements were performed with a signal duration equal or greater than 1 μs.

As the minimum ROSE bandwidth used in all the experiments was 800 kHz, we can assure that the bandwidth of a 1 μs (or larger) signal pulse was always included in ROSE's bandwidth.

ROSE efficiency is quite dependent on the optical depth, as shown in equation (5.17). We make the optical depth vary by tuning the laser at different frequencies within the inhomogeneous linewidth. Although the Koheras laser is slowly tunable by temperature, we decided to shift the center of the inhomogeneous linewidth by slightly changing the magnetic field. This allowed us to perform the experiment much faster and in a more reproducible way than tuning the laser. As we worked at large magnetic fields (on the order of Tesla) and tens of mT is enough to cover the whole inhomogeneous linewidth, the change in the magnetic field does not have any appreciable influence on the coherence time.

In figure 7.9, the efficiency as a function of αL for a magnetic field close to 3.3 T and for $2t_{23} = 16$ μs is shown [85], for $\vec{B}$ making an angle of 160° with respect to D$_1$. The optical depth was obtained by using the SHB technique (see section 6.6) for each value of the magnetic field. We compared the experimental result with the theoretical prediction given by equation (5.17). For this, we need to measure the coherence time T_2. This measurement was performed in two independent ways.
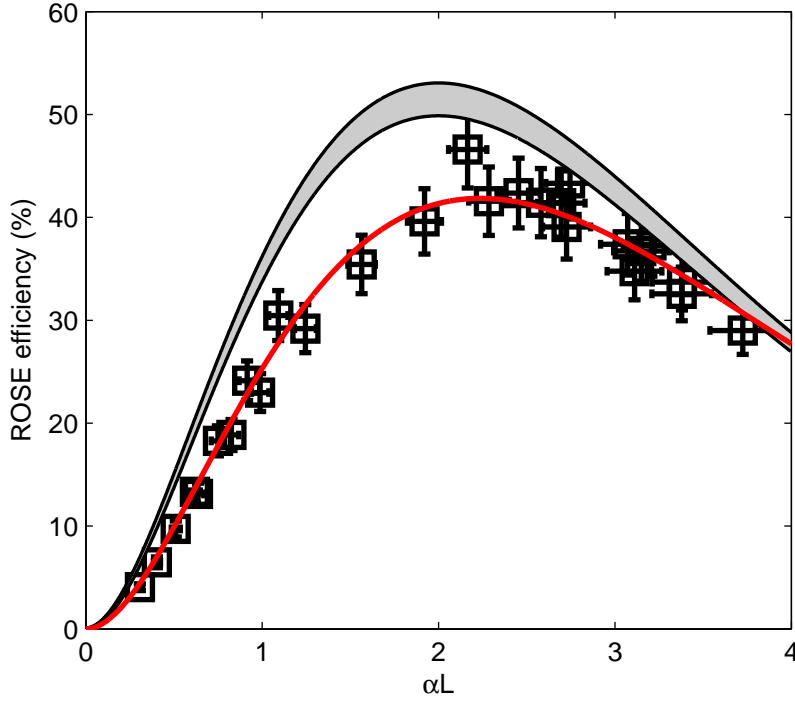
Figure 7.9: ROSE efficiency as a function of the optical depth αL.

First, the standard two-pulse photon echo ($\pi/2$-π sequence) was used, which gave us $T_2 = 1.4$ ms. We also measured it by using ROSE protocol by simply changing the time t_{23} between CHS pulses, where we obtained $T_2 = 400$ μs. The discrepancy is probably related to the instantaneous spectral diffusion that affects the rephasing of the coherences. As ROSE protocol inverts the whole excited bandwidth when the first CHS pulse is applied, a higher induced dephasing is expected and, thus, a lower coherence time. Furthermore, the excited bandwidth of the two-pulse photon echo might be lower than the bandwidth excited by ROSE protocol, which could explain the difference between the T_2 measured by both methods. In section 8.3, I will analyze the effect of ISD on ROSE protocol. We present a confidence interval in figure 7.9 (grey-shaded area), taking into account these two values of T_2. Qualitatively, the measurements and the theoretical efficiency show a similar behavior. The difference between them comes from the fact that equation (5.17) assumes that the inversion and rephasing process are perfectly done.

In section 5.5, I have presented a phenomenological model when the rephasing pulses do not fully invert the medium or when the rephasing process is imperfect. Adding ad-hoc coefficients, we have derived equation (5.40). We left the coefficients η_{pop} and η_{phase} as free parameters to fit the experimental data. We use the fixed value of $T_2 = 400$ μs measured using ROSE while varying t_{23}. The red curve in figure 7.9 is given by the least square optimization of this equation, which gives $\eta_{\text{pop}} = 80\%$

and $\eta_{\mathrm{phase}} = 85\%$. The analysis of these parameters is not simple. However, η_{pop} is clearly related to the inversion of the medium and its efficiency. For the experimented presented here, the ground state population (i.e. double inversion efficiency) was approximately 80% (see section 7.1.2), in agreement with the parameter η_{pop} used in the fitting.

ROSE Bandwidth
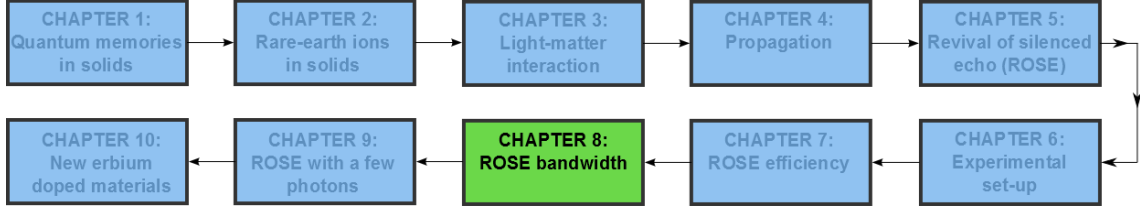
In the last section I presented the performance of ROSE protocol for a fixed bandwidth. The next step, to fully characterize ROSE protocol, is to study its behavior when increasing the bandwidth. Increasing the bandwidth means that we have to increase the CHS duration to maintain the adiabatic condition. I will first explain how the efficiency scales with the bandwidth when the CHS duration is modified. Afterwards, I will show how instantaneous spectral diffusion (ISD) affects the rephasing of the coherences when changing the protocol's bandwidth. Then, I will present a microscopical model to estimate the effect of ISD on photon echo protocols. Finally, I will resume how ISD affects ROSE protocol parameters and finish by introducing a strategy to reduce its effect on $Er^{3+}:Y_2SiO_5$.

8.1 Adjusting the time sequence

The bandwidth of the protocol can be easily increased by changing the parameters of the CHS (i.e. μ and β). However, as shown in section 5.4, when changing the bandwidth of ROSE protocol, the duration of the CHS have to be modified to keep the adiabatic condition constant. In this section, I present the methodology used to measure ROSE efficiency as a function of the bandwidth.

To prevent the overlap between the input pulse and the CHS and, also, between the CHS pulses when increasing the CHS bandwidth, t_{12} and t_{23} have to be modified. First of all, as presented in the last chapter, we choose to keep $t_{23} = 2_t12$ for which the efficiency is good. The duration of the CHS is $1/(\beta)$. In figure 8.1, the time sequence of the protocol including t_{12}, t_{23} and the duration of the CHS is shown. To avoid the overlap between pulses, we keep constant the following expression:

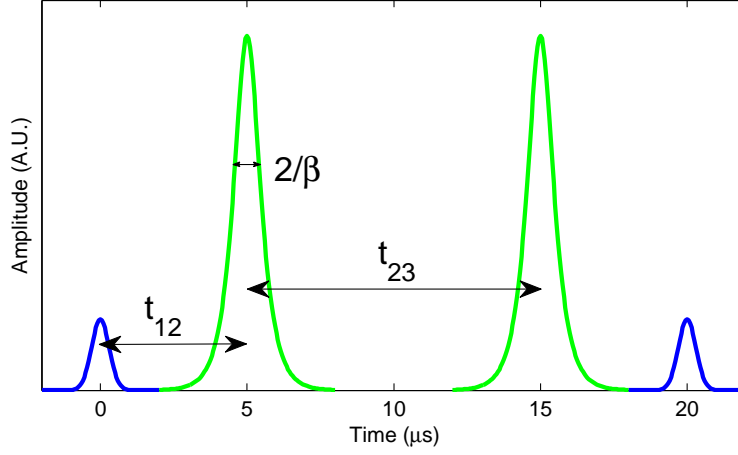$$\beta t_{23} = \text{cte} \qquad (8.1)$$

Figure 8.1: ROSE protocol sequence. t_{12} is the time between the input pulse and the first CHS, t_{23} the time between CHS and $1/\beta$ the duration of the pulses.

The value of the constant is given by an initial condition of β and t_{23}. For $\mu = 1$, $\beta = 2\pi \times 400$ kHz and $t_{12} = 5\,\mu s$, the minimum t_{23} is given by:

$$t_{23}^{\mathrm{min}} = \frac{8\pi}{\beta} \tag{8.2}$$

This expression can be rewritten as a function of the bandwidth BW of the protocol and the Rabi frequency of the system. Combining equation (7.2) with equation (8.2), we obtain the following expression:

$$t_{23} = \frac{16\pi}{\Omega_0^2}\mathrm{BW} \tag{8.3}$$

With this constraint, it is possible to rewrite the efficiency as a function of the bandwidth:

$$\eta = (\alpha L)^2 \exp(-\alpha L) \exp\left(-\frac{64\pi}{\Omega_0^2 T_2}\mathrm{BW}\right) \tag{8.4}$$

Additionally, the logarithm of the efficiency decreases linearly with the bandwidth, where the slope depends on the coherence time:

$$\ln \eta = \ln(\eta_0) - \frac{64\pi}{\Omega_0^2 T_2}\mathrm{BW}\,, \tag{8.5}$$

where $\eta_0 = (\alpha L)^2 \exp(-\alpha L)$.

In figure 8.2, the efficiency and the logarithm of the efficiency are shown as a function of the excited bandwidth, for $T_2 = 500\ \mu s$, $\Omega_0 = 2\pi \times 800$ kHz and $\alpha L = 2$. These parameters are similar to the ones from our experiment. We can clearly see that when the bandwidth is increased, the efficiency decays. This is due to the limited coherence time.
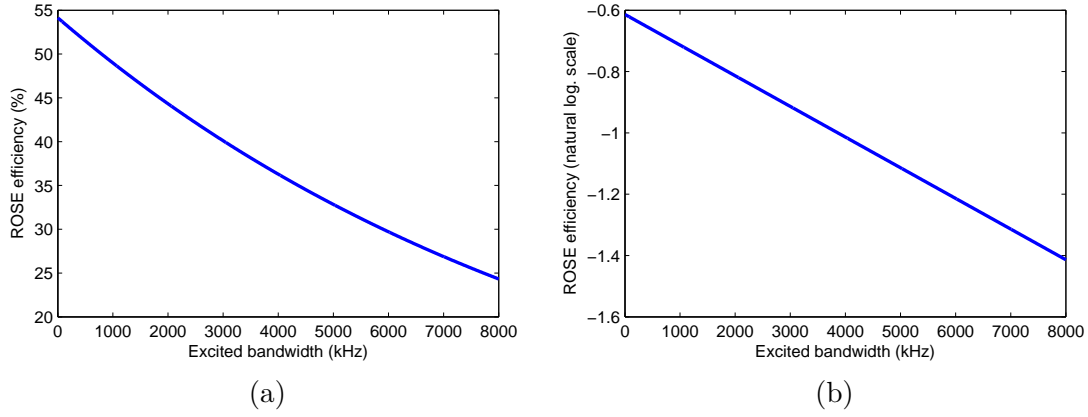
Figure 8.2: Theoretical ROSE efficiency as a function of the excited bandwidth BW.

In the next section I will present the efficiency measurements while changing the bandwidth of the protocol, and analyze the discrepancy with the predicted performance of the protocol.

8.2   ROSE efficiency as a function of the bandwidth

Following the approach presented in the last section we measured ROSE efficiency as a function of its bandwidth. We expect an exponential decay of the efficiency (figure 8.2). In figure 8.3, ROSE efficiency as a function of the excited bandwidth BW is presented in (a) while its logarithm is shown in (b).

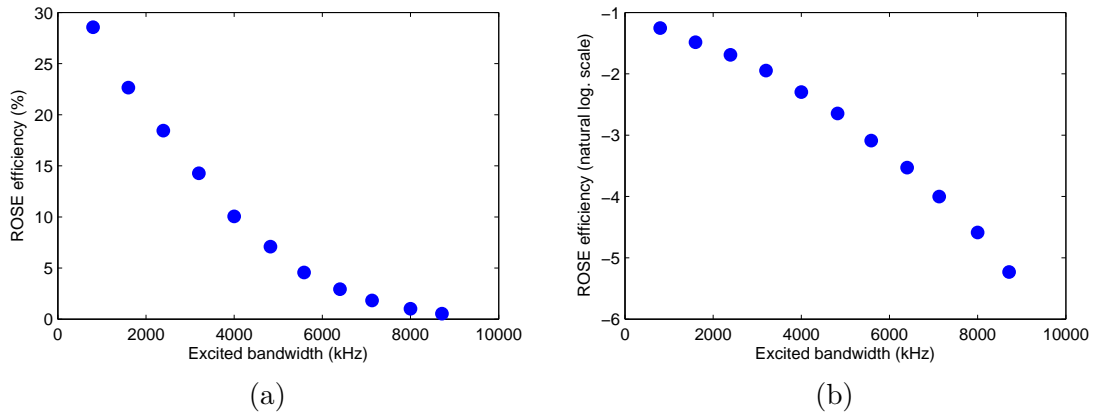**Figure 8.3:** Experimental ROSE efficiency as a function of the excited bandwidth BW.

Although we expected to measure a linear behavior for the natural logarithm of the efficiency (figure 8.3(b)), as predicted by equation (8.5), we observe a non linear decay. This measurement suggests that there is another process affecting the

rephasing of coherences that we did not consider yet. First of all, we should consider that the inversion made by the CHS pulses is not necessarily constant for different μ and β. However, this difference cannot explain the effect seen in figure 8.3(b), as the inversion is approximately constant for $\mu > 1$. Furthermore, the decay observed in that figure corresponds to a quadratic decay, which suggests that this unexpected interaction scales linearly with ROSE's bandwidth. In the following section I will introduce a model to explain the change in the efficiency due to the interaction between erbium ions, called instantaneous spectral diffusion.

8.3 Measuring the instantaneous spectral diffusion (ISD)

8.3.1 ROSE efficiency model including ISD

As discussed in section 2.6, the dipole-dipole interaction between erbium ions may cause a sudden shift in the transition frequency of the neighboring ions. This interaction is a broadening source known as instantaneous spectral diffusion (ISD), and has a strong effect on the rephasing of the coherences. To account for this extra dephasing, we introduce a phenomenological bandwidth dependent parameter to the coherence time, which now will depend on the bandwidth [53, 86, 87]. In equation (2.15) I presented the linear relation between the bandwidth and the excited ions density n_e. Thus, we consider that the coherence time including extra dephasing is given by:

$$\frac{1}{T_2(\text{BW})} = \frac{1}{T_2^0} + \kappa \frac{\text{BW}}{2\pi} \tag{8.6}$$

This equation will give us an effective coherence time dependent on the excited bandwidth. When increasing the bandwidth, as more ions are being excited, the coherence time will be reduced. Thus, the efficiency will decay faster than predicted by equation (8.5) when ROSE's bandwidth is increased.

From equation (8.6), we can rewrite the efficiency given in equation (8.4) as:

$$\eta = (\alpha L)^2 \exp(\alpha L) \exp\left[-\frac{64\pi}{\Omega_0^2} \text{BW} \left(\frac{1}{T_2^0} + \kappa \frac{\text{BW}}{2\pi} \right) \right] \tag{8.7}$$

To include the coherence time $T_2 = 500$ μs previously measured for a bandwidth $\text{BW} = 2\pi \times 800$ kHz , equation (8.7) can be rewritten:

$$\ln(\eta) = \ln(\eta_0) - \frac{64\pi}{\Omega_0^2} \text{BW} \left(\frac{1}{T_2(\text{BW}_{800})} + \kappa \left(\frac{\text{BW}}{2\pi} - \frac{\text{BW}_{800}}{2\pi} \right) \right], \tag{8.8}$$

where $\ln(\eta_0) = \ln((\alpha L)^2 \exp(-\alpha L))$, $T_2(BW_{800})$ is the coherence time for $BW = 2\pi \times 800$ kHz and $BW_{800} = 2\pi \times 800$ kHz. Equation (8.8) has only one free parameter, κ, that characterizes the effect of ISD.

We measured ROSE efficiency as a function of its bandwidth for different orientations of the crystal with respect to an external magnetic field. As shown in section 2.6, ISD is strongly dependent on the orientation. This is particularly important for Er^{3+}:Y_2SiO_5 whose g-factors are highly anisotropic. In figure 8.4(a), the natural logarithm of ROSE efficiency as a function of the bandwidth is shown for a magnetic field $\vec{B} = 2$ T [88]. In this measurement $\vec{B}$ makes an angle of $135°$ with respect to D_1. We initially used this angle because, as demonstrated by Böttger and coworkers [45], it optimizes the coherence time.
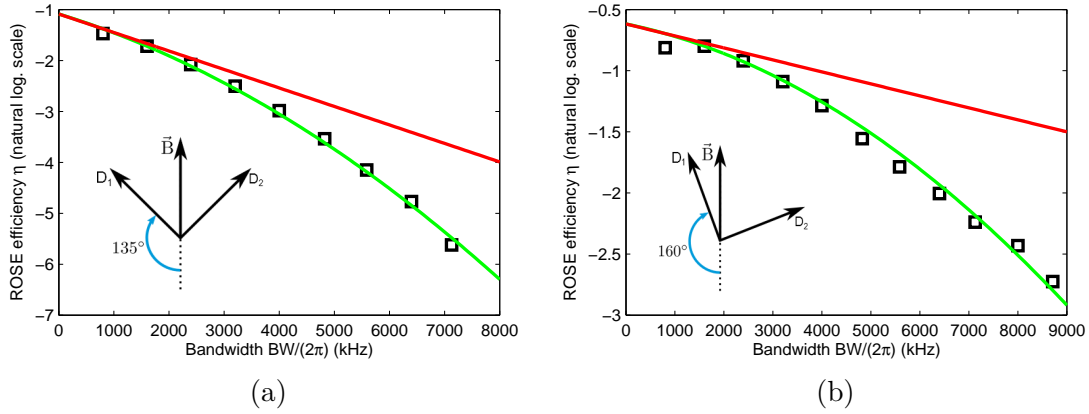

(a)   (b)

Figure 8.4: Natural logarithm of ROSE efficiency as a function of the bandwidth. In (a) for $\alpha L = 3.4$. The red line corresponds to the expectation of equation (8.5) with the parameters $\eta_0 = 34\%$ and $T_2 = 138$ μs. In (b) for $\alpha L = 1.6$. The red line corresponds to the expectation of equation (8.5) with the parameters $\eta_0 = 48\%$ and $T_2 = 400$ μs. The quadratic fits (green line) include the influence of instantaneous spectral diffusion, as given by equation (8.8).

For this first orientation, the red line in figure 8.4(a) corresponds to the prediction given by equation (8.5) while the green fits account for ISD, as predicted by equation (8.8). This fitting was done using the following parameters $\eta_0 = 34\%$ and $T_2 = 138$ μs, which were measured using ROSE protocol. From the fitting we obtain an ISD coefficient of $\kappa = 0.88$ s^{-1} kHz^{-1} for $\alpha L = 3.4$.

In order to see how ISD is affected by the angle between the magnetic field and the axes of the crystal, we measured ROSE efficiency as a function of the bandwidth for a different orientation. For the second orientation, $\vec{B}$ makes an angle of $160°$. In figure 8.4(b) the natural logarithm of the efficiency as a function of the bandwidth is shown. We obtain an ISD coefficient of $\kappa = 0.48$ s^{-1} kHz^{-1} for $\alpha L = 1.6$ and a magnetic field $\vec{B} = 3.3$ T.

The orientation of the crystal in this second measurement was not chosen by coincidence. As ISD depends on the difference between the magnetic dipoles in the excited and ground state (see equation (2.16)), minimizing its difference may be a way to reduce the effect of ISD. Looking at figure 2.8, we can notice that the difference of the g-factors is smaller for this orientation.

One could go further where the difference is much closer to zero, for example where $\vec{B}$ makes an angle of 20° with respect to D_1. However, with this orientation, the coherence time is greatly reduced because of the small absolute values of the g-factors.

Although this second orientation of the crystal gives a lower ISD coefficient, it is important to notice that ISD scales linearly with the optical depth. In the following section I will go back to that point to make a comparison between different measurements. Furthermore, I will introduce an independent way to measure ISD.

8.3.2   Independent measurement of ISD coefficient

From a different point of view, ROSE protocol provides a straightforward way of measuring and quantifying the effect of the coupling between erbium ions because of the induced dephasing. However, as the targeted ions and the ones that affect the coherence time are optically overlapped, the ISD analysis is rather complicated. This is also the case for the experiments performed by Liu and coworkers [53, 54]; where the dephasing is caused by changing the intensity of the second pulse in a two-pulse photon echo experiment.

In order to verify the ISD results that we obtained using ROSE, we decided to use a different method where the dephasing is caused by an auxiliary subgroup of ions, at a different spectral position in the inhomogeneous profile. This method ensures that the ions are interacting through dipole-dipole coupling and discards a possible effect mediated by light. These type of experiments were already performed in rare earth materials such as Eu^{3+}, Pr^{3+} and Nd^{3+} by Mitsunaga and coworkers [89] and by Graf and coworkers [86]. In those experiments, the two-pulse photon echo protocol is used to measure the coherence time while another laser, slightly shifted in frequency, excites a different subgroup of ions within the inhomogeneous linewidth. If this auxiliary excitation, called scrambler, affects the coherence time, we can assure that the ions are either magnetically or electrically coupled.

Following Mitsunaga approach, we performed a two-pulse photon echo experiment with a scrambler pulse, as shown in figure 8.5. To perform the experiment we used the same optical set-up than for ROSE protocol (see figure 6.2), using the signal beam to apply the two-pulse photon echo sequence and the rephasing beam to

apply the scrambler pulse. The scrambler pulse is a CHS whose behavior has been characterized in section 7.1. As shown in the scheme in figure 8.5, the scrambler pulse was AOM shifted by 10 MHz from the ions targeted by the two-pulse photon echo sequence.
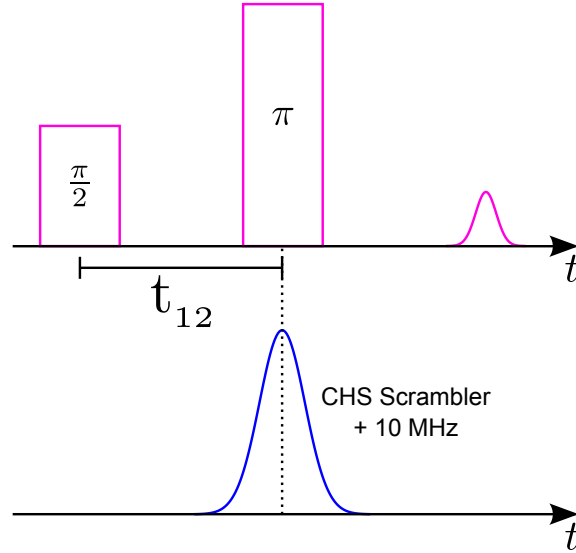

Figure 8.5: Temporal scheme to measure the influence of ISD in a two-pulse photon echo protocol. One beam is used to measure the coherence time using while the other one, called scrambler, targets ions shifted 10 MHz from the signal beam.

It is important to point out that the scrambler pulse must be applied between the first pulse and the echo in order to see the effect of ISD. Otherwise, the photon echo sequence will compensate any extra dephasing which is caused before the first pulse.

The two-pulse photon echo is repeated for several values of t_{12} to measure the coherence time. This procedure was reproduced for an increasing value of the scrambler bandwidth. We performed the experiment for the two D_1-D_2 axes configuration presented in section 8.3.1. The scrambler bandwidth was varied from $2\pi \times 0$ kHz to $2\pi \times 7100$ kHz for the first configuration and up to $2\pi \times 8000$ kHz in the other one.

In figure 8.6(a) the homogeneous linewidth as a function of the scrambler bandwidth is presented for D_1 making an angle of 135° [88] and, in figure 8.6(b), for D_1 making an angle of 160°.

In both figures we can clearly see the dephasing induced by the scrambler pulse. Furthermore, the homogeneous linewidth shows a linear behavior, as predicted by equation (8.6). The linear fitting in figure 8.6(a) gives an ISD coefficient of $\kappa_{ind} = 0.88$ s^{-1}kHz^{-1}, in agreement with the value obtained in section 8.3.1 ($\kappa = 0.8$ s^{-1}kHz^{-1}). For the other configuration (figure 8.6(b)) the fitting gives an ISD coefficient of $\kappa_{ind} = 0.82$ s^{-1}kHz^{-1}, also comparable with the value calculated in the former section ($\kappa = 0.48$ s^{-1}kHz^{-1}). The difference between these

values comes from the fact that the measurements were performed at different optical depths. Although both methods to measure ISD (ROSE protocol and two-pulse
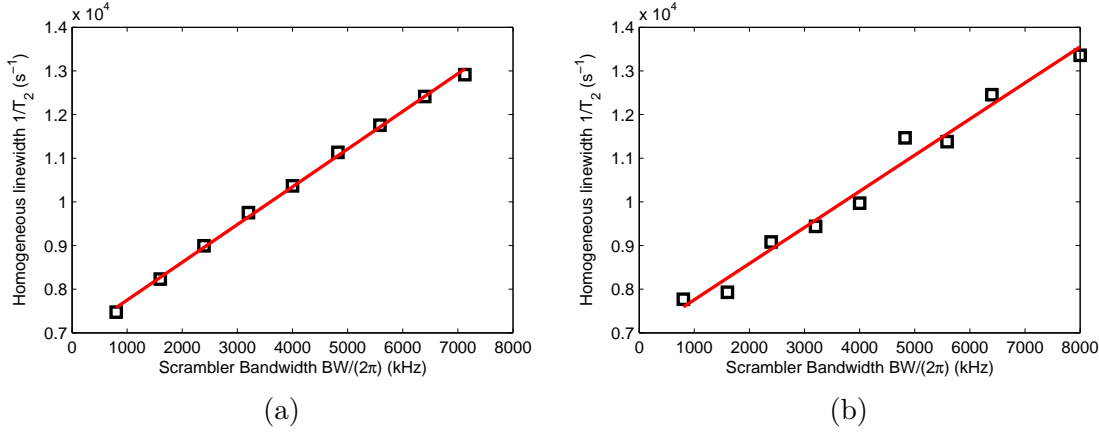

Figure 8.6: Homogeneous linewidth $(\frac{1}{T_2})$ as a function of the scrambler bandwidth BW. In (a) the magnetic field makes an angle of 135° respect to D_1 while, in (b) 160° respect to D_1.

photon echo plus a scrambler) show a similar ISD coefficient, both measurements were performed at different position in the inhomogeneous profile (i.e. different optical depths). As ISD is dependent on the density of ions, we should normalize the values to the optical depth αL. In table 8.1, the ISD coefficients normalized to their optical depth are presented.

If we normalize the ISD factors for an angle of 135° respect to D_1, we obtain normalized ISD factors of: $\kappa_{norm} = 0.26$ s^{-1}kHz^{-1} and $\kappa_{norm_{ind}} = 0.30$ s^{-1}kHz^{-1} in units of αL; for the measurements with ROSE protocol and with two-pulse photon echo respectively. The agreement between the normalized ISD coefficients is still good. In any case, we should consider that both measurements were performed at high absorption and the measurement of the optical depth present a considerable error (that I do not consider here).

On the other hand, for an angle of 160° respect to D_1, the normalized ISD factors are: $\kappa_{norm} = 0.30$ s^{-1}kHz^{-1} and $\kappa_{norm_{ind}} = 0.35$ s^{-1}kHz^{-1} in units of αL; for the measurements with ROSE protocol and with two-pulse photon echo respectively.

Orientation	κ_{norm}[s^{-1}kHz^{-1}] (ROSE)	$\kappa_{norm_{ind}}$[s^{-1}kHz^{-1}] (2PE + Scrambler)
135°	0.26	0.30
160°	0.30	0.35

Table 8.1: Normalized ISD coefficients measured using ROSE protocol and two-pulse photon echo plus a scrambler pulse for two orientation of the crystal respect to D_1.

Lastly, I would like to point out that the procedure presented in this section

to measure the influence of ISD is hard to carry out. As the coherence time has to be measured for every scrambler bandwidth, a high stability of the temperature and magnetic field in time is required. On the other hand, ROSE protocol offers an easy and reproducible way to measure the ISD coefficient. The time required to measure the ISD coefficient using ROSE protocol is of approximately 10% the time needed to run the independent measurement presented in this section.

8.4 Estimation of ISD from a microscopic point of view

In section 2.6, I presented a brief analysis of ISD and how to estimate its contribution to the homogeneous linewidth. From equation (2.15), we can calculate the broadening if the constant that describes the interaction (A) and the spatial density of excited ions (n_e) are given. It is not straightforward to evaluated the total fraction of atoms that are excited by a pulse. Recently, Thiel and coworkers showed a way to measure ISD without knowing the excited spatial density [90]. In our case, as ROSE protocol uses complex hyperbolic secants, we can assume that a CHS fully inverts a given bandwidth [91, 83]. Therefore, we estimate n_e directly from the CHS bandwidth.

Considering that inhomogeneous linewidth has a Lorentzian shape and assuming that the excited ions are located at the center of the line, the excited fraction n_e is given by:

$$n_e = n_Y C \frac{2}{\pi \Gamma_{inh}} BW \, , \tag{8.9}$$

where n_Y is the spatial density of yttrium ions in the structure, C the dopant concentration (in % or ppm) and Γ_{inh} the inhomogeneous linewidth. In Y_2SiO_5, the spatial density of yttrium is $n_Y = 1.83 \times 10^{22}$ cm^{-3}. The dopant concentration of the crystal used for this experiment was 50 ppm. However, as the erbium substitutes equally two sites of yttrium in Y_2SiO_5 (site 1 and 2), we consider that $C = \frac{1}{2} \times 50$ ppm. We have measured $\Gamma_{inh} = 2\pi \times 630$ MHz (see figure 6.7) for site 1 under study.

The broadening caused by dipolar interactions will modify the coherence as:

$$\frac{1}{T_2(B)} = \frac{1}{T_2^0} + \frac{1}{4} \Delta \omega \, , \tag{8.10}$$

where $\Delta \omega$ is given by equation (2.15). Therefore, the ISD coefficient is given by:

$$\kappa_\mu = \frac{8\pi^3}{9\sqrt{3}} A n_Y C \frac{2}{\pi \Gamma_{inh}} \, , \tag{8.11}$$

where A is composed of both magnetic and electric dipole-dipole interactions. To account for the magnetic interaction, A_{mag} is given by:

$$A_{\mathrm{mag}} = \frac{\mu_0 \hbar}{4\pi} \left| \Delta \vec{\mu}_{\mathrm{mag}} \right|^2 \, , \tag{8.12}$$

where $\Delta \vec{\mu}_{\mathrm{mag}}$ is the difference of the magnetic moment (either electronic or nuclear) between the ground and the excited state (units of $T^{-1}\mathrm{rad\,s^{-1}}$). In $Er^{3+}:Y_2SiO_5$, the contribution can be calculated from the moment tensor [34] 2.3. Using this tensor for the magnetic field making an angle of $135°$ with respect to D_1, the magnetic coupling constant is given by $A_{\mathrm{mag}} = 2.8 \times 10^{-19}\,\mathrm{m^3\,rad\,s^{-1}}$.

We have also to consider the electric dipole-dipole interaction whose coupling constant is given by:

$$A_{\mathrm{el}} = \frac{1}{4\pi\epsilon_r\epsilon_0\hbar} \left| \Delta \vec{\mu}_{\mathrm{el}} \right|^2 \, , \tag{8.13}$$

where $\Delta \vec{\mu}_{\mathrm{el}}$ is the difference of the electric moment (units of C.m), ϵ_r the relative permittivity and ϵ_0 vacuum permittivity. This parameter is usually measured from the frequency shift given by the Stark effect. To our knowledge, the Stark shift tensor has not been measured for $Er^{3+}:Y_2SiO_5$. However, Macfarlane in 2007 published a series of Stark shifts for different rare earth materials in different host materials [92]. The variation between different rare earth materials is rather small, and in between erbium ions in different host matrix, the variation is even smaller. So we consider as a reference the Stark shift for $Er^{3+}:LiNbO_3$, 25 kHz/(V cm^{-1})[93]. We decided to use this one as this is the only value published for the transition $^4I_{13/2} \rightarrow {}^4I_{15/2}$. This Stark shift gives an electric moment of $|\Delta\vec{\mu}| = 1.65 \times 10^{-31}$ C m. Using the relative permittivity perpendicular to the C_2 axis $\epsilon_r = 4$ [94], we obtain a coupling constant for the electric moment of $A_{\mathrm{el}} = 5.8 \times 10^{-19}\,\mathrm{m^3\,rad\,s^{-1}}$. Although the coupling constant of the electric moment is larger than the one for the magnetic moment, we should consider that the Stark shift is unknown for $Er^{3+}:Y_2SiO_5$ and that the relative permittivity is very anisotropic in Y_2SiO_5. The order of magnitude of A_{el} is nevertheless relevant and cannot be neglected.

From the calculated values of A_{el} and A_{mag}, we obtain an ISD coefficient of $\kappa_\mu = 1\,\mathrm{s^{-1}\,kHz^{-1}}$ if we consider both interactions. The contribution of the magnetic dipole-dipole interaction to the ISD coefficient is typically one third.

The theoretical prediction $\kappa_\mu = 1\,\mathrm{s^{-1}\,kHz^{-1}}$ for the magnetic field making an angle of of $135°$with respect to D_1 is in good agreement with the measurements performed for that orientation: $\kappa = 0.8\,\mathrm{s^{-1}\,kHz^{-1}}$ and $\kappa_{ind} = 0.88\,\mathrm{s^{-1}\,kHz^{-1}}$. This confirms that both electric and magnetic dipole-dipole interaction generate ISD, affecting the rephasing of the coherences. Although there is a slight difference between

the measurements and the theoretical estimation we should consider that, first, no considerations were done regarding the errors in the measurements and, second, the Stark shift used in the theoretical calculation belongs to another material (similar to Er^{3+}:Y_2SiO_5).

8.5   Influence of the phonons on ISD

Up to now, we have assumed that ISD was due to the fluctuations in the local electric and magnetic fields of an ion caused by optical excitation of its neighbors. However, other interactions could add extra dephasing due to the homogeneous linewidth [95, 96].

In this section, we consider non-equilibrium phonons associated with non radiative decay of the excited ions. These phonons can either scatter or be reabsorbed by the erbium ions, generating an extra dephasing that might affect a coherent protocol where strong pulses are being used [97].

In this section, we analyze the contribution of phonons to the dephasing in Er^{3+}:Y_2SiO_5. To do this, we consider a similar experimental sequence to the one presented in section 8.3.2. This sequence consists of a two-pulse photon echo sequence with a scrambler pulse added to excite a large number of ions. We repeated this experiment for a scrambler CHS pulse of 5 MHz bandwidth, and measured the amplitude of the echo for three different positions of the scrambler with respect to the first pulse of the photon echo sequence. First, the scrambler before the sequence, then coincident with the first pulse (the $\pi/2$-pulse) and, finally, coincident with the second pulse (the π-pulse). In figure 8.7, the amplitude of the echo as a function of the scrambler position is presented. In blue the amplitude of the echo without the scrambler, while in red, the amplitude with the scrambler on.

If the scrambler pulse is applied before the two-pulse photon echo sequence, the ISD does not affect the rephasing of the coherences. However, phase dephasing due to the phonons interaction with the erbium ions is present during the whole sequence because the atoms will continuously decay after the application of the scrambler. As we can see in figure 8.7, the effect of applying the scrambler pulse before the photon echo sequence is not really appreciable because the echo amplitude with and without scrambler are similar. This demonstrates that we can disregard the extra dephasing induced by phonons. This analysis can be also applied to the case when the scrambler pulse is overlapped with the first pulse of the photon echo sequence.

Lastly, we can see the effect of ISD presented in the former sections when the scrambler pulse is overlapped with the second pulse of the photon echo sequence. As shown in figure 8.7 (black square), the amplitude of the echo is almost reduced
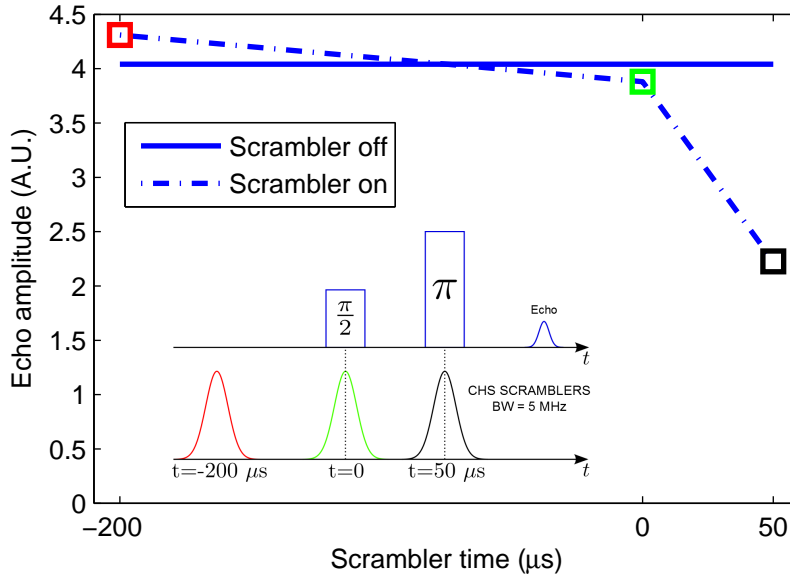
by half value when the scrambler pulse is on.

Figure 8.7: Echo amplitude as a function of the time when the scrambler pulse is applied on the two-pulse photon echo sequence.

8.6 ROSE performance including ISD

In section 1.2, I have presented useful features to evaluate the performance of a memory. In this section I will go through a few of them to analyze the influence of ISD on ROSE protocol.

8.6.1 Storage time, efficiency and bandwidth with ISD

As discussed in section 8.1, the parameters of the ROSE protocol are not independent. For example, for a fixed coherence time T_2 and laser power Ω_0^2, the bandwidth and efficiency are limited by the adiabatic condition. However, these constraints can be modified by, for example, increasing the Rabi frequency of the system. ISD adds a new constraint, acting on the coherence time. Here, I present the influence of ISD in the storage time, the efficiency, the bandwidth and the multiplexing capacity of the protocol:

- Storage time: as shown in equation (8.6), ISD limits the coherence time, imposing an upper bond to the storage time. This latter ultimately scales as $\frac{2\pi}{\kappa \text{BW}}$.

- Efficiency: in equation (8.8), the logarithm of the efficiency as a function of the bandwidth was presented. IDS adds a quadratic decay as a function of the bandwidth that might be critical for the performance of the protocol. However, by increasing the laser power Ω_0^2, it may be possible to overcome this problem. The consequence of following this approach is that the sequence must be shortened and, thus, the storage time would be shorter.

- Bandwidth: when the bandwidth is increased, the effect of the ISD on the rephasing of the coherences becomes more important, modifying the expected efficiency given by equation (8.5).

- Multiplexing capacity: one of the most important features of ROSE protocol is its high multiplexing capacity. The temporal multiplexing capacity is equivalent to the time-bandwidth product given by: $T_2(\text{BW}) \times \frac{\text{BW}}{2\pi}$. Theoretically, ROSE temporal multiplexing capacity is limited by the inhomogeneous linewidth of the material used to store the information. In the presence of ISD, this is, in general, no longer true. ISD will directly limit the multiplexing capacity of the protocol, which now scales as $1/\kappa$.

ISD limits the memory performance, specially when a high bandwidth is considered. A high bandwidth is one of most important requirements in several applications, as presented in section 1.1. That is why it is important to analyze the ISD source and find ways to diminish it.

From the ISD coefficient κ shown in equation 2.15, we can distinguish two ways to reduce the influence of ISD: reducing the erbium concentration C or reducing the dipole-dipole coupling constants A_{el} and A_{mag}. Reducing the erbium concentration of the crystal is the most straightforward option. When decreasing the concentration, we are simply increasing the distance between erbium ions. As ISD scales linearly with the concentration, for example, we should reduce the ISD coefficient 5 times if we go from a 50 ppm erbium concentration to a 10 ppm concentration. However, as the optical depth αL also scales linearly with the concentration, we have to increase the crystal length to keep its value and, therefore, the efficiency of the protocol.

The other option to reduce ISD is to decrease the coupling constants between erbium ions by minimizing the difference between their ground and excited dipole moments. For the electric dipole-dipole interaction is fixed for a given optical transition. On the other hand, the magnetic dipole interaction shows a high dependence on the angle between the magnetic field and the axis of the crystal. However, reducing the difference of the magnetic moments between the ground and excited state

might have an effect on the coherence time T_2^0, as the g-factors are involved in other static interactions. In the following section I will present an improvement analysis of the memory performance that can be done by rotating the crystal.

8.6.2 Optimization strategy for Er^{3+}:Y_2SiO_5

In this section, I will consider the magnetic field dependence of the coherence time T_2^0 and the ISD coefficient κ with respect to the orientation of the crystal. This allows us to find the optimal orientation for ROSE protocol.

Er^{3+}:Y_2SiO_5 has a highly anisotropic g-factors with respect to an external magnetic field [45] (see figure 2.8). This anisotropy affects the coherence properties. As ISD depends on the difference of the magnetic dipole between the excited and ground state, it might be possible to find an orientation of the magnetic field where this difference is minimized. However, we have also to consider that a low magnetic dipole (or g-factor), either for the ground and excited state will reduce the coherence time (T_2^0). Thus, there is a trade-off between minimizing ISD and keeping a good storage time.

In our analysis we only consider that the external magnetic field is applied on the D_1-D_2 plane. There are two reasons to choose this particular configuration. First, as explained in section 2.1, if the magnetic field is applied on that plane the sites are magnetically equivalent, avoiding a splitting of the transition (i.e. reducing the optical depth). Second, although we could apply the magnetic field along the b-axis to assure the equivalence between magnetic sites, Böttger and coworkers showed that the splitting of both ground and excited state can be maximized if the magnetic field is applied on the D_1-D_2 plane. As explained in section 2.3, a larger splitting reduces the mutual spin flip-flop interaction.

Knowing the behavior of T_2^0 and κ as a function of the angle Θ between the magnetic field B and the axis D_1 should allow us to predict the performance of our protocol. An experimental analysis would be extremely challenging as Er^{3+}:Y_2SiO_5 has a strong dependence of the g-factors with respect to the direction of an external magnetic field. If the crystal is rotated, the frequency of resonance will suffer a shift if the value of the magnetic field is not modified.

Therefore, we decided to study the angular dependence of those factors using their known (measured) values for certain angles. To do so we started using the $T_2^0(\Theta)$ for a 15 ppm Er^{3+}:Y_2SiO_5 crystal provided by Thomas Böttger [45]. For the ISD coefficient we used our measurement $\kappa = 0.8$ s^{-1}kHz^{-1} for an angle between D_1 and B of $\Theta = 135°$ (section 8.3.1). The other values of κ for other orientations of the field Θ will be deduced from the following model. The coefficient κ has an electric

and a magnetic contribution. In section 8.4, I showed that the magnetic dipole-dipole contribution is 0.33 s^{-1}kHz^{-1}, while the reminder (0.47 s^{-1}kHz^{-1}) comes from the electric dipole-dipole contribution.

Using equation (8.12), we were able to calculate the dependence of κ with respect to the orientation of the magnetic field. The angular dependence of the homogeneous linewidth ($1/2\pi T_2^0(\Theta)$) and the ISD coefficient $\kappa(\Theta)$ are shown in figure 8.8(a) and (b) respectively.
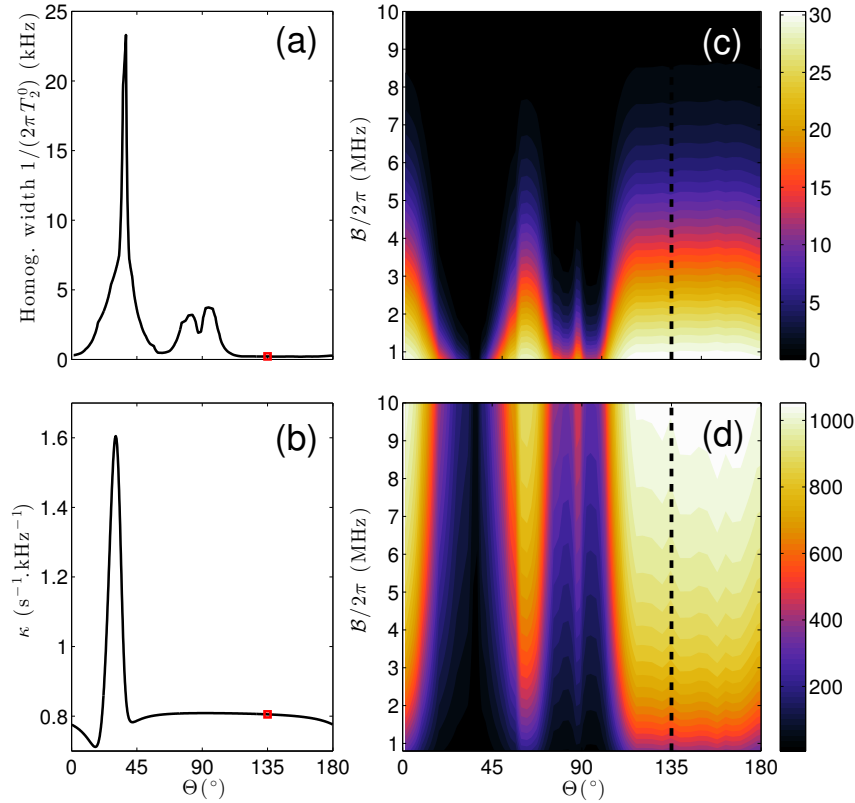

Figure 8.8: (a) (From [45], Copyright American Physical Society) Homogeneous linewidth $\frac{1}{2\pi T_2^0}$ at 3 T for 15 ppm concentration as a function of Θ, the magnetic field orientation in the plane D$_1$-D$_2$. (b) Theoretical variation in κ as a function of Θ. (c) Estimated ROSE protocol efficiency, in percent, as a function of the bandwidth B and the orientation Θ. (d) Time-to-bandwidth product as a function of the bandwidth B and the orientation Θ. In all figures, the orientations $\Theta = 0°$ or $180°$ and $\Theta = 90°$ correspond to D$_1$ and D$_2$ respectively. The two red squares in (a) and (b) and the dashed lines in (c) and (d) correspond to the experimental condition $\Theta = 135°$ of figures 8.4a and 8.6a. From [88].

Qualitatively figures (a) and (b) present the same behavior. This is reasonable and expected as the larger $\Delta\mu$ the more sensitive to spin flip-flop from neighboring erbium ions the system is and, coincidentally, the larger the ISD coefficient κ is.

Although this analysis gives an estimation of the coherence time extrapolated from [45] and the ISD coefficient deduced from one measurement (section 8.3.1), it is

useful to estimate the performance of ROSE protocol for $Er^{3+}:Y_2SiO_5$ as a function of the orientation of the magnetic field. We are particularly interested in evaluating the efficiency and multiplexing capacity (time-to-bandwidth product) as a function of Θ. From the values of $T_2^0(\Theta)$ and $\kappa(\Theta)$, we can estimate ROSE efficiency using equation 8.8 and the time-to-bandwidth product $T_2(BW) \times \frac{BW}{2\pi}$ as a function of the bandwidth using equation (8.6). We obtain the two graphs in figure 8.8(c) and (d) respectively.

As we can see from the dark regions in figure 8.8(c) and (d), and in coincidence with the presence of two peaks in figure 8.8(a) around $\Theta = 35°$ and $\Theta = 90°$, those angles should be avoided as they present the highest values of κ and/or the lowest values of T_2^0. On the other hand, the range $120° < \Theta < 180°$ is clearly the best configuration to run ROSE protocol. This justifies a posteriori the previously angle chosen.
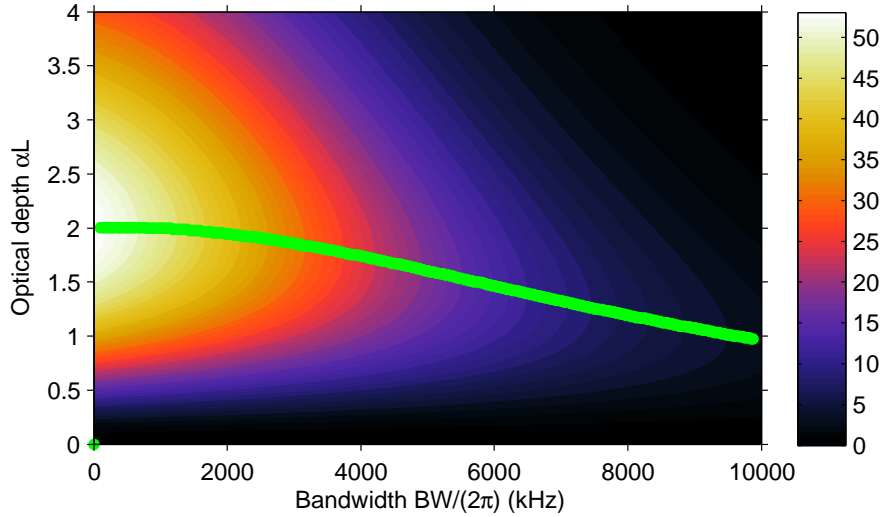

Figure 8.9: ROSE efficiency as a function of the optical depth αL and the bandwidth BW, including the effect of ISD. The green curve represents the αL that gives the maximum efficiency for a given bandwidth.

It is also important to consider that the ISD coefficient has a linear dependence with the optical depth αL. Thus, we can easily reduce ISD by shifting the laser away from the resonance. For example, here we started our estimation using a value of ISD given by $\kappa = 0.8 \text{ s}^{-1}\text{kHz}^{-1}$, measured at $\alpha L = 3.4$. If we consider $\alpha L = 1.7$, the ISD coefficient will be $\kappa = 0.4 \text{ s}^{-1}\text{kHz}^{-1}$. This is another degree of freedom that we can also take into account to improve ROSE performance. In figure 8.9, ROSE efficiency as a function of the excited bandwidth and the optical depth is shown.

Although the maximum efficiency is expected to be at $\alpha L = 2$, when the excited bandwidth is increased we might need to change the optical depth to increase

the efficiency. In figure 8.9, the green line indicates the position of the maximum efficiency for a given bandwidth. In order to obtain the maximum efficiency, it is advisable to measure the efficiency as a function of the optical depth for a fixed bandwidth. For example, at BW= $2\pi \times 800$ kHz the maximum efficiency is 49% at αL=2 but, if we move to a higher bandwidth BW= $2\pi \times 10000$ kHz, the maximum efficiency is 3.7% for an absorption αL=1.

ROSE with a few photons
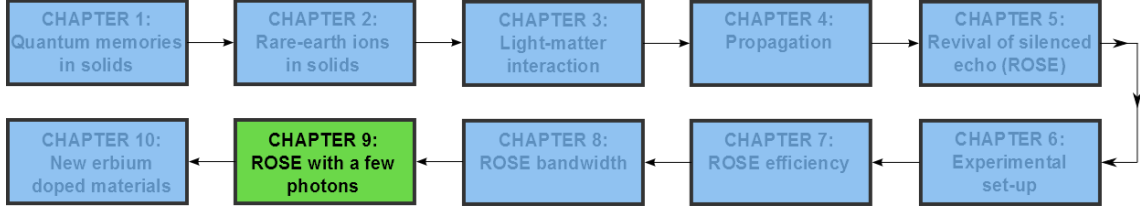
In the former sections I presented ROSE performance regarding its efficiency and bandwidth while storing classical pulses. As ROSE protocol is conceived for quantum storage, we performed a series of measurements to evaluate its noise. In this chapter I will present ROSE performance while storing a few photons.

9.1   Experimental set-up

The optical set-up used to perform single photon experiments is similar to the one presented in figure 6.2. We keep the two beams counterpropagating. The main difference between both set-up are the intensity of the input signal and the detection. Regarding the intensity, we used optical densities to attenuate the intensity of the signal before passing through the crystal. This procedure allowed us to have a few photons per pulse. The detection of a properly isolated output signal might be complicated. However, as the output was already collected in a single-mode fiber, we can easily plug the fiber into a fiber detector. The detector used for these experiments was an InGaAs/InP avalanche photodiode id220-FR-SMF from ID Quantique borrowed from the group of S. Tanzilli (LPMC, Nice), with a maximum efficiency of 20% at telecom wavelengths. The output of this detector is connected to a discriminator/counter SR400 from Stanford Research Systems. Finally, to acquire the data from a PC, we used a digitizer board P7888 from Fast ComTec that resolves in time the data taken from the photon counter. The measured dark counts rate is approximately 2.3 kHz, in agreement with the typical value provided by the manufacturer.

9.2   Spontaneous emission

When working at low photon level, the effect of imperfections in the single inversion, and particularly in the double inversion, are critical. As the rephasing pulses are applied in the same transition where the information is being stored, the noise due to spontaneous emission will be also detected and might overwhelm the echo. We studied the effect of the single inversion and the double inversion while applying one CHS pulse and two CHS pulses respectively. In figure 9.1(a) the number of counts as a function of time is shown when one CHS is applied, while in figure 9.1(b) the intensity when two CHS are applied to the system.
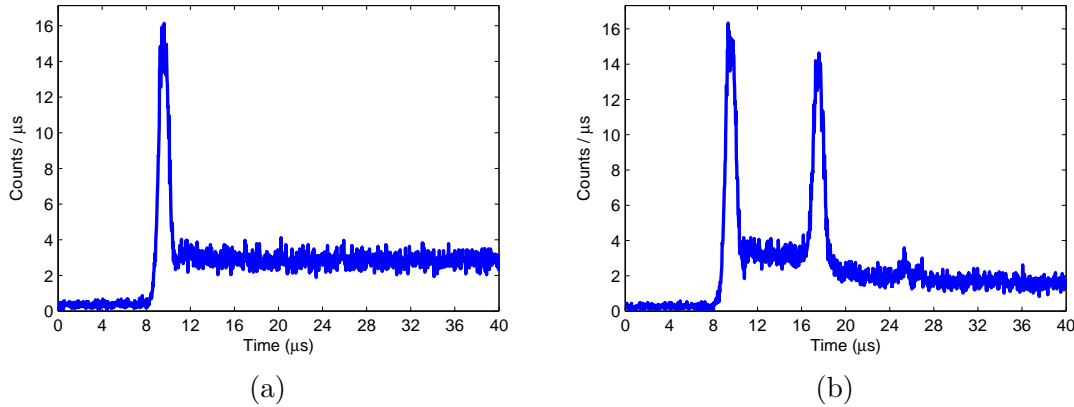

(a)   (b)

Figure 9.1: Number of counts as a function of time when applying in (a) one CHS and in (b) two CHS.

Although we worked in the counterpropagative configuration, it is possible to see a leakage of the CHS pulses in both figures. However, the number of counts is negligible respect to the total amounts of photons that these kind of pulses contain ($P_{CHS} \sim 10$ mW $\sim 10^{10}$ photons/μs). Additionally, in both figures we can see the spontaneous emission, which is greater after one CHS as the ions are mostly in the excited state. This source of noise will affect the fidelity of a quantum state. Although the ARP pulses have been extensively studied regarding its capacity to invert a medium, why a better inversion cannot performed still remains as an open question.

To better characterize the spontaneous emission, we studied the amplitude of the spontaneous emission as a function of the optical depth after one CHS and two CHS. The measurements are shown in figure 9.2. This effect was already studied by our group while performing experiments with a few photons in Tm^{3+}:YAG [70], where a similar behavior of the spontaneous emission was observed. We attribute this effect to the amplified spontaneous emission. This effect has been widely studied as a function of the thickness of a material (for example in [98]).
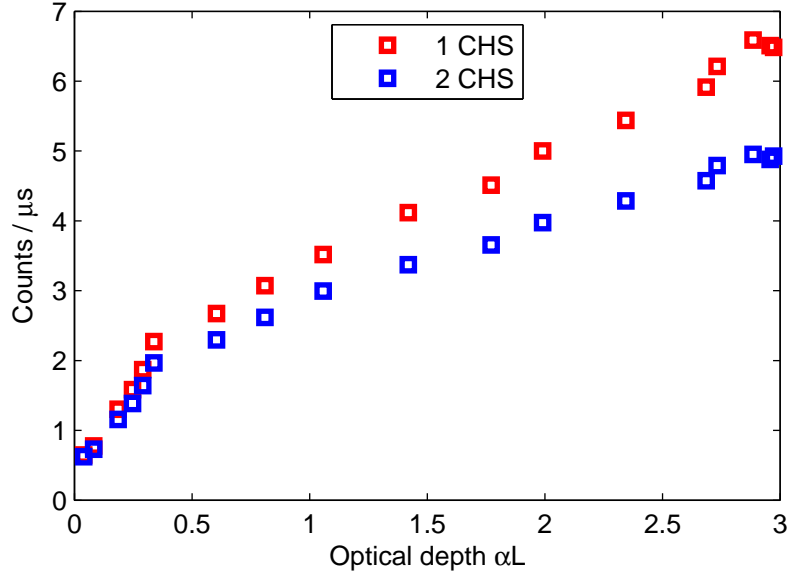
Figure 9.2: Amplitude of the spontaneous emission (SE) as a function of the optical depth αL. In red the SE amplitude after one CHS and in blue the SE amplitude after two CHS.

The measurements presented in figure 9.2 show two regimes [99, 100]. The first one is at low optical depth ($\alpha L < 0.5$), where the ASE increases exponentially with the optical depth. The second regime seems to be dominated by saturation effects. As explained by McGehee and coworkers [101], when the excitation length and gain is high enough, the amplified spontaneous emission is enough to start depopulating the excited state, giving place to saturation. During this regime, the ASE does not grow exponentially, but rather linearly. In terms of population, the effect of the amplified light traveling in the sample is to reduce the excited state population and, thus, the gain of the system. Further modeling is required for a proper quantitative comparison. On the other hand, the number of counts after one CHS is higher than after two CHS because of the higher excited state population after one CHS.

Although we would expect to measure a greater amount of photons per μs in the presence of ASE, because of the optical set-up most of the photons coming from this effect were not collected.

The gain region generated by the CHS pulses in the crystal is not collinear with respect to the signal beam:
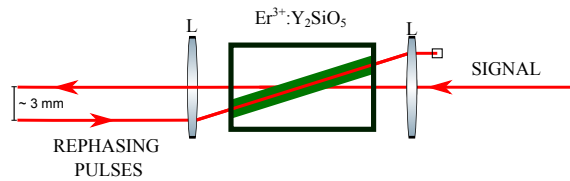
This is due to the separation between both signal and rephasing pulses beams, which

was around 3 mm. As the collection of the photons was optimized for the signal beam, not all the photons coming from the ASE effect were collected.

To fully characterize the dynamics of the spontaneous emission we verify the population lifetime (T_1) of the excited state for different the optical depths. The measurements are shown in figure 9.3.
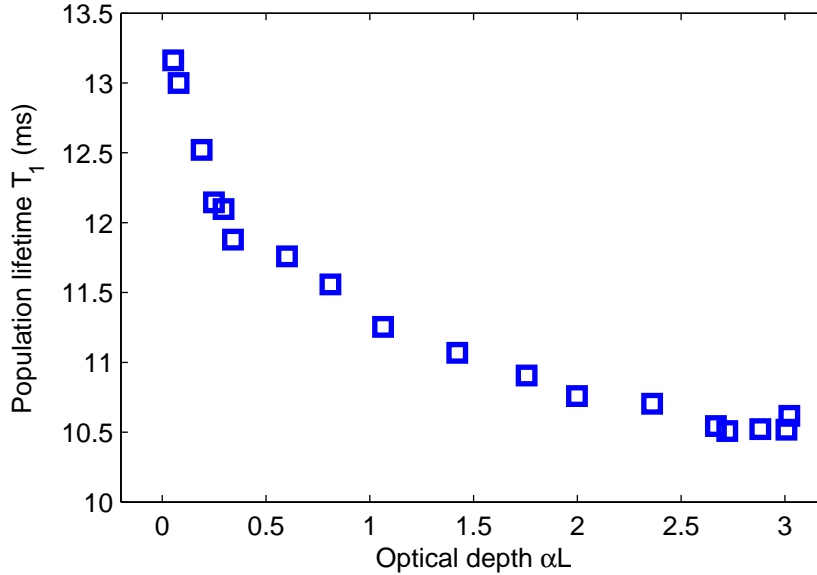

Figure 9.3: Population lifetime T_1 as a function of the optical depth αL.

This is something that, up to my knowledge, it has not been studied in detail in $Er^{3+}:Y_2SiO_5$. In [39], they showed that when the erbium concentration is increased, the population lifetime decays. In this case, it appears to be related to a quenching effect because of the Er-Er coupling as shown in [102]. We have previously highlighted the influence of ISD on the coherence time. Dipole-dipole electric or magnetic coupling between erbium ions has been characterized independently but may also affect the radiative lifetime. Further analysis is required.

Finally, we studied the amplitude of the spontaneous emission after two CHS as a function of the excited bandwidth BW. In principle, the increase in the spontaneous emission should be linear with the bandwidth, proportional to the number of excited ions. However, as shown in figure 9.4, both curves slightly saturate for a large excitation bandwidth. This behavior is qualitatively similar to the one presented in figure 9.2, where I analyzed the spontaneous emission as a function of the optical depth. Again further modeling of the ASE is required for a quantitative analysis. The measurements and analysis presented in this section are important to understand how the CHS pulses interact with the medium, and the characteristics of the noise. In the next section, I will present ROSE protocol for a few photons.
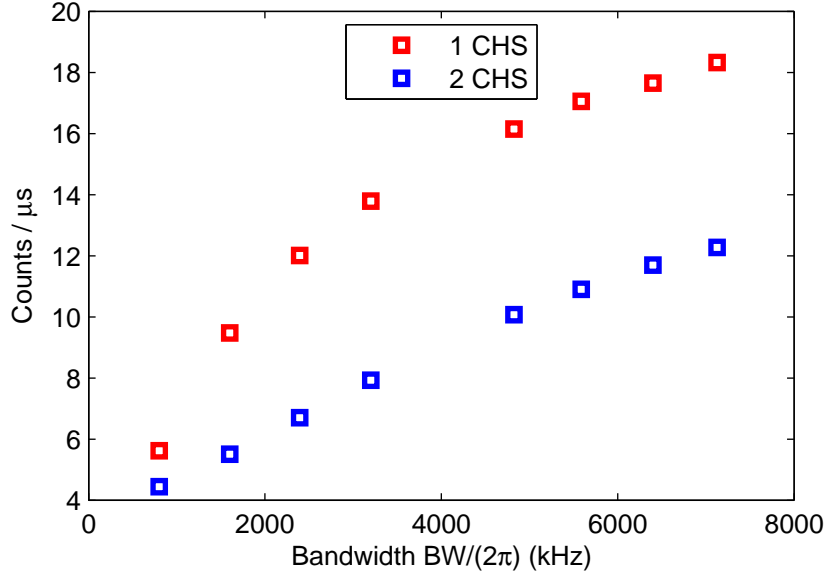
Figure 9.4: Amplitude of the spontaneous emission (SE) as a function of the bandwidth BW with a linear fitting.

9.3   Signal-to-noise ratio

We measured the signal-to-noise ratio for a bandwidth BW $= 2\pi \times 800$ kHz. With the optical densities, we were able to go down to 7.8 photons per pulse. As the noise from the spontaneous emission was important, we could not go down to only one photon per pulse. The efficiency of the protocol was calculated by taking the ratio between the area of the output mode and the input mode. The input pulse was measured by changing the magnetic field, thus shifting the absorption profile. In figure 9.5 the protocol without magnetic field (no absorption) is presented. The area under the red curve gives the input signal. In that case the area is of 7.8 photons.

We performed the experiment at a magnetic field of 3.3 T. In figure 9.6 the protocol is presented, in blue ROSE protocol with an input pulse while in green without an input pulse. Comparing this curve with figure 9.5, we see that most of the input pulse is actually absorbed by the crystal as expected for an optical depth of 1.9.

This measurement gives an efficiency of $\eta = 30\%$. This is below the maximum achieved while using strong input pulses. This is probably related to the noise coming from the spontaneous emission. However, the value obtained here shows that, even with a few photons, ROSE protocol presents a good performance in terms of efficiency. Regarding the noise levels, we took the integrated noise over the mode of the echo. In that case, the noise is 3.5 photons.
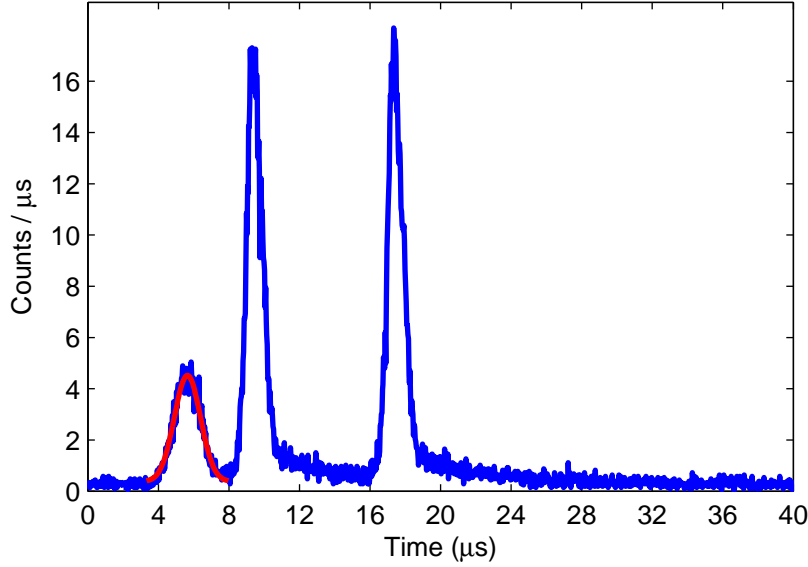
Figure 9.5: ROSE protocol without magnetic field (out of the absorption line). The input is composed of 7.8 photons.
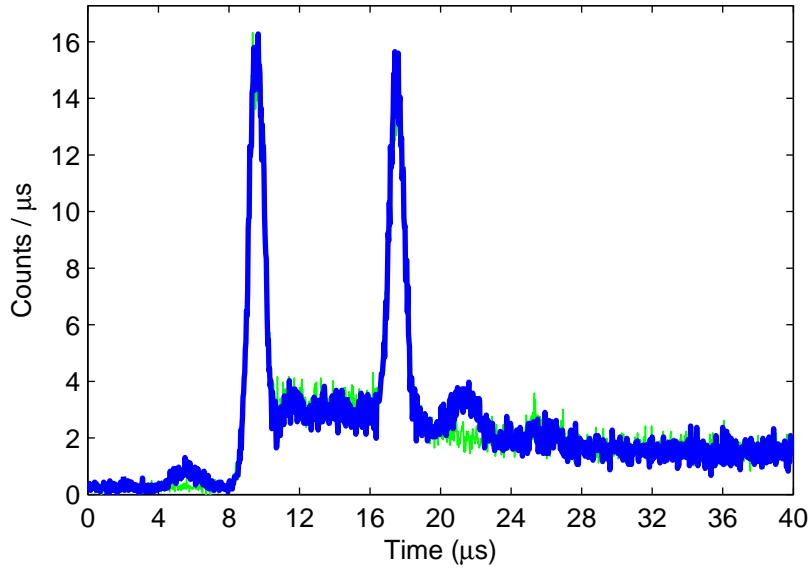

Figure 9.6: ROSE protocol sequence, in blue with an input of 7.8 photons while in green without an input pulse.

The figure of merit to evaluate the relevance of the noise is given by the signal-to-noise ratio (SNR). The SNR is calculated taking the ratio between the echo and the noise in the mode of the echo. We obtain a SNR= 0.7 for this experiment.

A lot has to be done to obtain a SNR much larger than one. As the spontaneous emission comes from the same transition used to store the information, spectral filtering is not an option. A better inversion efficiencies and a good understanding of the CHS pulses behavior are still required.

New erbium doped materials
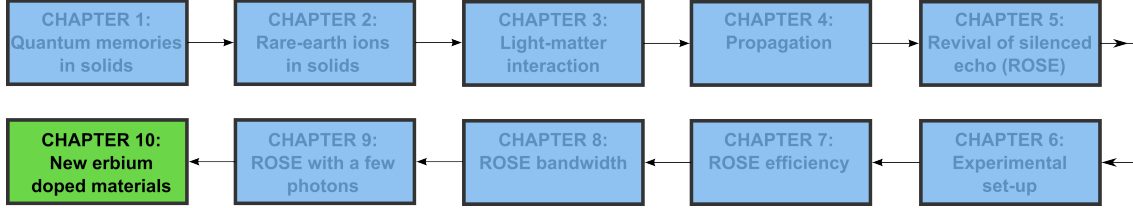
In this chapter I present a series of prospective measurements, performed on new doped materials, with an optical transition around 1.5 μm in the context of optical information processing. They are all doped with erbium, either codoped with another substitution ion or in a different host matrix. Large inhomogeneous linewidths, long coherence times and a large time-to-bandwidth product are desirable and analyzed in this chapter.

I will present the measurements performed in three crystals: $Er^{3+}:KYF_4$, $Er^{3+}+Ge^{4+}:Y_2SiO_5$ and $Er^{3+}+Sc^{3+}:Y_2SiO_5$.

10.1 $Er^{3+}:KYF_4$

As part of a collaboration with Professor Alberto Tonelli from University of Pisa and in the framework of CIPRIS, we studied a fluoride crystal doped with erbium. $Er^{3+}:KYF_4$ has been already studied as a candidate for solid-state lasers (see for example [103]). KYF_4 may exhibit a high degree of disorder that results in large inhomogeneous linewidths [104], something desirable in the context of optical information processing. However, this high disorder may have a negative effect on the coherent properties, that has to be evaluated. In this section I will present a set of preliminary results of a 5.2 x 5.0 x 4.9 mm^3 KYF_4 crystal doped with 200 ppm of erbium. This crystal was growth using the Czochralski method in the group of Pr. Tonelli. Fluorides, compared to oxides, present a lower melting temperature, which in the case of KYF_4 is 805°.

10.1.1 Inhomogeneous linewidth

Initially, we studied the spectrum of the crystal using a spectrum optical analyzer AQ6317B (Ando) to find the transition. In figure 10.1, the optical depth as a
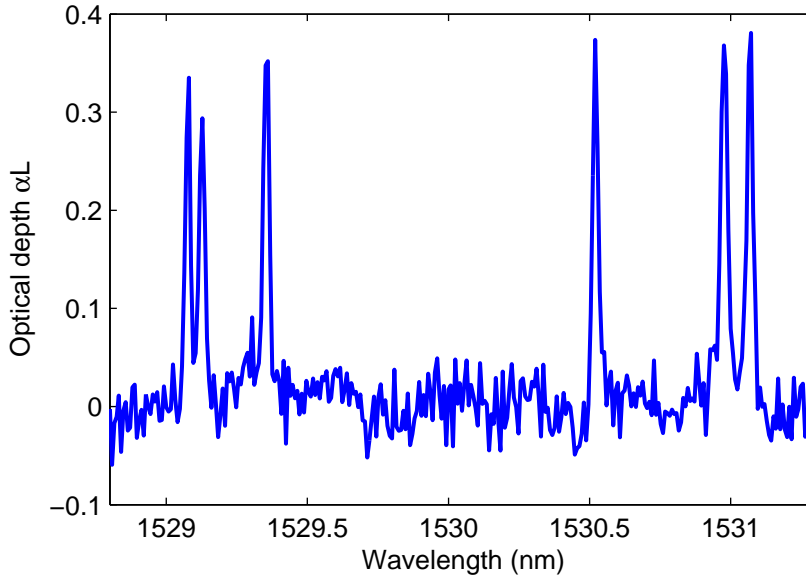
function of the wavelength is presented.

Figure 10.1: Optical spectrum at 2 K measured using the spectrum optical analyzer.

Although we were expecting to see one transition broader than $Er^{3+}:Y_2SiO_5$, figure 10.1 presents six different transitions, each one with an absorption around 0.3. Each transition corresponds to a different substitution site. The material is not disordered in that sense because the different substitution sites are well separated. For a disordered material, a broader transition covering typically 2 nm is expected.

Additionally, from this measurement we can estimate that the inhomogeneous linewidth for the different transitions are around 2 and 3 GHz, potentially limited by the resolution of the spectrum analyzer. Thus, we focused on one of the transitions using a tunable laser.

We picked one of the transitions and we measured the inhomogeneous linewidth by sweeping the laser. In figure 10.2, the absorption (in arbitrary units) as a function of the frequency without magnetic field and a temperature of 2.5 K. Using a Lorentzian fitting we obtain an inhomogeneous linewidth of $\Gamma_{inh} \approx 2$ GHz.

10.1.2 Coherence time

We studied the coherent properties of $Er^{3+}:KYF_4$ at low temperature (2.5 K) and a high magnetic field (3 T). As the absorption is quite low, and the homogeneous linewidth quite large, performing photon echo experiments is challenging. However, as explained in section 6.6, the hole width in the SHB technique is proportional to the coherence time. Thus, we measured the SHB width while changing the power of the burning beam.
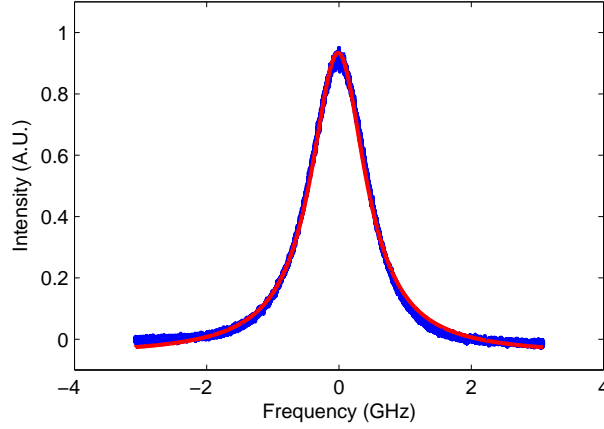
Figure 10.2: Absorption profile of one of the peaks from figure 10.1 at 2.5 K and without magnetic field.

In figure 10.3, the homogeneous linewidth as a function of the pumping power is presented. This measurement was performed at a temperature of 2.5 K and a magnetic field of 3 T.
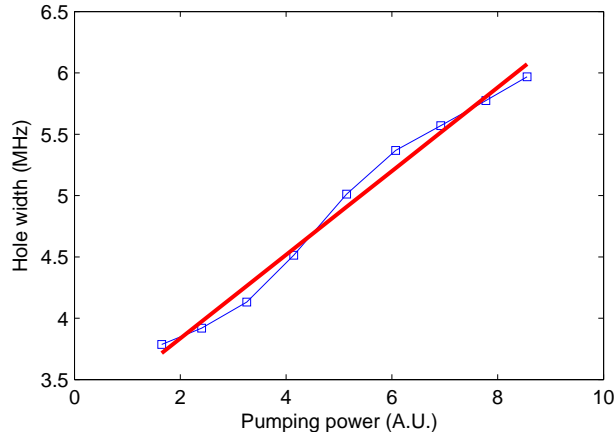
Figure 10.3: Homogeneous linewidth as a function of the pumping power.

From the linear fitting we can extract the homogeneous linewidth: $\Gamma_h \approx 1.6$ MHz. Compared to Er^{3+}:Y_2SiO_5, the homogeneous linewidth of Er^{3+}:KYF_4 is around 3 orders of magnitude larger, that represents a coherence time much shorter than 1 μs. Although this material has a larger inhomogeneous linewidth than Er^{3+}:Y_2SiO_5, the time-to-bandwidth-product is clearly less advantageous. This is a preliminary study and it might be interesting to go further. For example, a measure of the homogeneous linewidth as a function of the angle between magnetic field and one of the axes of the crystal might lead to a narrower homogeneous linewidth.

10.2 $Er^{3+}+Ge^{4+}:Y_2SiO_5$

As part of the collaborations with Philippe Goldner's group (ENSCP), we studied a Y_2SiO_5 crystal codoped with erbium (Er^{3+}) and germanium (Ge^{4+}). The germanium was added to increase the disorder in a controlled manner and, thus, the inhomogeneous linewidth but preserving the homogeneous linewidth. Codoping a material to increase its homogeneous linewidth has been already done, for example adding europium to $Er^{3+}:Y_2SiO_5$ [105].

The crystal used for the experiments had a dimension of 4.52 x 4.95 x 6.68 mm^3 and it was codoped with 50 ppm of erbium and 10000 ppm. The b axis was directed along the 4.95 mm side. The crystal was growth using the Czochralski method by the group of P. Goldner (ENSCP, Paris). The main difference with the fluoride presented in the former section is given by the melting temperature of Y_2SiO_5 , which is close to $2000°$.

10.2.1 Inhomogeneous linewidth

We measured first the inhomogeneous linewidth of the optical transition for different magnetic fields. These measurements were performed acquiring the transmission for different wavelengths while using the temperature tuning of the Koheras laser. In figure 10.4 the optical depth αL as a function of the frequency with a Lorentzian fitting is shown. From the fitting we obtain an inhomogeneous linewidth of $\Gamma_{inh} = 560$ MHz, that represents a larger broadening that the one measured for the crystal doped only with 50 ppm ($\Gamma_{inh} = 365$ MHz).
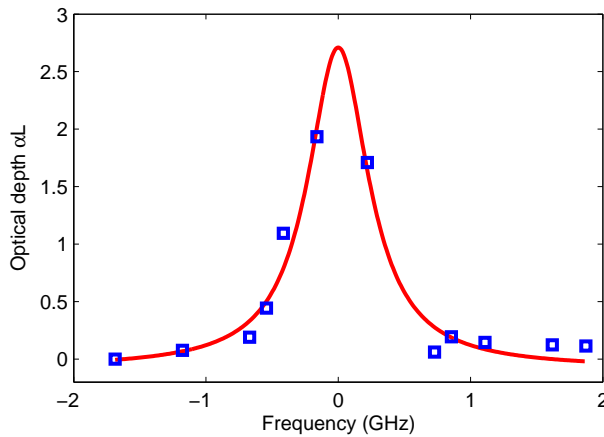

Figure 10.4: Absorption profile without magnetic field. In red a Lorentzian fitting, which gives a linewidth $\Gamma_{inh} = 560$ MHz.

When increasing the magnetic field, we observed that the inhomogeneous linewidth increased. In figure 10.5, the absorption profile for a magnetic field of

0.9 T is shown. From the Lorentzian fitting we obtain a linewidth $\Gamma_{inh} = 1.2$ GHz, almost two times what it was measured without magnetic field. This effect probably comes from the contribution of inequivalent magnetic sites, that appears when the magnetic field is not exactly at 90° respect to the b axis of the crystal.
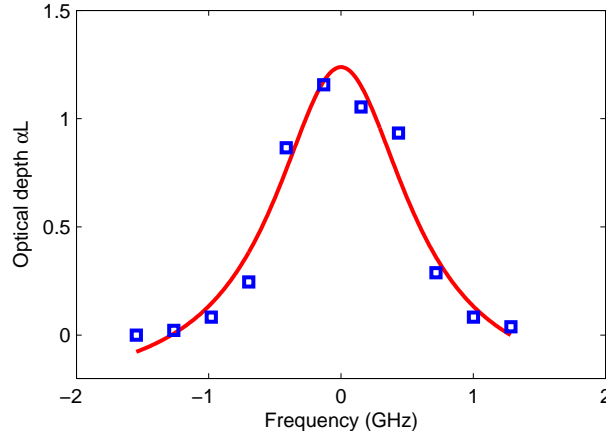

Figure 10.5: Absorption profile for a magnetic field of 0.9 T. In red a Lorentzian fitting, which gives a linewidth $\Gamma_{inh} = 1.2$ GHz.

This is certainly verified when the magnetic field is increased even more. For a magnetic field of 2.9 T and 3.5 T, we can distinguish both sites (see figure 10.6).

(a)   (b)
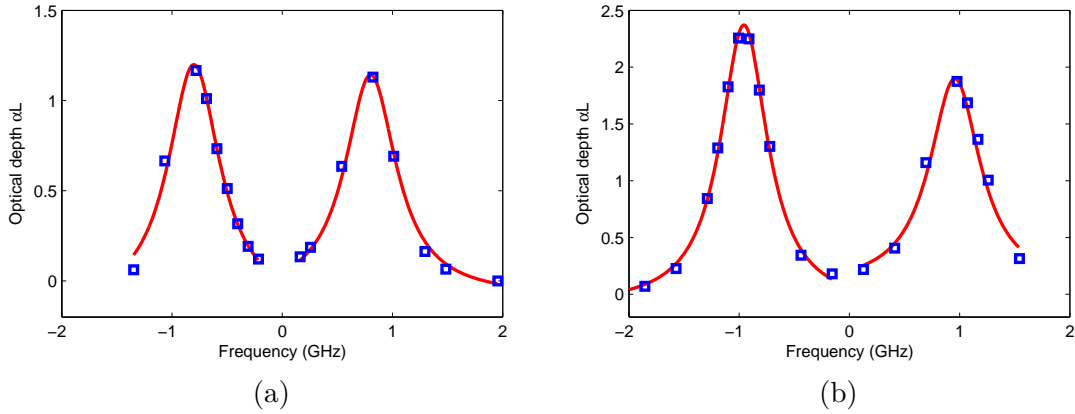
Figure 10.6: Absorption profile for a magnetic field of 2.9 T in (a) and 3.5 T in (b). In (a) both peaks have a inhomogeneous linewidth of $\Gamma_{inh} = 570$ MHz while, in (b), $\Gamma_{inh} = 520$ MHz for the first Lorentzian and $\Gamma_{inh} = 560$ MHz for the second Lorentzian.

From the fittings we obtain an inhomogeneous linewidth of around 550 MHz for all peaks. This is consistent with the measurements taken without any magnetic field.

Although the inhomogeneous linewidth measured for $Er^{3+}+Ge^{4+}:Y_2SiO_5$ is larger than for $Er^{3+}:Y_2SiO_5$ (see figure 6.5), they have the same order of magnitude. Thus, codoping $Er^{3+}:Y_2SiO_5$ with Ge^{4+} does not add as much disorder apparently.

10.2.2 Coherence time

We studied the coherence properties of $Er^{3+}+Ge^{4+}:Y_2SiO_5$ using the two-pulse photon echo. In figure 10.7 the logarithm of the echo amplitude as a function of t_{12} for a magnetic field of 3.7 T is presented.

Figure 10.7: Natural logarithm of the echo amplitude as a function of t_{23} at a magnetic field of 3.7 T. The linear fitting gives a coherence time of $T_2 = 360$ μs.

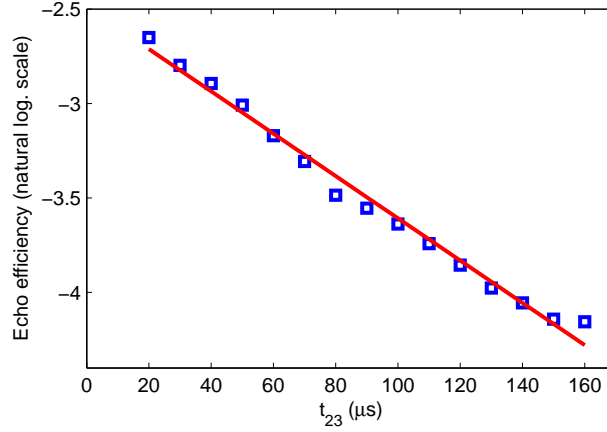From the linear fitting we obtain a coherence time of $T_2 = 360$ μs. On the other hand, the $Er^{3+}:Y_2SiO_5$ crystal shows a coherence time of around 700 μs for the same orientation. This means that the germanium slightly modifies the coherence properties of the transition.

The absorption profiles presented in the last section and the coherence properties showed in this section demonstrate that the germanium does not modify the properties of $Er^{3+}:Y_2SiO_5$. This could be related to the growing process of the crystal. Adding germanium is not an easy task to achieve and most of it might have been evaporated during the melting process. The exact amount of germanium contained in the crystal has to be verified.

10.3 $Er^{3+}+Sc^{3+}:Y_2SiO_5$

In addition to the $Er^{3+}+Ge^{4+}:Y_2SiO_5$ crystal, we also analyzed the performance of a Y_2SiO_5 crystal codoped with 30 ppm of erbium (Er^{3+}) and 10000 ppm of scandium (Sc^{3+}) growth by Philippe Goldner's group (ENSCP). As in the case of $Er^{3+}+Ge^{4+}:Y_2SiO_5$, we were expecting to have a larger inhomogeneous linewidth because of the disorder added by the scandium [106]. Scandium was chosen as a co-dopant because it is a trivalent ion, therefore, it substitutes the yttrium ions without charges compensation (as with erbium), avoiding any issues related to charge

compensation. Furthermore, it has an atomic radius similar to the erbium, adding disorder to the crystal. Additionally it does not have electronic spin and transitions in the IR-visible, which could affect the coherence properties of the crystal.

10.3.1   Inhomogeneous linewidth

To measure the inhomogeneous linewidth in this sample we used an optical spectrum analyzer well adapted for a large broadening. The erbium concentration is rather low, thus, if the broadening is too large, the profile will present low peak absorption. In figure 10.8, the optical depth as a function of the frequency without magnetic field is shown.
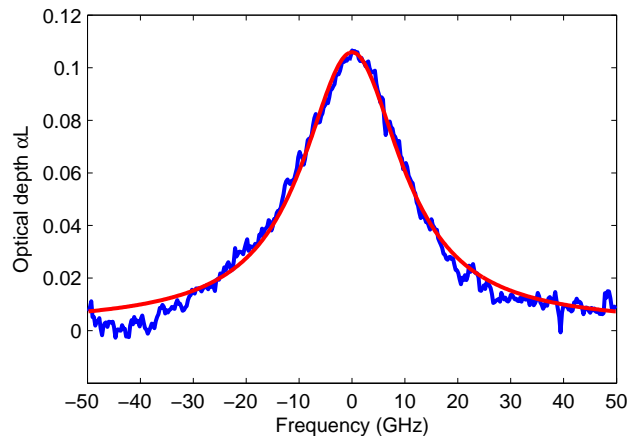
Figure 10.8: Absorption profile without magnetic field. In red a Lorentzian fitting, which gives a linewidth $\Gamma_{inh} = 23$ GHz.

The measurements presented a modulation due to an optical etalon Fabry-Perot (effect of the optical elements) that we artificially removed. The baseline is still slightly biased. From the Lorentzian fitting in figure 10.8 we obtain an inhomogeneous linewidth of $\Gamma_{inh} = 23$ GHz. This 50 times greater than the one for in $Er^{3+}:Y_2SiO_5$.

We also measured the inhomogeneous linewidth with a magnetic field of 1 T and 2 T as for $Er^{3+}+Ge^{4+}:Y_2SiO_5$. In principle, we should not see any changes, like the splitting of the inequivalent magnetic sites, because of the much larger broadening. In figure 10.9 the inhomogeneous linewidth for a magnetic field of 1 T and 2 T are presented. For 1 T, the inhomogeneous broadening is $\Gamma_{inh} \approx 25$ GHz, while for 2 T $\Gamma_{inh} \approx 32$ GHz. No evidence of resolved inequivalent magnetic sites is observed.

(a)   (b)
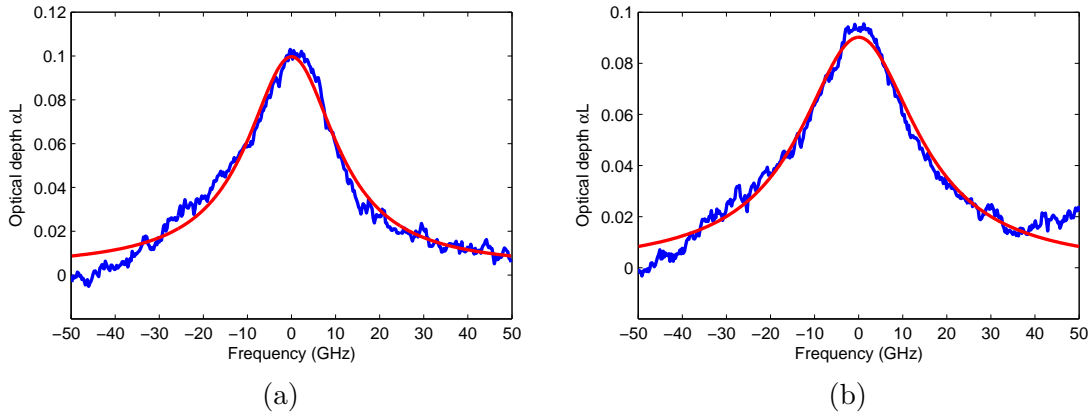
Figure 10.9: Absorption profile for a magnetic field of 1 T in (a) and 2 T in (b). The Lorentzian fittings give an inhomogeneous linewidth of $\Gamma_{inh} = 25$ GHz and $\Gamma_{inh} = 32$ GHz for (a) and (b) respectively.

10.3.2   Coherence time

In the former section, I showed the encouraging measurements of the inhomogeneous linewidth. We still need to look at the coherence properties and evaluate the time-bandwidth product. The maximum optical depth measured for this crystal was of αL= 0.1, thus, performing a photon echo experiment is quite challenging.

In order to increase the absorption and, thus, the efficiency of a photon echo experiment, we glued a gold mirror to one of the faces of the crystal. We double the absorption by this double pass configuration. In figure 10.10 the coherence time as a function of the magnetic field is shown.
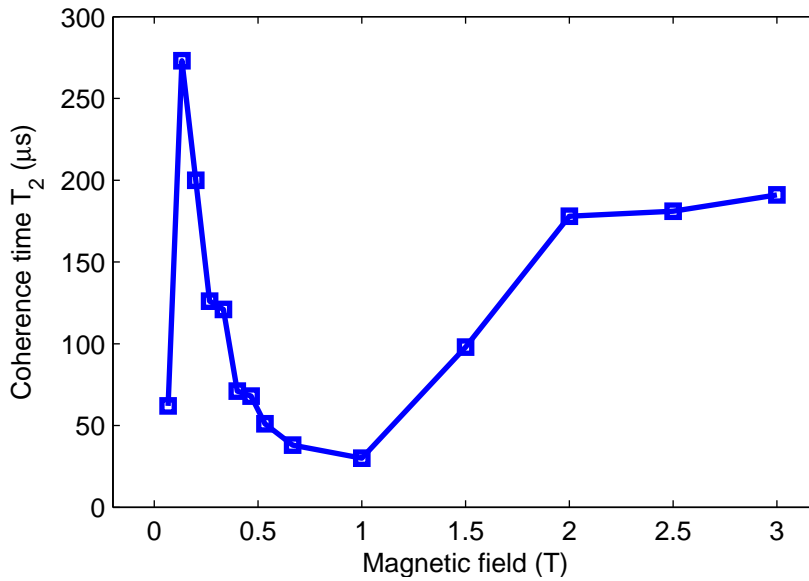
Figure 10.10: Coherence time T_2 as a function of the magnetic field.

The coherence time was measured using the standard two-pulse photon echo and the magnetic field was varied from 0.07 T to 3 T.

This measurement shows a maximum coherence time of $T_2 = 173\,\mu$s for a magnetic field of 0.13 T. Although these results are strange, we found the similar behavior for the Y_2SiO_5 crystal doped with 50 ppm of erbium [107]. At low magnetic fields, there is a region where it might be a compensation of different interactions that gives place to a higher coherence time. The measurements presented here are a preliminary study and more detailed experiments will be performed in the near future to confirm this interesting behavior of the coherence time.

The coherence times measured for $Er^{3+}+Sc^{3+}{:}Y_2SiO_5$ are similar to those measured for $Er^{3+}{:}Y_2SiO_5$. However, the inhomogeneous linewidth for the crystal codoped with scandium is 50 times larger. This means that the multiplexing capacity of the crystal with scandium is 50 larger, which represents an interesting and useful improvement of the optical processing capabilities with respect to the crystal doped only with erbium. In the future, it will be interesting to test crystals codoped with scandium and a higher concentration of erbium to increase the optical absorption of the transition and see if the coherence properties are maintained.

Conclusion

The development of an efficient quantum memory at telecom wavelengths is an important challenge to improve several quantum applications. Quantum memories have been shown transcendental to improve the capabilities of quantum processing and quantum communication. In long distance quantum communication, for example, quantum memories with a high multiplexing capacity are essential to extend the communication length of quantum states. Certain features are expected for a quantum memory: high efficiency, high multiplexing capacity and long storage times. Furthermore, a quantum memory that works at telecom wavelength, where the optical fiber losses are minimized, would allow to improve the quantum communications.

In this thesis, I have presented the performance of a storage protocol, called revival of silenced echo (ROSE), set up to be used at both classical and quantum regime. The measurements were performed in Er^{3+}:Y_2SiO_5, a crystal that has a transition in the C-band of the telecom spectrum. This region needs to be exploited to improve the quantum communication field.

Using ROSE protocol, an efficiency of 40% at classical regime for an excited bandwidth of 800 kHz for a storage time of 16 μs was shown. The optical set-up used in this work is limited to a maximum efficiency of 54%. A way to increase the 40% efficiency might be done by improving the double inversion efficiency, which was approximately 80% in this work. Inversion efficiencies over 90% have been reported in the literature. The efficiency reported in this work, and the possibility of improving it, demonstrates why ROSE protocol deserves to be further studied as a potential quantum memory.

Additionally, the efficiency was studied while increasing the bandwidth. ROSE protocol can access to the whole inhomogeneous linewidth to store information, which represents a huge advantage against other protocols. However, as presented in this work, when the bandwidth of the protocol is increased the interaction between erbium ions induces extra dephasing, called instantaneous spectral diffusion (ISD), which goes in detriment of the protocol efficiency. I have presented how ISD affects the coherence time for two different orientation of the crystal with respect to the external magnetic field. An ISD factor $\kappa = 0.88s^{-1}$ kHz^{-1} for an αL = 3.4 for a magnetic field making an angle of 135° with respect to D_1 and $\kappa = 0.48s^{-1}$ kHz^{-1}

for an $\alpha L = 1.6$ for a magnetic field making an angle of $160°$ with respect to D_1 were reported.

To analyze ISD, a microscopical model to estimate it from experimental values was laid out. The agreement between the theory and the experiments was rather good. Finally, I have presented the different features of a memory while including ISD and how to optimize ROSE performance. The magnetic field should be set making an angle between $120°$ and $180°$ with respect to the axis D_1 of the crystal to minimize ISD. Furthermore, I have shown that the optical depth of the system has to be changed to maximize ROSE efficiency depending on the bandwidth of the protocol.

ISD is an interaction to be considered in any anisotropic materials regarding their magnetic or electric moments. A possible solution to reduce the effect of ISD is going to lower erbium concentration. As ISD scales with the distance between erbium ions, reducing the density of ions in the crystal should reduce the extra dephasing. In this work I have shown the performance for a crystal doped with 50 ppm of erbium. In the future, different crystal with lower concentrations will be tested.

A series of measurements performed with a few photons were presented. ROSE protocol is fundamentally adapted to be used as a quantum memory. To evaluate its performance I have shown the spontaneous emission after one and two rephasing pulses. The presence of spontaneous emission after two rephasing pulses demonstrates the difficulties in achieving an efficient double inversion of the media meaning a proper return to the ground state. Additionally, the spontaneous emission as a function of the absorption of the system is reported. When the absorption of the system is increased, the spontaneous emission increases as more ions are being excited. This have been demonstrated, however I have also shown that from a certain absorption, the system saturates because of the amplified spontaneous emission (ASE). I have reported a substantial change of the population lifetime where the absorption is increased and that the ASE does not really growth exponentially as expected. A proper quantitative modeling is required to fully describe the dynamics in the ASE regime.

Finally, I have presented the performance of ROSE protocol while storing 7.8 photons per pulse. An efficiency of 30% was measured for a storage time of 16 μs for an 800 kHz bandwidth, and a 0.7 signal-to-noise ratio (SNR) was measured. This represents a rather low value, however, improving the double inversion efficiency can lead to a higher SNR. The atoms that remains in the excited state after the double inversion of the media, performed while using ROSE protocol, decay and emit photons that will be overlapped with the echo. Furthermore, if the optical depth

is high enough, the spontaneous emission might be amplified leading to amplified spontaneous emission.

Finally, a series of measurements were performed on new doped materials with a transition at 1.5 μm to test their capabilities in the frame of optical processing. The crystals tested were $Er^{3+}:KYF_4$, $Er^{3+}+Ge^{4+}:Y_2SiO_5$ and $Er^{3+}+Sc^{3+}:Y_2SiO_5$. Looking for materials with larger inhomogeneous linewidth and good coherence properties compared to $Er^{3+}:Y_2SiO_5$, the inhomogeneous linewidth and homogeneous linewidth (or coherence time) were reported in those materials. The first material has a different host matrix: KYF_4. I have reported a series of transitions at 1.5 μm, showing an inhomogeneous linewidth of 2 GHz in one of those transitions, and similar for the others. Although the linewidth is larger than the one for $Er^{3+}:Y_2SiO_5$, the homogeneous linewidth is much larger as well. Thus, the coherence properties are not well preserved and this material does not represent an improvement with respect to Y_2SiO_5. For the materials with a Y_2SiO_5 host matrix, the results are rather different. In the case of $Er^{3+}+Ge^{4+}:Y_2SiO_5$, the measurements presented in this work show a similar performance with respect to the crystal doped only with erbium. The presence of germanium in the crystal is questionable because of its volatility during the growth process. However, $Er^{3+}+Sc^{3+}:Y_2SiO_5$ performance is quite promising. A 23 GHz inhomogeneous linewidth was measured and a coherence time close to 200 μs was reported. This represents an increase of approximately 50 times of the multiplexing capacity with respect to $Er^{3+}:Y_2SiO_5$. Searching for new materials doped with rare earth is important to improve the performance of the quantum memories as well as the processing capabilities of the crystals. The crystal codoped with Er^{3+} and Sc^{3+} presents an enhancement of the processing qualities of the crystal doped only with Er^{3+}. Further studies will be performed in this material as well as in new materials.

Bibliography

[1] R. P. Feynman. Simulating physics with computers. *International Journal of Theoretical Physics*, 21(6-7):467–488, 1982.
(Cited on page 3.)

[2] G. E. Moore. Cramming more components onto integrated circuits. *Proceedings of the IEEE*, 86(1):82–85, 1998.
(Cited on page 3.)

[3] P. W. Shor. Polynomial-time algorithms for prime factorization and discrete logarithms on a quantum computer. *SIAM J. Comput.*, 26(5):1484–1509, 1997.
(Cited on page 3.)

[4] E. Knill, R. Laflamme, and G. J. Milburn. A scheme for efficient quantum computation with linear optics. *Nature*, 409:46–52, 2001.
(Cited on page 4.)

[5] F. Bussières, N. Sangouard, M. Afzelius, H. de Riedmatten, C. Simon, and W. Tittel. Prospective applications of optical quantum memories. *Journal of Modern Optics*, 60(18):1519 – 1537, 2013.
(Cited on page 4.)

[6] H.-J. Briegel, W. Dür, J. I. Cirac, and P. Zoller. Quantum repeaters: The role of imperfect local operations in quantum communication. *Phys. Rev. Lett.*, 81:5932–5935, 1998.
(Cited on page 4.)

[7] O. A. Collins, S. D. Jenkins, A. Kuzmich, and T. A. B. Kennedy. Multiplexed memory-insensitive quantum repeaters. *Phys. Rev. Lett.*, 98:060502, 2007.
(Cited on page 5.)

[8] N. Sangouard, C. Simon, H. de Riedmatten, and N. Gisin. Quantum repeaters based on atomic ensembles and linear optics. *Rev. Mod. Phys.*, 83:33–80, 2011.
(Cited on page 5.)

[9] X.-C. Yao, T.-X. Wang, P. Xu, H. Lu, G.-S. Pan, C.-Z. Peng X.-H. Bao, C.-Y. Lu, Y.-A. Chen, and J.-W. Pan. Observation of eight-photon entanglement. *Nature Photonics*, 6:225–228, 2012.
(Cited on page 5.)

[10] J. Nunn, N. K. Langford, W. S. Kolthammer, T. F. M. Champion, M. R. Sprague, P. S. Michelberger, X.-M. Jin, D. G. England, and I. A. Walmsley. Enhancing multiphoton rates with quantum memories. *Phys. Rev. Lett.*, 110:133601, 2013.
(Cited on page 5.)

[11] C. Simon, M. Afzelius, J. Appel, A. B. de la Giroday, S. J. Dewhurst, N. Gisin, C. Hu, F. Jelezko, S. Kröll, J. H. Müller, J. Nunn, E. Polzik, J. Rarity, H. de Riedmatten, W. Rosenfeld, A. J. Shields, N. Sköld, R. M. Stevenson, R. Thew, I. Walmsley, M. Weber, H. Weinfurter, J. Wrachtrup, and R. J. Young. Quantum memories. *Eur. Phys. J. D*, 58(1):1–22, 2010.
(Cited on page 5.)

[12] T. Golubeva, Y. Golubev, O. Mishina, A. Bramati, J. Laurat, and E. Giacobino. High-speed spatially multimode atomic memory. *Phys. Rev. A*, 83:053810, 2011.
(Cited on page 7.)

[13] C. Simon, H. de Riedmatten, and M. Afzelius. Temporally multiplexed quantum repeaters with atomic gases. *Phys. Rev. A*, 82:010304, 2010.
(Cited on page 7.)

[14] C. Simon, H. de Riedmatten, M. Afzelius, N. Sangouard, H. Zbinden, and N. Gisin. Quantum repeaters with photon pair sources and multimode memories. *Phys. Rev. Lett.*, 98:190503, 2007.
(Cited on page 7.)

[15] N. Sinclair, E. Saglamyurek, H. Mallahzadeh, J. A. Slater, M. George, R. Ricken, M. P. Hedges, D. Oblak, C. Simon, W. Sohler, and W. Tittel. Spectral multiplexing for scalable quantum photonics using an atomic frequency comb quantum memory and feed-forward control. *Phys. Rev. Lett.*, 113:053603, 2014.
(Cited on page 7.)

[16] A. I. Lvovsky, B. C. Sanders, and W. Tittel. Optical quantum memory. *Nature Photonics*, 3:706–714, 2009.
(Cited on page 7.)

[17] M. Afzelius, C. Simon, H. de Riedmatten, and N. Gisin. Multimode quantum memory based on atomic frequency combs. *Phys. Rev. A*, 79:052329, 2009.
(Cited on page 7.)

[18] B. Lauritzen, J. Minář, H. de Riedmatten, M. Afzelius, and N. Gisin. Approaches for a quantum memory at telecommunication wavelengths. *Phys. Rev. A*, 83:012318, 2011.
(Cited on pages 8 and 71.)

[19] E. Saglamyurek, J. Jin, V. B. Verma, M. D. Shaw, F. Marsili, S. W. Nam, D. Oblak, and W. Tittel. Quantum storage of entangled telecom-wavelength photons in an erbium-doped optical fibre. *Nature Photonics*, 9:83–87, 2015.
(Cited on page 9.)

[20] B. Kraus, W. Tittel, N. Gisin, M. Nilsson, S. Kröll, and J. I. Cirac. Quantum memory for nonstationary light fields based on controlled reversible inhomogeneous broadening. *Phys. Rev. A*, 73:020302, 2006.
(Cited on page 9.)

[21] A. L. Alexander, J. J. Longdell, M. J. Sellars, and N. B. Manson. Photon echoes produced by switching electric fields. *Phys. Rev. Lett.*, 96:043602, 2006.
(Cited on page 9.)

[22] G. Hétet, J. J. Longdell, A. L. Alexander, P. K. Lam, and M. J. Sellars. Electro-optic quantum memory for light using two-level atoms. *Phys. Rev. Lett.*, 100:023601, 2008.
(Cited on page 9.)

[23] B. Lauritzen, J. Minář, de Riedmatten H., M. Afzelius, N. Sangouard, C. Simon, and N. Gisin. Telecommunication-wavelength solid-state memory at the single photon level. *Phys. Rev. Lett.*, 104:080502, 2010.
(Cited on page 9.)

[24] V. Damon, M. Bonarota, A. Louchet-Chauvet, T. Chanelière, and J-L. Le Gouët. Revival of silenced echo and quantum memory for light. *New Journal of Physics*, 13(9):093031, 2011.
(Cited on pages 10, 11, 59, 63, and 67.)

[25] M. Bonarota, J. Dajczgewand, A. Louchet-Chauvet, J-L. Le Gouët, and T. Chanelière. Photon echo with a few photons in two-level atoms. *Laser Phys.*, 24(9):094003, 2014.
(Cited on pages 11 and 151.)

[26] G. Liu and B. Jacquier. *Spectroscopic Properties of Rare Earths in Optical Materials*, volume 83. Springer, 2005.
(Cited on pages 13 and 31.)

[27] A. J. Freeman and R. E. Watson. Theoretical investigation of some magnetic and spectroscopic properties of rare-earth ions. *Phys. Rev.*, 127:2058–2075, 1962.
(Cited on pages 13 and 14.)

[28] G. H. Dieke and H. M. Crosswhite. The spectra of the doubly and triply ionized rare earths. *Applied Optics*, 2(7):675–686, 1963.
(Cited on pages 14 and 15.)

[29] R.J. Mears, L. Reekie, I.M. Jauncey, and D.N. Payne. Low-noise erbium-doped fibre amplifier operating at 1.54 μm. *Electronics Letters*, 23:1026–1028, 1987.
(Cited on page 14.)

[30] E. Desurvire, D. Bayart, B. Desthieux, and S. Bigo. *Erbium-Doped Fiber Amplifiers, Device and System Developments*. Wiley, 2002.
(Cited on page 14.)

[31] R. Moncorge. Rare earth materials in optical storage and data processing applications. In *Spectroscopic Properties of Rare Earths in Optical Materials by G. Liu and B. Jacquier*, volume 83, chapter 7. Springer, 2005.
(Cited on page 14.)

[32] R. W. Equall, Y. Sun, R. L. Cone, and R. M. Macfarlane. Ultraslow optical dephasing in Eu^{3+}:Y_2SiO_5. *Phys. Rev. Lett.*, 72:2179–2182, 1994.
(Cited on page 14.)

[33] B. A. Maksimov, Y. A. Kharitonov, V. V. Ilyukhin, and N. V. Belov. Crystal structure of Y-Oxysilicate $Y_2(SiO_4)O$. *Soviet Physics-Doklady*, 13:1188–1190, 1969.
(Cited on page 14.)

[34] Y. Sun, T. Böttger, C. W. Thiel, and R. L. Cone. Magnetic g tensors for the $^4I_{15/2}$ and $^4I_{13/2}$ states of Er^{3+}:Y_2SiO_5. *Phys. Rev. B*, 77:085124, 2008.
(Cited on pages 15, 21, 22, and 106.)

[35] G. Liu. Electronic energy level structure. In *Spectroscopic Properties of Rare Earths in Optical Materials by G. Liu and B. Jacquier*, volume 83, chapter 1.

Springer, 2005.
(Cited on pages 16 and 23.)

[36] T. Böttger, Y. Sun, C. W. Thiel, and R. L. Cone. Spectroscopy and dynamics of Er^{3+}:Y_2SiO_5 at 1.5 μm. *Phys. Rev. B*, 74:075107, 2006.
(Cited on pages 18, 23, and 25.)

[37] H. K. Kramers. Théorie générale de la rotation paramagnétique dans les cristaux. *Proceedings Koninklijke Akademie van Wetenschappen*, 33:959–972, 1930.
(Cited on page 18.)

[38] M. J. Klein. On a degeneracy theorem of kramers. *American Journal of Physics*, 20(2):65–71, 1952.
(Cited on page 18.)

[39] C. Li, C. Wyon, and R. Moncorge. Spectroscopic properties and fluorescence dynamics of Er^{3+} and Yb^{3+} in Y_2SiO_5. *IEEE Journal of Quantum Electronics*, 28(4):1209–1221, 1992.
(Cited on pages 18, 19, and 118.)

[40] R. M. Macfarlane and R. M. Shelby. Coherent transient and holeburning spectroscopy of rare earth ions. In *Spectroscopy of solids containing rare earth ions by A. A. Kaplyanskii and R.M. Macfarlane*, chapter 3. North-Holland, 1987.
(Cited on page 20.)

[41] A. Abragam and B. Bleaney. *Electronic Paramagnetic Resonance of Transition Ions*. Oxford, 1970.
(Cited on pages 20 and 35.)

[42] T. Böttger, Y. Sun, C. W. Thiel, and R. L. Cone. Material optimization of Er^{3+}:Y_2SiO_5 at 1.5 μm for optical processing, memory, and laser frequency stabilization applications. *Proceddings SPIE*, 4988:51–61, 2003.
(Cited on page 23.)

[43] R. M. Macfarlane, T. L. Harris, Y. Sun, R. L. Cone, and R. W. Equall. Measurement of photon echoes in Er^{3+}:Y_2SiO_5 at 1.5 μm with a diode laser and an amplifier. *Optics Letters*, 22(12):871–873, 1997.
(Cited on page 23.)

[44] T. Böttger, C. W. Thiel, Y. Sun, and R. L. Cone. Optical decoherence and spectral diffusion at 1.5 μm in Er^{3+}:Y_2SiO_5 versus magnetic field, temperature, and Er^{3+} concentration. *Phys. Rev. B*, 73:075101, 2006. (Cited on pages 23 and 85.)

[45] T. Böttger, C. W. Thiel, R. L. Cone, and Y. Sun. Effects of magnetic field orientation on optical decoherence in Er^{3+}:Y_2SiO_5. *Phys. Rev. B*, 79:115104, 2009. (Cited on pages 23, 24, 101, 110, and 111.)

[46] O. Guillot-Noël, H. Vezin, Ph. Goldner, F. Beaudou, J. Vincent, J. Lejay, and I. Lorgeré. Direct observation of rare-earth-host interactions in Er^{3+}:Y_2SiO_5. *Phys. Rev. B*, 76:180408, 2007. (Cited on page 24.)

[47] L. Allen and J. H. Eberly. *Optical Resonance and Two-Level Atoms.* Dover, 1987. (Cited on pages 25 and 38.)

[48] R. M. Macfarlane. Inhomogeneous broadening of spectral lines in doped insulators. *Journal of Luminescence*, 45(1–6):1 – 5, 1990. (Cited on page 25.)

[49] W. B. Mims, K. Nassau, and J. D. McGee. Spectral diffusion in electron resonance lines. *Phys. Rev.*, 123:2059–2069, 1961. (Cited on page 26.)

[50] J. R. Klauder and P. W. Anderson. Spectral diffusion decay in spin resonance experiments. *Phys. Rev.*, 125:912–932, 1962. (Cited on page 26.)

[51] A. M. Stoneham. Shapes of inhomogeneously broadened resonance lines in solids. *Reviews of Modern Physics*, 41:82–108, 1969. (Cited on page 26.)

[52] W. B. Mims. Electron spin echoes. In *Electron paramagnetic resonance by S. Geschwind*, chapter 4. Plenum Press, 1972. (Cited on page 26.)

[53] G. K. Liu and R. L. Cone. Laser-induced instantaneous spectral diffusion in Tb^{3+} compounds as observed in photon-echo experiments. *Phys. Rev. B*, 41:6193–6200, 1990. (Cited on pages 27, 100, and 102.)

[54] G. K. Liu, R. L. Cone, M. F. Joubert, B. Jacquier, and J. L. Skinner. Energy transfer and instantaneous spectral diffusion processes in Tb^{3+} compounds as probed in photon echo experiments. *Journal of Luminescence*, 45(1–6):387–391, 1990.
(Cited on pages 27 and 102.)

[55] A. S. van de Nes, J. J. M. Braat, and S. F. Pereira. High-density optical data storage. *Rep. Prog. Phys.*, 69(8):2323, 2006.
(Cited on page 29.)

[56] W. Tittel, M. Afzelius, T. Chanelière, R. L. Cone, S. Kröll, S. A. Moiseev, and M. Sellars. Photon-echo quantum memory in solid state systems. *Laser & Photonics Reviews*, 4(2):244–267, 2010.
(Cited on page 29.)

[57] K. Hammerer, A. S. Sørensen, and E. S. Polzik. Quantum interface between light and atomic ensembles. *Rev. Mod. Phys.*, 82:1041–1093, 2010.
(Cited on page 29.)

[58] P. R. Berman and V. D. Malinovsky. In *Principles of Laser Spectroscopy and Quantum Optics*, chapter 3. Princeton University Press, 1945.
(Cited on page 31.)

[59] M. O. Scully and S. Zubairy. *Quantum Optics*. Cambridge University Press, 1997.
(Cited on page 34.)

[60] F. Bloch. Nuclear induction. *Phys. Rev.*, 70:460–474, 1946.
(Cited on page 35.)

[61] R. P. Feynman, F. L. Vernon, and R. W. Hellwarth. Geometrical representation of the schrodinger equation for solving maser problems. *Journal of Applied Physics*, 28(1):49–52, 1957.
(Cited on page 35.)

[62] H. Torrey. Transient nutations in nuclear magnetic resonance. *Phys. Rev.*, 76:1059–1068, 1949.
(Cited on page 36.)

[63] E. L. Hahn. Spin echoes. *Phys. Rev.*, 80:580–594, 1950.
(Cited on page 40.)

[64] N. A. Kurnit, I. D. Abella, and S. R. Hartmann. Observation of a photon echo. *Phys. Rev. Lett.*, 13:567–568, 1964.
(Cited on page 40.)

[65] I. D. Abella, N. A. Kurnit, and S. R. Hartmann. Photon echoes. *Phys. Rev.*, 141:391–406, 1966.
(Cited on page 40.)

[66] E. Hahn. Nuclear induction due to free larmor precession. *Phys. Rev.*, 77:297–298, 1950.
(Cited on page 42.)

[67] R. Brewer and R. Shoemaker. Optical free induction decay. *Phys. Rev. A*, 6:2001–2007, 1972.
(Cited on page 42.)

[68] L. Mandel and E. Wolf. Optical coherence and quantum optics. chapter 7. Cambridge University Press, 1995.
(Cited on page 46.)

[69] J. Ruggiero, T. Chanelière, and J.-L. Le Gouët. Coherent response to optical excitation in a strongly absorbing rare-earth ion-doped crystal. *J. Opt. Soc. Am. B*, 27(1):32–37, 2010.
(Cited on pages 50 and 56.)

[70] M. Bonarota. *Optimisation de la programmation d'un cristal dopé aux ions de terres rares, opérant comme processeur analogique d'analyse spectrale RF, ou de stockage d'information quantique.* PhD thesis, Université Paris-Sud, 2012.
(Cited on pages 50, 67, and 116.)

[71] S. O. Elyutin, S. M. Zakharov, and E. A. Manykin. Theory of the photon-echo formation. *Sov. Phys. JETP*, 49:421, 1979.
(Cited on page 54.)

[72] N. W. Carlson, W. R. Babbitt, T. W. Mossberg, L. J. Rothberg, and A. G. Yodh. Storage and time reversal of light pulses using photon echoes. *Opt. Lett.*, 8(9):483–485, 1983.
(Cited on page 54.)

[73] J. Ruggiero, J-L. Le Gouët, C. Simon, and T. Chanelière. Why the two-pulse photon echo is not a good quantum memory protocol. *Phys. Rev. A*, 79:053851, 2009.
(Cited on page 54.)

[74] W. K. Wootters and W. H. Zurek. A single quantum cannot be cloned. *Nature*, 299:802–803, 1982.
(Cited on page 54.)

[75] N. Sangouard, C. Simon, J. Minář, M. Afzelius, T. Chanelière, N. Gisin, J-L. Le Gouët, H. de Riedmatten, and W. Tittel. Impossibility of faithfully storing single photons with the three-pulse photon echo. *Phys. Rev. A*, 81:062333, 2010.
(Cited on page 57.)

[76] N. Sangouard, C. Simon, M. Afzelius, and N. Gisin. Analysis of a quantum memory for photons based on controlled reversible inhomogeneous broadening. *Phys. Rev. A*, 75:032327, 2007.
(Cited on pages 58 and 63.)

[77] A. Abragam. *Principles of Nuclear Magnetism.* Oxford University Press, Oxford, United Kingdom, 1961.
(Cited on page 64.)

[78] M. M. T. Loy. Observation of population inversion by optical adiabatic rapid passage. *Phys. Rev. Lett.*, 32:814–817, 1974.
(Cited on page 64.)

[79] M. F. Pascual-Winter, R-C. Tongning, T. Chanelière, and J-L. Le Gouët. Securing coherence rephasing with a pair of adiabatic rapid passages. *New Journal of Physics*, 15(5):055024, 2013.
(Cited on page 64.)

[80] N. V. Vitanov, T. Halfmann, B.W. Shore, and K. Bergmann. Laser-induced population transfer by adiabatic passage techniques. *Annual Review of Physical Chemistry*, 52:763–809, 2001.
(Cited on page 65.)

[81] M. S. Silver R. I. Joseph and D. I. Hoult. Selective spin inversion in nuclear magnetic resonance and coherent optics through an exact solution of the Bloch-Riccati equation. *Phys. Rev. A*, 31:2753–2755, 1985.
(Cited on page 66.)

[82] I. Zafarullah, M. Tian, T. Chang, and W. R. Babbitt. Preparation of inverted medium and processing in the inverted medium. *Journal of Luminescence*, 127(1):158 – 163, 2007. Proceedings of the Ninth International Meeting on

Hole Burning, Single Molecule, and Related Spectroscopies: Science and Applications Hole Burning, Single Molecule, and Related Spectroscopies: Science and Applications.
(Cited on page 67.)

[83] L. Rippe, M. Nilsson, S. Kröll, R. Klieber, and D. Suter. Experimental demonstration of efficient and selective population transfer and qubit distillation in a rare-earth-metal-ion-doped crystal. *Phys. Rev. A*, 71:062328, 2005.
(Cited on pages 67 and 105.)

[84] H. M. Gibbs. Incoherent resonance fluorescence from a Rb atomic beam excited by a short coherent optical pulse. *Phys. Rev. A*, 8:446–455, 1973.
(Cited on page 79.)

[85] J. Dajczgewand, J.-L. Le Gouët, A. Louchet-Chauvet, and T. Chanelière. Large efficiency at telecom wavelength for optical quantum memories. *Opt. Lett.*, 39(9):2711–2714, 2014.
(Cited on pages 93 and 150.)

[86] F. R. Graf, A. Renn, G. Zumofen, and U. P. Wild. Photon-echo attenuation by dynamical processes in rare-earth-ion-doped crystals. *Phys. Rev. B*, 58:5462–5478, 1998.
(Cited on pages 100 and 102.)

[87] J. Huang, J. M. Zhang, A. Lezama, and T. W. Mossberg. Excess dephasing in photon-echo experiments arising from excitation-induced electronic level shifts. *Phys. Rev. Lett.*, 63:78–81, 1989.
(Cited on page 100.)

[88] J. Dajczgewand, R. Ahlefeldt, T. Böttger, A. Louchet-Chauvet, J-L. Le Gouët, and T. Chanelière. Optical memory bandwidth and multiplexing capacity in the erbium telecommunication window. *New Journal of Physics*, 17(2):023031, 2015.
(Cited on pages 101, 103, 111, and 151.)

[89] M. Mitsunaga, T. Takagahara, R. Yano, and N. Uesugi. Excitation-induced frequency shift probed by stimulated photon echoes. *Phys. Rev. Lett.*, 68:3216–3219, 1992.
(Cited on page 102.)

[90] C. W. Thiel, R. M. Macfarlane, Y. Sun, T. Böttger, N. Sinclair, W. Tittel, and R. L. Cone. Measuring and analyzing excitation-induced decoherence in

rare-earth-doped optical materials. *Laser Phys.*, 24:106002, 2014.
(Cited on page 105.)

[91] F. de Seze, F. Dahes, V. Crozatier, I. Lorgeré, F. Bretenaker, and J-L. Le Gouët. Coherent driving of Tm^{3+}:YAG ions using a complex hyperbolic secant optical field. *Eur. Phys. J. D*, 33(3):343–355, 2005.
(Cited on page 105.)

[92] R. M. Macfarlane. Optical stark spectroscopy of solids. *Journal of Luminescence*, 125:156–174, 2007.
(Cited on page 106.)

[93] S. R. Hastings-Simon, M. U. Staudt, M. Afzelius, P. Baldi, D. Jaccard, W. Tittel, and N. Gisin. Controlled stark shifts in Er^{3+} -doped crystalline and amorphous waveguides for quantum state storage. *Optics Communications*, 266(2):716–719, 2006.
(Cited on page 106.)

[94] M. P. Hedges. *High performance solid state quantum memory.* PhD thesis, The Australian National University, 2011.
(Cited on page 106.)

[95] V. Crozatier, G. Gorju, F. Bretenaker, J.-L. Le Gouët, I. Lorgeré, O. Guillot-Noël, and Ph. Goldner. Experimental observation of spectral diffusion in an optically pumped crystal. *Journal of Luminescence*, 127(1):65 – 70, 2007.
(Cited on page 107.)

[96] S. B. Altner, G. Zumofen, U. P. Wild, and M. Mitsunaga. Photon-echo attenuation in rare-earth-ion-doped crystals. *Phys. Rev. B*, 54:17493–17507, 1996.
(Cited on page 107.)

[97] Y. S. Bai and R. Kachru. Nonequilibrium resonant-phonon-induced excess photon-echo dephasing. *Phys. Rev. B*, 46:13735–13738, 1992.
(Cited on page 107.)

[98] K. P. Kretsch, C. Belton, S. Lipson, W. J. Blau, F. Z. Henari, H. Rost, S. Pfeiffer, A. Teuschel, H. Tillmann, and H.-H. Hörhold. Amplified spontaneous emission and optical gain spectra from stilbenoid and phenylene vinylene derivative model compounds. *Journal of Applied Physics*, 86(11):6155–6159, 1999.
(Cited on page 116.)

[99] L. W. Casperson and A. Yariv. Spectral narrowing in high-gain lasers. *IEEE Journal of Quantum Electronics*, 8(2):80–85, 1972.
(Cited on page 117.)

[100] A. Costela, O. García, L. Cerdán, I. García-Moreno, and R. Sastre. Amplified spontaneous emission and optical gain measurements from pyrromethene 567 - doped polymer waveguides and quasi-waveguides. *Opt. Express*, 16(10):7023–7036, 2008.
(Cited on page 117.)

[101] M. D. McGehee, R. Gupta, S. Veenstra, E. K. Miller, M. A. Díaz-García, and A. J. Heeger. Amplified spontaneous emission from photopumped films of a conjugated polymer. *Phys. Rev. B*, 58:7035–7039, 1998.
(Cited on page 117.)

[102] F. Auzel, G. Baldacchini, L. Laversenne, and G. Boulon. Radiation trapping and self-quenching analysis in Yb^{3+}, Er^{3+}, and Ho^{3+} doped Y_2O_3. *Optical Materials*, 24:103 – 109, 2003. Proceedings of the Fifth French-Israeli Workshop on Optical Properties of Inorganic Materials.
(Cited on page 118.)

[103] R. Brede, E. Heumann, J. Koetke, T. Danger, G. Huber, and B. Chai. Green up-conversion laser emission in Er-doped crystals at room temperature. *Appl. Phys. Lett.*, 63:2030, 1993.
(Cited on page 121.)

[104] E. Sani, A. Toncelli, M. Tonelli, and F. Traverso. Growth and spectroscopic analysis of Tm, Ho:KYF_4. *J. Phys.: Condens. Matter*, 16:241, 2004.
(Cited on page 121.)

[105] C. W. Thiel, W. R. Babbitt, and R. L. Cone. Optical decoherence studies of yttrium oxyorthosilicate Y_2SiO_5 codoped with Er^{3+} and Eu^{3+} for optical signal processing and quantum information applications at 1.5 microns. *Phys. Rev. B*, 85:174302, 2012.
(Cited on page 124.)

[106] K. W. Jang and R. S. Meltzer. Homogeneous and inhomogeneous linewidths of Eu^{3+} in disordered crystalline systems. *Phys. Rev. B*, 52:6431–6439, 1995.
(Cited on page 126.)

[107] A. Amisse. Efficient quantum memory in the telecommunication wavelength range. *Rapport de stage en Laboratoire. Master 2 de Physique Fondamentale.*

Spécialité Laser, Optique, Matière, Université Paris-sud U.F.R Sciences, 2015. (Cited on page 129.)

Optical memory in an erbium doped crystal: efficiency, bandwidth and noise studies for quantum memory applications

Quantum information processing has been developing rapidly in the last two decades as a way to overcome the limitations of classical electronics. Several components to generate, process and send quantum information are needed. In this context, optical quantum memories appear as principal components to communicate quantum information at long distances by overcoming the losses of the optical fibers in the so-called quantum repeater scheme. During the last decade several storage protocols to store quantum information have been proposed and tested. In this thesis, I present the Revival of Silenced Echo (ROSE) protocol implemented in an Er^{3+}:Y_2SiO_5 crystal. This material is a good candidate for a quantum memory because of its transition in the C-band of the telecom wavelengths where the losses in optical fibers are minimized. In this work, I evaluate the ROSE performances with weak classical pulses. I measure efficiency, bandwidth and storage time which are the typical figures of merit for an optical quantum memory. Starting with a fixed bandwidth, I demonstrate experimentally a good efficiency. Additionally, I measure the bandwidth dependence of the protocol. For this latter, the dipole-dipole interactions between erbium ions appears as limiting factors. Finally, I implement the ROSE protocol with a few photons per pulse to show its potential as a quantum memory. I report good efficiencies with a moderate signal to noise ratio. I finish this work with a series of measurements in new materials (doped or codoped with erbium), to extend the processing bandwidth of Er doped samples compatible the telecom wavelength range.

Keywords

Quantum memory	Quantum repeater	Quantum communication
Telecom wavelength	Erbium	Optical processing

Mémoire optique dans un cristal dopé erbium: efficacité, bande passante and analyse des bruits pour des applications des mémoires quantiques.

Le traitement quantique de l'information comme moyen de surmonter les limites de l'électronique classique a connu un développement rapide dans les deux dernières décennies. Plusieurs composants pour générer, traiter et envoyer l'information quantique sont nécessaires. Dans ce contexte, les mémoires quantiques optiques apparaissent comme des composantes principales capables de communiquer l'information quantique sur de longues distances en surmontant les pertes des fibres optiques dans un schéma de répéteur quantique. Durant la dernière décennie, plusieurs protocoles de stockage pour stocker l'information quantique ont été proposés et testés. Dans cette thèse, je présente le protocole Revival of Silenced Echo (ROSE) et sa réalisation dans un cristal Er^{3+}:Y_2SiO_5. Ce matériau est un bon candidat pour une mémoire quantique grâce à sa transition dans la bande C des télécommunications où les pertes dans les fibres optiques sont minimales. Dans ce travail, j'évalue les performances du ROSE avec des impulsions faibles classiques. Je mesure l'efficacité, la bande passante et le temps de stockage qui sont des figures de mérite typiques d'une mémoire quantique optique. Pour une bande passante fixe, je démontre expérimentalement une bonne efficacité. En outre, je mesure la dépendance de la bande passante du protocole. Pour cette dernière les interactions dipôle-dipôle entre les ions d'erbium apparaît comme un facteur limitant. Enfin, je réalise le protocole ROSE avec quelques photons par impulsion afin d'évaluer son potentiel comme mémoire quantique. Je démontre une bonne efficacité avec un rapport signal sur bruit modéré. Je termine ce travail par une série de mesures dans des matériaux nouveaux (co-dopé ou dopé avec de l'erbium), pour augmenter la bande-passante de traitement d'échantillons dopés Er compatible avec les longueurs d'onde des télécommunications.

Mots clés

Mémoire quantique	Répéteur quantique	Communication quantique
Longuer onde télécommunication	Erbium	Traitement optique

Synthèse en français

Le traitement quantique de l'information comme moyen de surmonter les limites de l'électronique classique a connu un développement rapide dans les deux dernières décennies. Plusieurs composants pour générer, traiter et envoyer l'information quantique sont nécessaires. Dans ce contexte, les mémoires quantiques optiques sont les composants principaux pour communiquer l'information quantique sur de longues distances en surmontant les pertes des fibres optiques dans un schéma de répéteur quantique. Durant la dernière décennie, plusieurs protocoles de stockage pour stocker l'information quantique ont été proposés et testés. Dans cette thèse, je présente le protocole Revival of Silenced Echo (ROSE) et sa rèalisation dans un cristal Er^{3+}:Y_2SiO_5. Ce matériau est un bon candidat pour une mémoire quantique grâce à sa transition dans la bande C des télécommunications où les pertes dans les fibres optiques sont minimales. Dans ce travail, j'évalue les performances du ROSE avec des impulsions faibles classiques. J'ai étudié l'efficacité du ROSE en fonction de l'absorption du milieu (figure 1).
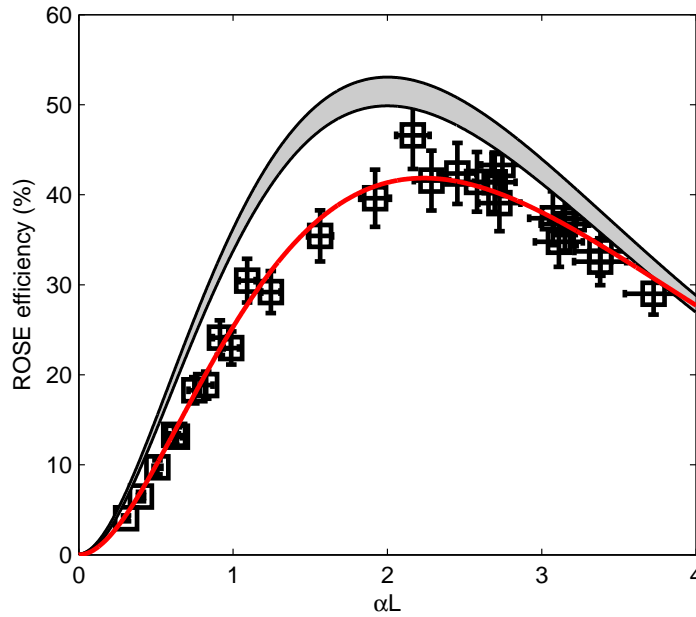

Figure 1. Efficacité du ROSE en fonction de l'épaisseur optique αL. Les carrés noirs représentent les mesures, en gris un modèle théorique incluant la décohérence et en rouge un ajustement incluant à la fois la décohérence et modélisant les imperfections pendant la séquence de rephasage constitutive du protocole [85].

L'accord entre les mesures et l'ajustement rouge est bon. Pour une bande passante fixe de 800 kHz, je démontre expérimentalement une bonne efficacité. Un maximum autour de 40% a été mesuré pour un temps de stockage de 16 mμs, à com-

parer èl'efficacité maximum de 54% que nous pouvons atteindre avec la configuration de faisceaux utilisée dans cette expérience.

En outre, je mesure la dépendance de l'efficacité en augmentant la bande passante du protocole pour une configuration spécifique d'axes par rapport au champ magnétique externe (figure 2) [88]. Cette dernière permet d'optimiser le décohérence pour cette échantillon qui reste très anisotrope.
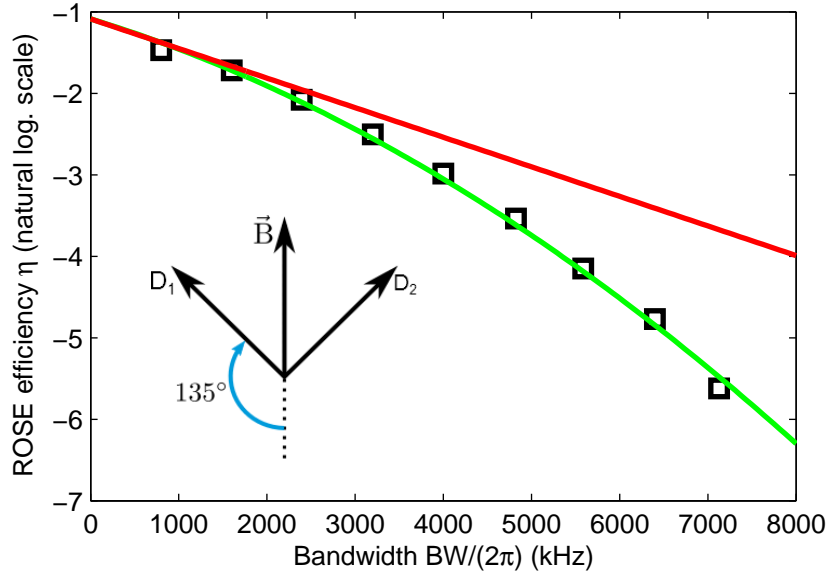

Figure 2. Logarithme naturel de l'efficacité du ROSE en fonction de la bande passante excitée. Les carrés noirs représentent les mesures, la courbe verte un ajustement quadratique qui dévie de la droite en rouge. Cette dernière inclut simplement la décohérence.

La courbe rouge montre la décroissance de l'efficacité prévue en incluant la décohérence. La courbe verte est obtenue en incluant les interactions dipôle-dipôle entre les ions d'erbium qui se traduisent effectivement par une réduction du temps de cohérence avec la bande passante excitée. Cet effet, appelé diffusion spectrale instantanée, vient de l'interaction entre les dipôles permanents électriques ou magnétiques des ions d'erbium.

Enfin, je réalise le protocole ROSE avec quelques photons par impulsion afin d'évaluer son potentiel comme mémoire quantique (figure 3) [25]. Je mesure une efficacité de 30% avec un temps de stockage de 16 ms. Je démontre une bonne efficacité pour un rapport signal sur bruit modéré, d'environ 0,7. Je termine ce travail par une série de mesures dans des matériaux nouveaux (co-dopé ou dopé avec de l'erbium), pour augmenter la bande-passante de traitement compatible avec les longueurs d'onde des télécommunications. Le matériau le plus prometteur est $Er^{3+}:Y_2SiO_5$ (dopé avec 30 ppm d'erbium) co-dopé avec 10000 ppm de scandium ($Er^{3+}+Sc^{3+}:Y_2SiO_5$) (figure 4).
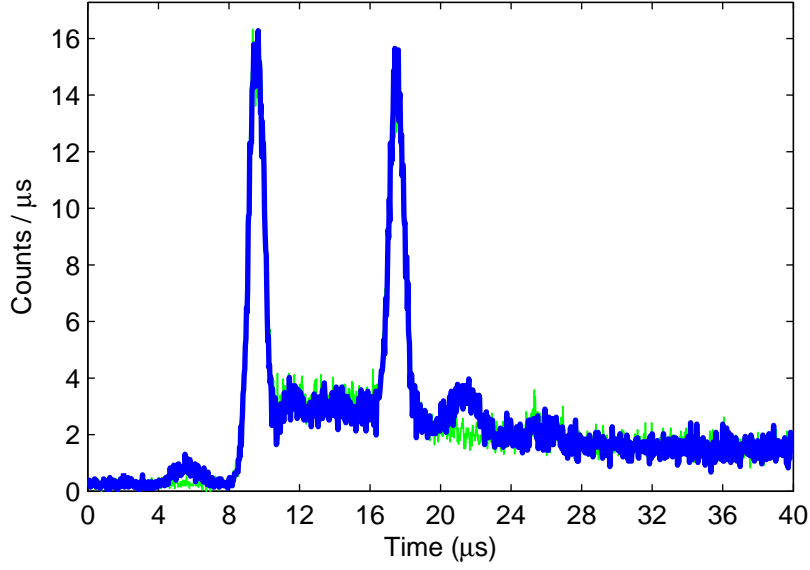
Figure 3. ROSE avec quelques photons par impulsion en coups par microsecondes sur un détecteur de photons uniques. En bleu, ROSE avec 7.8 photons par impulsion en entrée et, en vert, ROSE sans impulsion d'entrée (bruit).
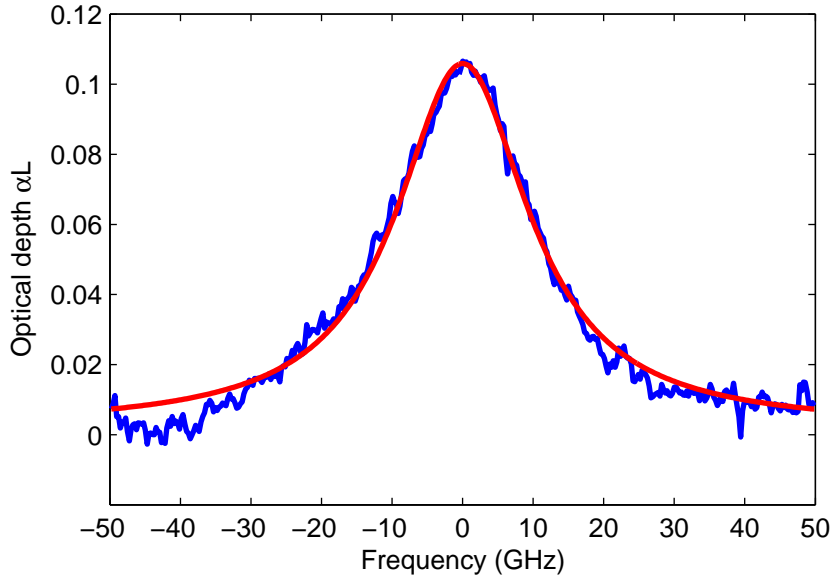

Figure 4. Profil d'absorption de l'erbium dans $Er^{3+}+Sc^{3+}:Y_2SiO_5$.

L'élargissement inhomogène pour cet échantillon est d'environ 20 GHz à comparer à 350 MHz pour $Er^{3+}:Y_2SiO_5$. Le temps de cohérence est très comparable au cristal seulement dopé avec erbium. Cela donne un produit temps-bande passante 50 fois plus large pour le cristal co-dopé scandium ouvrant des perspectives pour le traitement classique ou quantique large-bande.